



*Institut für Geowissenschaften  
Mathematisch-Naturwissenschaftliche Fakultät  
Universität Potsdam*



# Pliocene-Pleistocene landscape evolution in south-central Chile

Interactions between tectonic, geomorphic, and climatic  
processes

**Katrin Rehak**

**Dissertation  
zur Erlangung des akademischen Grades  
Doktor der Naturwissenschaften (Dr. rer. nat.)  
in der Wissenschaftsdisziplin Geologie**

**eingereicht an der Mathematisch-Naturwissenschaftlichen Fakultät  
der Universität Potsdam**

**Potsdam, im April 2008**

Elektronisch veröffentlicht auf dem  
Publikationsserver der Universität Potsdam:  
<http://opus.kobv.de/ubp/volltexte/2008/1979/>  
[urn:nbn:de:kobv:517-opus-19793](http://nbn-resolving.org/urn:nbn:de:kobv:517-opus-19793)  
[<http://nbn-resolving.de/urn:nbn:de:kobv:517-opus-19793>]

*für Richard und Theresia Anders*

## Abstract

Landscapes evolve in a complex interplay between climate and tectonics. Thus, the geomorphic characteristics of a landscape can only be understood if both, climatic and tectonic signals of past and ongoing processes can be identified. In order to evaluate the impact of both forcing factors it is crucial to quantify the evolution of geomorphic markers in natural environments.

The Cenozoic Andes are an ideal natural setting to evaluate tectonic and climatic aspects of landscape evolution at different time and length scales and in different natural compartments. The Andean Cordillera constitutes the type subduction orogen and is associated with the subduction of the oceanic Nazca Plate beneath the South American continent since at least 200 million years. In Chile and the adjacent regions this convergent margin is characterized by active tectonics, volcanism, mountain building, and the impact of geomorphic processes governed by various superposed climate zones. Importantly, along the coast of Chile megathrust earthquakes occur frequently and influence landscape evolution. In fact, the largest earthquake ever recorded occurred in south-central Chile in 1960 and comprised a rupture zone of ~ 1000 km length, a rupture zone that also appears to have been the locus of preceding large earthquakes. However, on longer time scales beyond historic documentation of seismicity it is not well known, how such seismotectonic segments have behaved and how they influence the geomorphic evolution of the coastal realms. With several semi-independent morphotectonic segments, recurrent megathrust earthquakes, and a plethora of geomorphic features indicating sustained tectonism, the subduction margin of Chile is thus a key area to study relationships between surface processes and tectonics.

In this study, I combined geomorphology, geochronology, sedimentology, as well as morphometry in order to quantify the Pliocene-Pleistocene landscape evolution of the tectonically active south-central Chile forearc. With this analysis, I provide (1) new results about the influence of seismotectonic forearc segmentation on the geomorphic evolution and (2) new insights in the interaction between climate and tectonics with respect to the morphology of the Chilean forearc region.

In particular, I show that the forearc of south-central Chile is characterized by three long-term segments that are not correlated with short-lived earthquake-rupture zones that may, however, influence forearc morphology over the duration of several earthquake cycles. In the study area these segments are the Nahuelbuta, Toltén, and Bueno segments, each recording a distinct geomorphic and tectonic evolution. The Nahuelbuta and Bueno segments are undergoing active tectonic uplift. The long-term behavior of these two segments is manifested in form of two doubly plunging, growing antiforms that constitute an integral part of the Coastal Cordillera and record the uplift of marine and river terraces. In addition, these uplifting areas have caused major changes in flow directions of rivers. In contrast, the Toltén segment, situated between the two other segments, appears to be quasi-stable.

In order to further quantify uplift and incision in the actively deforming Nahuelbuta segment, I dated an erosion surface and fluvial terraces in the Coastal Cordillera with cosmogenic  $^{10}\text{Be}$  and  $^{26}\text{Al}$  and optically stimulated luminescence, respectively. According to my results, late Pleistocene uplift rates corresponding to  $0.88 \text{ mm a}^{-1}$  are faster than surface-uplift rates averaging over the last 5 Ma, which are in the range of  $0.21 \text{ mm a}^{-1}$ . This discrepancy suggests an acceleration of the tectonic processes during the late Quaternary. Nevertheless, surface uplift is highly variable in time and

space and might preferably concentrate along reverse faults as indicated by a late Pleistocene flow reversal which I dated to have taken place ~ 80 ka ago. I infer that this event is related to uplift above a blind reverse fault.

In addition, the results of exposure dating with cosmogenic  $^{10}\text{Be}$  and  $^{26}\text{Al}$  indicate that the morphotectonic segmentation of this region of the forearc has been established in Pliocene time, coeval with the initiation of uplift of the Coastal Cordillera about 5 Ma ago, inferred to be related to a shift in subduction mode from erosion to accretion. This substantial modification of the subduction process has been attributed to the onset of global cooling in the late Miocene and an associated increase in sediment supply into the trench.

Finally, I dated volcanic clasts obtained from alluvial surfaces in the Central Depression, a low-relief sector separating the Coastal from the Main Cordillera, with stable cosmogenic  $^3\text{He}$  and  $^{21}\text{Ne}$ , in order to reveal the controls of sediment accumulation in the forearc. My results document that these gently sloping surfaces have been deposited 150 to 300 ka ago. Although not very well constrained in this phase, this deposition may be related to changes in the erosional regime in the transition between glacial and interglacial episodes.

Taken together, the data indicates that the overall geomorphic expression of the forearc is of post-Miocene age and may be intimately related to a climatic overprint of the tectonic system. This climatic forcing is also reflected in the topography and local relief of the Central and Southern Andes. Both parameters vary considerably along the margin, determined by the dominant surface process that in turn is eventually controlled by climate. However, relief also partly mirrors surface processes that have taken place under past climatic conditions, emphasizing the major importance of changing paleo-climates and the transient character of the landscape in Chile.

## Zusammenfassung

Landschaften entwickeln sich in einem komplexen Zusammenspiel von Klima und Tektonik. Demzufolge kann die Geomorphologie von Landschaften nur verstanden werden, wenn sowohl klimatische als auch tektonische Signale vergangener und rezenter Prozesse identifiziert werden können. Um den Einfluss beider Faktoren zu bewerten, ist es deshalb äußerst wichtig, die Evolution geomorphologischer Marker in natürlichen Umgebungen quantitativ zu analysieren.

Die känozoischen Anden sind eine ideale Region, um tektonische und klimatische Aspekte der Landschaftsentwicklung auf verschiedenen Zeit- und Längenskalen zu erforschen. Das andine Gebirge ist das Modell-Subduktionsorogen und assoziiert mit der Subduktion der ozeanischen Nazca-Platte unter den südamerikanischen Kontinent seit ca. 200 Millionen Jahren. In Chile und angrenzenden Regionen ist dieser konvergente Plattenrand geprägt von aktiver Tektonik, Vulkanismus und Gebirgsbildung sowie geomorphologischen Prozessen, die von verschiedenen Klimazonen determiniert werden. Bedeutenderweise ereignen sich entlang der Küste Chiles häufig Megaerdbeben, die die Landschaftsentwicklung stark beeinflussen. Tatsächlich ereignete sich das größte jemals aufgezeichnete Erdbeben 1960 im südlichen Zentralchile. Es umfasste eine Bruchzone von ca. 1.000 km Länge, die anscheinend ebenfalls der Ausgangspunkt vieler vorhergehender Erdbeben gewesen ist. Nichtsdestotrotz ist auf längeren Zeitskalen, die über historische Dokumentationen von seismischen Ereignissen hinausgehen, nicht bekannt, wie sich solche seismotektonischen Segmente verhalten und wie sie die geomorphologische Entwicklung der Küstengebiete beeinflussen. Mit einigen semi-unabhängigen morphotektonischen Segmenten, wiederkehrenden Megaerdbeben und einer Fülle geomorphologischer Marker, die aktive Tektonik anzeigen, ist somit der Subduktions-Plattenrand von Chile ein Schlüsselgebiet für das Studium von Zusammenhängen zwischen Oberflächenprozessen und Tektonik.

In dieser Arbeit kombiniere ich Geomorphologie, Geochronologie, Sedimentologie und Morphometrie, um die plio-pleistozäne Landschaftsentwicklung des tektonisch aktiven süd-zentralchilenischen Forearcs zu quantifizieren. Mit dieser Analyse liefere ich (1) neue Ergebnisse über den Einfluss seismotektonischer Forearc-Segmentierung auf die geomorphologische Entwicklung und (2) neue Erkenntnisse über die Interaktion zwischen Klima und Tektonik bezüglich der Gestaltung des chilenischen Forearcs.

Ich zeige, dass der Forearc von Südzentral-Chile durch drei langlebige morphotektonische Segmente charakterisiert ist, die nicht mit kurzlebigen Erdbebenbruchzonen korrelieren, die jedoch die Forearc-Morphologie über die Dauer mehrerer Erdbebenzyklen hinweg beeinflussen können. Die Segmente in meinem Arbeitsgebiet heißen Nahuelbuta, Toltén und Bueno Segment, wovon jedes eine deutlich verschiedene geomorphologische und tektonische Entwicklung durchläuft. Die Nahuelbuta und Bueno Segmente unterliegen aktiver tektonischer Hebung. Das langfristige Verhalten dieser beiden Segmente manifestiert sich in zwei beidseitig abtauchenden, wachsenden Antiklinalen, die integraler Bestandteil des Küstengebirges sind und die Hebung von marinen und fluvialen Terrassen aufzeichnen. Zusätzlich verursachte die Hebung dieser Gebiete weitreichende Veränderungen in den Fließrichtungen des Gewässernetzes. Im Gegensatz dazu ist das Toltén Segment, das sich zwischen den beiden anderen Segmenten befindet, quasi-stabil.

Um desweiteren die Hebung und Einschneidung in dem tektonisch aktiven Nahuelbuta Segment zu quantifizieren, habe ich eine Erosionsfläche und fluviale Terrassen in dem Küstengebirge mit kosmogenem  $^{10}\text{Be}$  und  $^{26}\text{Al}$  bzw. optisch stimulierter Lumineszenz datiert. Meinen Ergebnissen zufolge sind die spätpleistozänen Hebungsdaten, die ca.  $0,88 \text{ mm a}^{-1}$  betragen, höher als die Oberflächenhebungsdaten, die über die letzten 5 Millionen Jahre mitteln und ca.  $0,21 \text{ mm a}^{-1}$  betragen. Diese Diskrepanz deutet eine Beschleunigung der tektonischen Prozesse im Spätquartär an. Die Hebung der Oberfläche variiert räumlich und zeitlich allerdings sehr stark und könnte sich präferiert an Aufschiebungen konzentrieren. Darauf deutet eine spätpleistozäne Flussumkehr, die vor 80 ka stattfand, hin. Sie steht meinen Daten zufolge in Beziehung zu Hebung über einer blinden Aufschiebung.

Zusätzlich zeigen die Ergebnisse der Expositionsdatierung mit kosmogenem  $^{10}\text{Be}$  und  $^{26}\text{Al}$ , dass die morphotektonische Segmentierung im Pliozän etabliert wurde, zeitgleich mit dem Beginn der Hebung des Küstengebirges vor ca. 5 Millionen Jahren infolge eines Wechsels des Subduktionsmodus von Erosion zu Akkretion. Diese substantielle Modifikation des Subduktionsprozesses wurde auf den Beginn der globalen Abkühlung im späten Miozän und einer damit assoziierten erhöhten Sedimentzufuhr in den Trench zurückgeführt.

Schließlich habe ich vulkanische Klaster, die aus alluvialen Flächen im Längstal - einem Niedrigreliefsektor, der das Küsten- vom Hauptgebirge trennt - stammen, mit den stabilen kosmogenen Nukliden  $^3\text{He}$  und  $^{21}\text{Ne}$  datiert, um Aufschluss über die Faktoren zu erhalten, die die Sedimentablagerung im Forearc bestimmen. Gleichwohl zu diesem Zeitpunkt noch nicht vollkommen sicher, weisen meine Ergebnisse darauf hin, dass diese flach einfallenden Oberflächen, die vor 150.000 bis 300.000 Jahren abgelagert wurden, anscheinend in Zusammenhang mit Änderungen des Erosionsregimes im Übergang zwischen glazialen und interglazialen Episoden entstanden sind.

Zusammenfassend zeigen die Daten, dass der heutige geomorphologische Ausdruck des Forearcs post-Miozän und eng mit einer klimatischen Überprägung des tektonischen Systems verknüpft ist. Der klimatische Einfluss spiegelt sich ebenfalls in der Topographie und dem lokalen Relief der Zentral- und Südanlagen wider. Beide Parameter variieren stark entlang des Plattenrandes, bestimmt durch den jeweils dominierenden Oberflächenprozess, der wiederum letztendlich vom vorherrschenden Klima abhängt. Allerdings reflektiert das Relief teilweise noch Oberflächenprozesse, die unter vergangenen klimatischen Gegebenheiten aktiv waren. Das betont die große Bedeutung von Paläoklimaten und Reliktformen im Landschaftscharakter von Chile.

# Contents

<b>Abstract</b> .....	ii
<b>Zusammenfassung</b> .....	iv
<b>Contents</b> .....	vi
<b>List of figures</b> .....	viii
<b>List of tables</b> .....	ix
<b>Acknowledgements</b> .....	x
<b>1. Introduction</b> .....	1
<b>2. Regional setting</b> .....	4
2.1 Geodynamic framework .....	4
2.2 Climatic conditions .....	7
<b>3. Morphotectonic segmentation of an active forearc, 37° - 41°S, Chile</b>	
3.1 Introduction .....	9
3.2 Regional tectonic setting .....	10
3.3 Methods .....	12
3.4 Results .....	13
3.4.1 Drainage-network analysis and sedimentological observations .....	13
3.4.2 Geological and geophysical data .....	18
3.5 Discussion .....	22
3.6 Conclusions .....	25
<b>4. Reconstructing surface uplift using cosmogenic nuclides, the Coastal Cordillera in south-central Chile</b> .....	26
4.1 Introduction .....	26
4.2 Regional setting .....	28
4.3 Methodology .....	29
4.4 Results .....	31
4.5 Discussion .....	35
4.6 Conclusions .....	37
<b>5. Late Pleistocene landscape evolution in south-central Chile constrained by luminescence and stable cosmogenic nuclide dating</b>	
5.1 Introduction .....	38
5.2 Regional setting .....	38

5.3 Methodology .....	42
5.3.1 Cosmogenic nuclide dating .....	43
5.3.2 Luminescence dating .....	43
5.4 Results .....	44
5.4.1 Cosmogenic nuclide dating .....	44
5.4.2 Luminescence dating .....	48
5.5 Discussion .....	51
5.6 Conclusions .....	55
<b>6. Climatic controls on drainage-basin morphology - the western Andean flank between 15.5° and 41.5°S</b> .....	<b>57</b>
6.1 Introduction .....	58
6.2 Regional setting .....	59
6.2.1 Geologic setting .....	59
6.2.2 Climatic setting .....	60
6.3 Methodology .....	62
6.4 Results .....	64
6.5 Discussion .....	68
6.6 Conclusions .....	72
<b>7. Conclusions</b> .....	<b>73</b>
<b>8. Bibliography</b> .....	<b>75</b>
<b>Appendix</b> .....	<b>95</b>
Climatic controls on drainage-basin morphology .....	95

## List of figures

Figure 2.1:	Topography, geodynamics, and climate along the Central to Southern Andes .....	5
Figure 2.2:	Morphotectonic units and main structures of south-central Chile .....	6
Figure 3.1:	Topography, bathymetry, and geology of south-central Chile ...	11
Figure 3.2:	Segmentation and drainage evolution of the Coastal Cordillera	14
Figure 3.3:	Local relief, steepness, and swath profiles of the Coastal Cordillera .....	15
Figure 3.4:	River longitudinal profiles and PCI-indices in the Nahuelbuta segment .....	16
Figure 3.5:	DS-plots of rivers crossing the Coastal Cordillera .....	17
Figure 3.6:	Pebble-count and flow-direction measurements of alluvial terraces along the Pellahuén river .....	18
Figure 3.7:	Bathymetric map and earthquake distribution in south-central Chile .....	19
Figure 3.8:	Historic earthquake-rupture zones, coseismic slip and deformation during the 1960-earthquake, gravimetry, and morphotectonic segments .....	21
Figure 3.9:	Evolution model of the south-central Chilean forearc .....	23
Figure 4.1:	Regional setting of the south-central Chile forearc .....	29
Figure 4.2:	Slope and topography of the erosion surface on top of the Coastal Cordillera .....	30
Figure 4.3:	Erosion surface at an elevation of 750 m .....	31
Figure 4.4:	Two alternative evolutionary sequences of surface development in the Coastal Cordillera .....	33
Figure 4.5:	Depth, ascent time, and uplift rates calculated from cosmogenic nuclide measurements .....	34
Figure 4.6:	Nuclide-ratio plots .....	35
Figure 5.1:	Study area in the forearc of south-central Chile .....	40
Figure 5.2:	Schematic stratigraphy of the Central Depression around 38° to 39°S .....	41
Figure 5.3:	Three-isotope plot for Ne-ratios .....	47
Figure 5.4:	Age distribution of the analyzed samples .....	48
Figure 5.5:	OSL depletion curve .....	49
Figure 5.6:	Dose-distribution plot .....	50
Figure 5.7:	Distribution of multicolored conglomerates, surface ages, and terrace ages .....	51
Figure 5.8:	Evolution model of the Pellahuén valley .....	52
Figure 5.9:	Thalweg profile along the Pellahuén valley .....	52
Figure 5.10:	Correlation of sediment accumulation and sea level .....	55

Figure 6.1:	Rainfall, local relief, shortening and uplift rates along the Central to Southern Andes .....	61
Figure 6.2:	Analyzed drainage basins and calculated morphometric indices .....	63
Figure 6.3:	Correlations between relief and climate variables .....	65
Figure 6.4:	Landsat TM images and local relief showing two typical headwater basins of each climatic zone .....	67
Figure 6.5:	North-south distribution of relief and climate parameters .....	68
Figure 6.6:	Relative drainage density along the Central to Southern Andes and implications for fluvial erosion .....	70

### List of tables

Table 3.1:	Basic morphometric data of the analyzed drainage basins and their trunk streams .....	16
Table 4.1:	Summary of AMS-measurements, nuclide concentrations, nuclide ratios, production rates, scaling, and errors .....	32
Table 5.1:	Sampling details, production-rate scaling, and nuclide ages ....	45
Table 5.2:	Mass-spectrometry results, blanks, and ICP-results .....	46
Table 5.3:	Incision and uplift rates in the Pellahuén valley .....	53
Table 5.4:	Temporal storage in the Central Depression .....	54
Table 6.1:	Definition of the investigated variables extracted for each catchment .....	64
Table 6.2:	Relief reduction due to a doubling of rainfall .....	69
Table A 1:	Definition and sources of the calculated variables .....	95
Table A 2:	Raw data with geometry, relief, and climatic variables calculated for each basin: forearc and mountain-front catchments .....	96
Table A 3:	Raw data with geometry, relief, and climatic variables calculated for each basin: arc catchments .....	97
Table A 4:	Raw data with geometry, relief, and climatic variables calculated for each basin: subcatchments .....	98
Table A 5:	Correlations between variables: forearc catchments and mountain-front catchments .....	99
Table A 6:	Correlations between variables: arc catchments and subcatchments .....	100
Table A 7:	Correlations between HI, PCI, and calculated variables .....	101

## Acknowledgements

This thesis benefited from the support of many people, and I ask everyone's pardon who I did not mention here.

First, I particularly thank Manfred Strecker for giving me the possibility to actualize this project, for his scientific guidance and advises, and for the freedom to follow my own research perspectives. Additionally, I sincerely thank Helmut Echtler for continuous motivation, competence, and optimism in numerous hours of discussion as well as invaluable support in the field.

I thank all my colleagues from the University of Potsdam who accompanied my thesis in all stages. My special thanks go to Rasmus Thiede, who turned into a friend and shared the room with me during the first month of my thesis. Special thanks also go to Mónica Vásquez, Gabriela Marcano, Jessica Zamagni (the pasta was just great!), Franziska Wilke, Astrid Riemann, and Annett Junginger for the nice company in the girls' room, candy, motivation, and ideas. Additionally, I thank Andreas Bergner for Schnappi, Gerold Zeilinger for help with tricky GIS-questions and continuous supply with Swiss chocolate, Ed Sobel for always knowing where the hand magnet is, and Markus Safaricz for providing an excellent espresso whenever it was needed.

I acknowledge Daniel Melnick and Bodo Bookhagen for maps, data, and pleasant days in the field. I greatly thank Bodo Bookhagen for hours of discussions and extremely helpful, always constructive criticism. I thank George Hilley for support and discussions. I also acknowledge discussions with Susanne Blumberg, Tim Vietor, and Sebastian Lindhorst.

Furthermore, I thank my collaboration partners in many parts of the world: Maria Mardones from Concepción, Chile, for an interesting time in the field and helpful discussions, Michael Summerfield, Tibor Dunai, Steve Binnie, and Chris Fogwill from Edinburgh, Scotland, for revealing me the secrets of sample processing in the lab for cosmogenic-nuclide analysis and inspiring discussions expanding geology into the philosophic realm, the CRONUS-EU team for the extremely interesting and effective workshops, Frank Preusser from Bern, Switzerland, for training me in the OSL lab (how does Bern look in daylight?), answering all my numerous questions, his optimism, and for responding unbelievably fast to emails, and last but not least I wish to thank Samuel Niedermann and Enzo Schnabel from the GFZ Potsdam, Germany, for hours and hours at the mass spectrometer, most friendly support, and continuous availability for questions.

Funding was provided by the German Science Foundation through the Leibniz Award to Manfred Strecker (STR373-18-1), the virtual institute CSAG of the Helmholtz Foundation, and the German Academic Exchange Program (DAAD).

This thesis would not have been possible without the unconditional love and support by my parents, Heidi and Josef, as well as my brother Rainer, the best friend one can have. Last, my very special thanks go to a Polish traveller and a small mountain brook from Angola who changed my life.

## 1. Introduction

Subduction margins constitute the tectonically and seismically most active regions in the world (Ruff and Kanamori, 1980, 1989; Ishibashi, 1992; McCaffrey, 1994; Cattin et al., 1997). Landscape evolution along these margins is consequently controlled by a complex interplay between pronounced tectonics, climate, and superposed surface processes. However, deciphering the rates of landscape-forming processes and distinguishing between tectonically and climatically controlled factors has been often hampered by the difficulty to unambiguously quantify surface processes. Despite these problems the emergence of new analytical methods, such as cosmogenic-nuclide dating of geomorphic markers and processes has made the investigation, quantification, and thus the understanding of surface processes on intermediate timescales possible. This can be done now at a level of detail that had not been accessible before. In this context, climate-related processes have become once again the focus of geomorphic investigations. This is particularly the case since it has been shown that climate through the effects of surface processes may also affect tectonic rates and styles (e.g. Molnar and England, 1990; Beaumont et al., 1992; Willett, 1999; Montgomery et al., 2001; Lamb and Davis, 2003). Accordingly, climate change has not only a direct impact on vegetation and geomorphic processes, but also implications for the locus and level of activity of tectonic systems. With a long-term perspective, modifications of the tectonic system might thereby ultimately alter deformation patterns and thus influence e.g., the distribution and recurrence of tectonic movements and tectonically triggered, voluminous landslides or the evolution of drainage networks. Key questions that arise in this context are for example: (1) How do tectonic and geomorphic patterns evolve through time? and (2) Which tectonic and geomorphic processes can be induced by climate or climate-change? In turn, the solution of these issues requires knowledge about how climatic signals are actually reflected in the landscape and the depositional record. In order to answer these questions, it is thus crucial to study those landscapes that evolve in the context of both, tectonic and climatic influences.

With more than 7000 km length the Andean margin along the west coast of South America constitutes the longest subduction orogen on Earth. With ongoing mountain building, megathrust earthquakes at the margin, as well as exceptionally steep climatic gradients ranging from a hyperarid desert in the north to humid, subarctic conditions in the south (e.g. Weischet, 1970; Schwerdtfeger, 1976; Khazaradze and Klotz, 2003; Lomnitz, 2004; Charrier et al., 2007), this region is an outstanding natural laboratory to investigate landscape evolution in response to climatic and tectonic forcing.

From west to east the margin in south-central Chile comprises the Peru-Chile trench, the forearc with offshore basins and the onshore coastal ranges; a low-relief sector, the Central Depression, the main volcanic arc with up to three north-south trending ranges; and the backarc region with the adjacent foreland. Although the entire margin and orogen are coupled to the subduction process itself, the forearc constitutes the most sensitive environment that responds to any changes in the factors determining mountain building. This region records tectonic and climate-driven geomorphic processes particularly well (e.g. Gardner et al., 2001; Pazzaglia and Brandon, 2001; Hampel et al., 2004; Glodny et al., 2005; Melnick and Echtler, 2006a). In addition to the long-term tectonic processes acting upon this environment, mega-earthquakes along the subduction zone are the expression of processes in the forearc above the interplate coupling zone. This setting in south-central Chile is very similar to the Cascadia subduction zone in North America (e.g. Atwater et al., 1992; Barrientos et al., 1992; Cattin et al., 1997; Wells et al., 2003; Lomnitz, 2004; Fuller et al., 2006;

Melnick et al., 2006). The largest earthquake ever recorded occurred in south-central Chile in 1960 (Plafker and Savage, 1970). This event ruptured about 1000 km of the main thrust between  $\sim 38^\circ$  and  $\sim 44^\circ$ S and was accompanied by significant coseismic uplift and subsidence in the forearc (Plafker and Savage, 1970; Cifuentes, 1989; Barrientos and Ward, 1990; Krawczyk and SPOC-Team, 2003). Thus, from a landscape-evolution viewpoint and the importance of processes on long time scales, but also from an earthquake-hazard perspective, it is extremely important to understand the overall tectonic and geomorphic behavior of forearc regions, because it may also provide clues regarding the seismotectonic behavior of the margin on much shorter time scales, involving hundreds of years, which is thus relevant for humans.

Despite the need to better understand these complex relations, our knowledge of the interaction between subduction and surface processes and their manifestation in the character of seismo- and morphotectonic segmentation of forearc regions is still scarce. This also applies to the effects of climate-related forcing of the tectonic system and the nature of disparate deformation and uplift, as well as subsidence patterns of forearc regions. Consequently, it is not fully understood yet a) what controls the long-term evolution of morphotectonic segments; b) over which time scales this segmentation is maintained; c) how the segments are related to earthquake-rupture zones; and d) which influence the subduction mode has on the segmentation and the overall deformation pattern in the forearc. In addition, a related question concerns the climatic control of certain geomorphic features and landscapes, especially in mountainous terrains. In order to contribute to solving these issues this thesis aims to answer some of these questions by investigating the Central to Southern Andean margin on different spatial and temporal scales, combining geomorphology, geochronology, sedimentology, and morphometry.

After an introduction to the regional geodynamic, geologic, and climatic setting I present the results of my research in form of four individual, yet related chapters (3 to 6). Each of these chapters constitutes a manuscript that has been or is in the process of being submitted. Chapter 3 has already been published. In chapter 7, the last chapter of this thesis, I summarize the final conclusions of my studies.

In chapter 3, I conducted a morphometric analysis of the Chile margin between  $37^\circ$  and  $41^\circ$ S in order to characterize and define forearc segments by investigating topography and fluvial systems. I identified different segments that record a distinct geomorphic and tectonic evolution. Subsequently, I discuss the persistence of this morphotectonic segmentation and the relation to short-lived earthquake-rupture zones. However, it remained an open question, when the morphotectonic segmentation was established, which appears to be closely related to the onset of uplift of the Coastal Cordillera.

In chapter 4, I focus on one morphotectonic segment that undergoes active uplift in order to reconstruct the evolution of the Coastal Cordillera on a timescale of  $10^6$  years. The highest sectors of the Coastal Cordillera around  $38^\circ$ S comprise an extensive, well-preserved erosion surface. Applying  $^{10}\text{Be}$  and  $^{26}\text{Al}$  cosmogenic-nuclide dating, I derive information on the initiation of range uplift as well as an uplift rate. Furthermore, I integrate these results in the regional tectonic context and discuss, whether onshore and offshore forearc sectors uplifted contemporaneously. I also address the question whether range uplift is related to a shift from subduction erosion to subduction accretion about 5 Ma ago, possibly related to the onset of global cooling and glaciations in this sector of the Andes.

Interestingly, the uplift rates I derived from cosmogenic-nuclide dating are significantly lower than late Quaternary uplift rates calculated from geomorphic markers, such as marine terraces. This indicates that uplift might have accelerated through time, which would have important implications for the tectonic evolution of the

forearc. Hence, in chapter 5, I present the dating of fluvial as well as alluvial sediments and geomorphic surfaces in order to quantify uplift and incision rates on a time scale of  $10^5$  years. This enables me to pin the age of tectonically controlled stream piracy, compare uplift rates derived by independent methods averaging over different timescales, and discuss landscape evolution in light of tectonic and climatic forcing.

Chapters 4 and 5 emphasize the importance of climate as a factor that significantly influences the geomorphic development of the Chile forearc, particularly with respect to the topography and morphology. Nevertheless, in general there is still no consensus for this and adjacent regions about how topography and relief are in fact shaped by climate, e.g. the overall evolution of surface processes determined by rainfall vs. glaciation. In chapter 6 I therefore analyze geometry, relief, and climate parameters of 120 drainage basins along the watershed of the western Andean flank between  $15.5^\circ$  and  $41.5^\circ\text{S}$  in order to contribute to the understanding of the climatic control on drainage-basin morphology. I identify segments characterized by different relief and topography and discuss them in relation to varying surface processes and transient landscapes.

Chapter 3 (“Morphotectonic segmentation of an active forearc,  $37^\circ - 41^\circ\text{S}$ , Chile” by Katrin Rehak, Manfred R. Strecker, Helmut P. Echtler) is published in *Geomorphology* 94 (1-2). Chapter 4 (“Reconstructing surface uplift using cosmogenic nuclides - the Coastal Cordillera in south-central Chile” by Katrin Rehak, Manfred R. Strecker, Helmut P. Echtler, Steve Binnie, Michael A. Summerfield, Tibor Dunai, Stuart Freeman) has been submitted to the journal *Earth Surface Processes and Landforms*. Chapter 5 (“Late Pleistocene landscape evolution in south-central Chile constrained by luminescence and stable cosmogenic isotope dating” by Katrin Rehak, Manfred R. Strecker, Helmut P. Echtler, Samuel Niedermann, Frank Preusser) will be submitted to GSA Bulletin. Chapter 6 (“Climatic controls on drainage-basin morphology - the western Andean flank between  $15.5^\circ$  and  $41.5^\circ\text{S}$ ” by Katrin Rehak, Bodo Bookhagen, Manfred R. Strecker, Helmut P. Echtler) is in submission to the journal *Earth Surface Processes and Landforms*.

## 2. Regional setting

### 2.1 Geodynamic framework

The western margin of the South American continent comprises the Andes, the world's longest mountain chain, and the type subduction orogen (e.g. Mitchell and Reading, 1969; Dewey and Horsfield, 1970; Windley and Smith, 1976). The study area is located in Chile; with 4300 km length, the Andean margin of Chile spans more than 38° of latitude from 17.42°S northeast of Arica to 55.98°S at Cape Horn. Being among the seismically most active regions in the world, Chile experienced the largest earthquake ever recorded, the Valdivia-earthquake at approximately 38°S with a  $M_w$  of 9.5 that occurred on May 22, 1960 (Plafker and Savage, 1970; Barrientos and Ward, 1990; Engdahl and Villasenor, 2002; Krawczyk and SPOC-Team, 2003).

The evolution of the Andes is closely related to the subduction of the oceanic Nazca Plate beneath the South American continent since ~300 Ma, inherited basement anisotropies, and pronounced north-south-gradients in climate and erosion (Schwerdtfeger, 1976; Mpodozis and Ramos, 1989). Both lithospheric plates converge obliquely at N77°E with a rate of currently 66 mm a<sup>-1</sup>, indicated by GPS modeling data (Angermann et al., 1999; Kendrick et al., 2003). Although the entire margin undergoes subduction at a spatially similar convergence rate and direction, the Andes are characterized by pronounced along-strike differences in topography, architecture, total shortening, and mode of deformation (e.g. Mpodozis and Ramos, 1989; Dewey and Lamb, 1992; Kley et al., 1999; Montgomery et al., 2001; Moreno and Gibbons, 2007). The factors controlling this segmentation are manifold and still a matter of debate. In fact, the segmentation of the Andes into distinct morphotectonic provinces has been related to longitudinal changes in dip and age of the Nazca plate (Jordan et al., 1983), characteristics of the pre-Andean continental basement (Mpodozis and Ramos, 1989), and zonal climatic gradients (Montgomery et al., 2001).

The central part from 14° to 27°S is characterized by crustal shortening in the Western Cordillera, the Subandean Ranges, and the internally drained Puna-Altiplano Plateau (Mpodozis and Ramos, 1989). The flat-slab segment of the Nazca Plate between 27° and 33.5°S exhibits no Quaternary volcanism (Jordan et al., 1983; Kay and Mpodozis, 2002; Ramos et al., 2002). This region comprises the broken-foreland province of the Sierras Pampeanas experiencing active shortening and destructive earthquakes (Jordan and Allmendinger, 1986; Allmendinger et al., 1990). South of ~31°S, Cenozoic total shortening is significantly reduced and generally decreases southwards from ~300 km in the Central Andes to only ~15 km in the Northern Patagonian Andes (Isacks, 1988; Allmendinger et al., 1990; Diraison et al., 1998b; Kley et al., 1999; Oncken et al., 2006; Vietor and Echtler, 2006). GPS measurements corroborate this pattern and document higher shortening rates in the Central Andes compared to adjacent regions (Dewey and Lamb, 1992; Klotz et al., 2001; Brooks et al., 2003). Major transitions along the Central to Southern Andes occur at 33°S, where the southern end of the flat-slab segment and the collision of the Juan-Fernández Ridge coincide, and at 38°S, the northern limit of the Patagonian Andes that delineates significant changes in kinematics and the degree of strain partitioning (e.g. Jordan et al., 1983; Mpodozis and Ramos, 1989; Dewey and Lamb, 1992; Hervé, 1994; Lavenu and Cembrano, 1999; Kay and Mpodozis, 2002; Ramos et al., 2002; Rosenau et al., 2006). South of 37°S strain partitioning, controlled by the Liquiñe-Ofqui strike-slip fault zone that developed during the latest Miocene due to changes in plate-convergence obliquity, is responsible for decoupling the forearc and

the retroarc, this resulted in minimum shortening and deformation of the foreland (Dewey and Lamb, 1992; Hervé, 1994; Diraison et al., 1998a; Somoza, 1998; Lavenu and Cembrano, 1999).

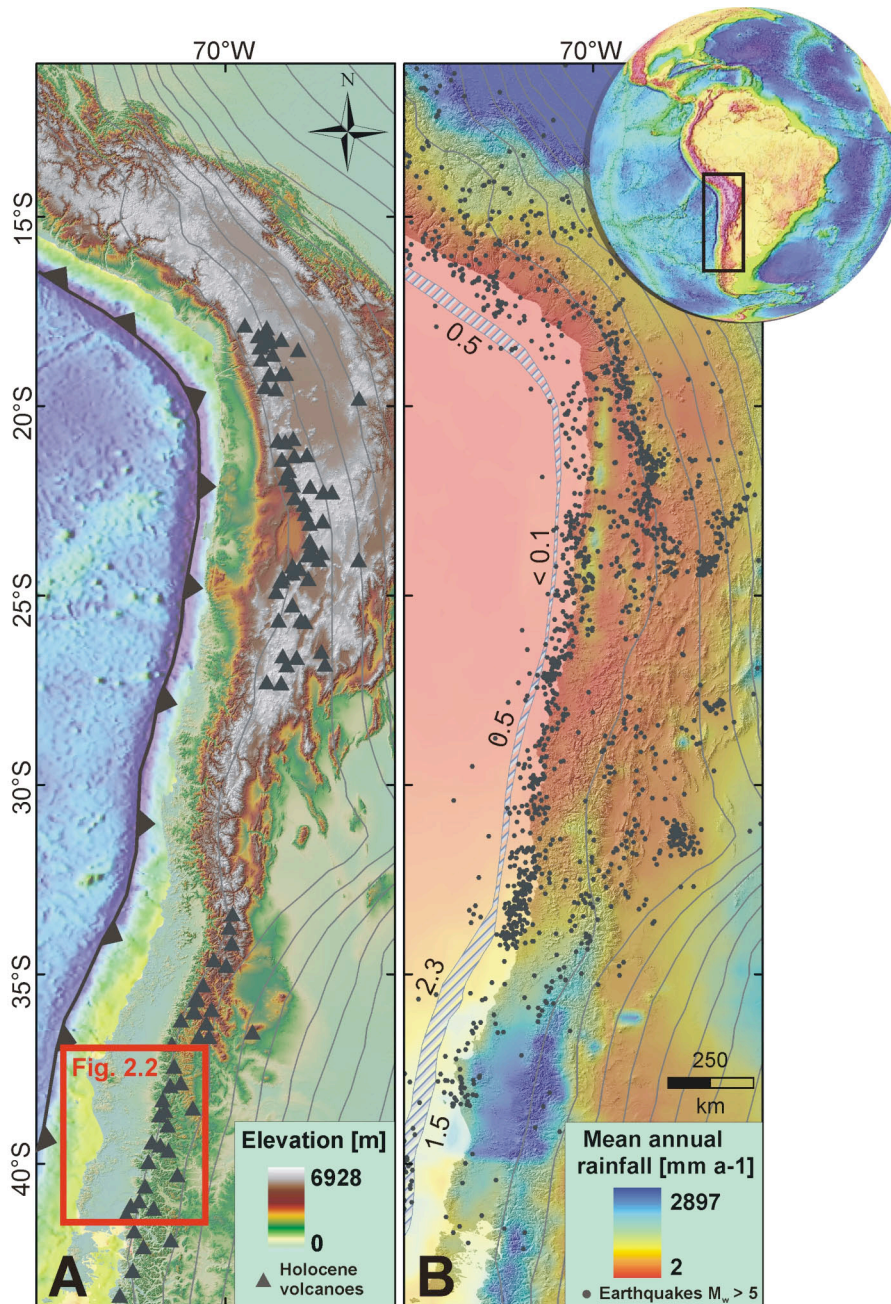


Fig. 2.1: Topography, geodynamic setting, and rainfall pattern along the Central to Southern Andes. (A): DEM with Holocene volcanoes marked with black triangles and slab depth depicted in grey 100-km-contours (modified after Tassara et al., 2006). Note the flat-slab segment between 27° and 33.5°S showing no Quaternary volcanism. (B): Mean annual rainfall (TRMM, 2007) with earthquakes  $M_w > 5$  denoted as grey dots (after Engdahl et al., 1998), trench-fill thickness in km marked by the shaded strip (modified after Bangs and Cande, 1997), and slab depth in grey contours.

Surface uplift and shortening of the Andean mountain range was initiated in the Eocene to Miocene, starting in the Central Andes and propagating southwards (Allmendinger et al., 1990; Jordan, 1993; Kley and Monaldi, 1998; Oncken et al., 2006). Whereas parts of the Central Andean region now constituting the Altiplano-Puna Plateau have been proposed to have started uplifting already in the Oligocene

(Allmendinger et al., 1997; Carrapa et al., 2005; Elger et al., 2005; Garziona et al., 2006; Oncken et al., 2006), extensional basins and syn-contractual deposits south of 33°S document surface uplift only between 16 to 6 Ma (Jordan et al., 2001; Giambiagi et al., 2003; Vietor and Echtler, 2006). Here, paleo-elevation data indicate > 1 km of surface uplift in the Patagonian Andes between ~ 16 to 14 Ma, establishing the orographic rain shadow on the eastern side of the range (Blisniuk et al., 2005). Approximately at the same time, pronounced exhumation in the Patagonian Andes started 16 to 10 Ma ago as constrained by thermochronological data (Thomson, 2002; Adriasola et al., 2006).

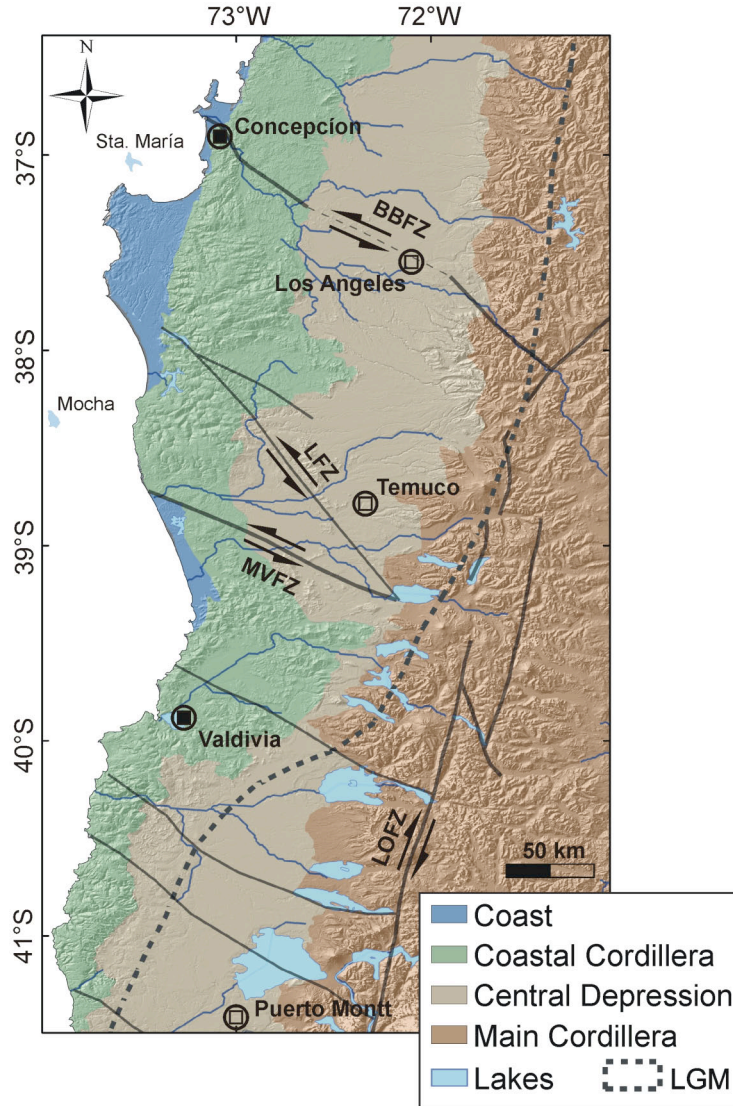


Fig. 2.2: Morphotectonic units of the south-central Chile margin with fault zones (modified after Melnick and Echtler, 2006b). The stippled line delineates the glacier extent during the LGM (after Rabassa and Clapperton, 1990).

In my thesis, I mainly concentrate on southern Central Chile, particularly the VIII. Región del Bío-Bío and the IX. Región de la Araucanía in south-central Chile around 38° to 39°S. Southern Central Chile is differentiated in four trench-parallel morphotectonic units that are representative for large parts of the Andean margin: (1) Coastal Platform, (2) Coastal Cordillera, (3) Central Depression, and (4) Main Cordillera (Fig. 2.2) (Darwin, 1846; Brügggen, 1950; Gansser, 1973; Jordan et al., 1983; Mpodozis and Ramos, 1989). I mainly focus on the Coastal Cordillera which consists of high-temperature metamorphic rocks and a Carboniferous granitic batholith constituting a Permo-Triassic accretionary wedge and parts of a Permo-

Carboniferous magmatic arc, respectively (Hervé, 1977; Glodny et al., 2005). Both lithologic units became juxtaposed by the Paleozoic reactivated Lanalhue strike-slip fault (Fig. 2.2) (Glodny et al., in press). Other prominent north-west striking fault zones traversing the Coastal Cordillera are the Bío-Bío and the Mocha-Villarica fault zones (Fig. 2.2) (Melnick and Echtler, 2006b).

The morphology of the coastal sectors and ranges is characterized from west to east by flights of marine terraces, well-preserved erosion surfaces atop the Coastal Cordillera, and extensive depositional surfaces and gravel fills in the Central Depression. The staircase morphologies and severe drainage re-adjustments in this region emphasize the high degree of tectonic activity of the southern Chile margin, which is also expressed in a cluster of seismicity associated with faulting (Bohm et al., 2002; Haberland et al., 2006) and pronounced coseismic deformation during megathrust events, such as in 1960 (Kaizuka et al., 1973; Barrientos and Ward, 1990; Nelson and Manley, 1992; Cisternas et al., 2005). Hence, the south-central Chile forearc constitutes an ideal setting to investigate the relationship between tectonic, geomorphic, and climatic processes on different time scales.

## 2.1 Climatic conditions

The climate of Chile represents an outstanding range of temperature and rainfall regimes from the hyperarid, subtropical Atacama Desert in the north around 22°S to year-round humid and subantarctic conditions south of 40°S and associated orographic effects (Schwerdtfeger, 1976). Mean annual precipitation increases from virtually zero in the core of the desert to more than 5000 mm a<sup>-1</sup> in the luff of the Andes south of 40°S (Fig. 2.1) (New et al., 2002; TRMM, 2007). In the north, precipitation is delivered by the low-level Andean Jet from the east, whereas in the south, it is supplied by the Westerlies. However, due to the high topography of the Central Andes with summit elevations reaching 7000 m, moisture from the east is efficiently blocked. Additionally, the upwelling cold Humboldt Current generates climatic inversions and thus prevents convection of moist air masses. In addition to the latitudinal position, this constellation promotes the hyperaridity on the western flank of the Central Andes. In contrast, precipitation in the south is directly related to frontal passages of cyclones that occasionally penetrate into the semiarid regions as far north as 27°S during mid-winter (Schwerdtfeger, 1976).

My study area is located in the transition between winter-rain subtropical and year-round humid, temperate climate conditions around ~38°S. The region is alternately influenced by the subtropical Pacific anticyclone in summer and outer-tropic cyclones during winter (Weischet, 1970; Mardones and Reuther, 1999). Characteristic for the southern subtropics, this region is subjected to episodic high-magnitude rainfall events (Weischet, 1970). Mean annual rainfall averages between 1000 to 2500 mm a<sup>-1</sup>, depending on the wind position to the Coastal Cordillera.

The regional climatic zonation is controlled by long-lived, hemisphere-scale circulation patterns. Humid conditions in the southern Central Andes determined by the Westerlies have probably existed since middle Miocene similar to the hyperarid desert which persisted since at least 10 to 14 Ma (Haselton et al., 2002; Hartley, 2003; Blisniuk et al., 2005; Dunai et al., 2005; Nishiizumi et al., 2005; Rech et al., 2006). Related to global cooling, Patagonian glaciation started 5 to 7 Ma ago (Mercer and Sutter, 1982; Zachos et al., 2001; Rabassa et al., 2005). Whereas south of 40°S the Patagonian ice reached the foothills of the Coastal Cordillera and successively the Pacific coast, the Coastal Cordillera and the Central Depression north of 40°S remained free of glaciers during Quaternary (Fig. 2.2.) (Rabassa and Clapperton, 1990; Clapperton, 1993; Clapperton, 1994). However, the Main Cordillera in south-

central Chile currently is and was partly influenced by valley and cirque glaciers (Rabassa and Clapperton, 1990).

The spatial distribution of precipitation and related intensity of erosion along the Andean margin is reflected by the thickness of the terrigenous sediment fill in the trench off South America (Fig. 2.1). Longitudinal sediment transport in the trench, however, is also inhibited by the Juan-Fernández Ridge, thus promoting sediment accumulation south of the ridge, while northern areas are sediment starved due to the combined effects of the moisture barrier and latitude-controlled aridity (Bangs and Cande, 1997). It has been proposed that the thickness of sediments in the trench exerts a first-order control on the subduction mode by lubricating the plate interface and thus decreasing shear stresses suggesting a mechanism, how climate might influence tectonic systems (Lamb and Davis, 2003; Melnick and Echtler, 2006a).

### 3. Morphotectonic segmentation of an active forearc, Chile (37°-41°S)

#### Abstract

*Many forearc-regions are characterized by seismo- and morphotectonic segments that may record recurring activity of large earthquakes in the past. It is very important, from a landscape development as well as from an earthquake-hazard perspective, to understand the evolution of such forearc segmentation. However, it is not well known on which timescales forearc segments retain their tectono-geomorphic identity, how they are related to earthquake rupture zones, and what may govern their long-term evolution. The forearc of the active convergent margin of south-central Chile (37°-41°S) is located within the rupture zone of the Chilean 1960 megathrust earthquake. We combine geomorphological and sedimentological analysis, as well as structural and geophysical data to reconstruct the morphotectonic evolution of this forearc setting.*

*Our data documents that the southern Chile forearc is segmented into three sectors (Nahuelbuta, Toltén and Bueno segments) that define a semi-independent structural and geomorphic evolution. Whereas the Toltén segment appears to be quasi-stable, the other two segments record pronounced Quaternary uplift. The Nahuelbuta and Bueno segments are characterized by broad, north-south oriented antiformal structures with numerous anomalies in the highly dynamic fluvial network implying severe drainage modifications and sediment rerouting. The morphotectonic segmentation is compatible with structural, seismic, and gravimetric characteristics.*

*Apparently, this morphotectonic segmentation is persistent over timescales of  $10^4$  to  $10^6$  years. This contrasts with transient earthquake rupture zones that exhibit short-term variability over  $10^2$  to  $10^3$  years and may rupture beyond the morphotectonic boundaries. We propose that the differential forearc evolution is focused by inherited upper-plate structures, but appears to be ultimately controlled by characteristics of the highly inhomogeneous subducting plate, as well as rheological properties of the forearc.*

**KEYWORDS:** *tectonic geomorphology, drainage basins, topography, forearc evolution, morphometry*

#### 3.1 Introduction

Forearc regions constitute one of the tectonically most active areas of plate boundary settings (e.g. in South America, Cascadia, Nankai or New Zealand), and are often associated with large, destructive earthquakes, concomitant deformation, uplift, or subsidence, resulting in pronounced contrasts in relief, changes in drainage networks, and variations in surface processes and rates (Ruff and Kanamori, 1989; Atwater, 1992; McCaffrey, 1993; Klotz et al., 2001; Pazzaglia and Brandon, 2001; Clift et al., 2003; Cisternas et al., 2005). Typically, forearc regions are segmented into semi-

independent seismotectonic segments that may correspond to rupture segments of large earthquakes (Mogi, 1969; Taylor et al., 1987). It is not known however, if such rupture segments are being sustained on timescales involving several  $10^3$  to  $10^6$  years or if they rather represent transient phenomena (Machette et al., 1991; Lomnitz, 2004; Lee and Yang, 2006). Another unresolved question concerning the evolution of active forearc regions is as to what extent landscape evolution and tectonic segmentation may be controlled by the characteristics of the subducting plate or by inherited structures of the upper plate. In this respect, it is interesting that earthquake ruptures in forearc settings may be limited by segment boundaries that are determined by crustal anisotropies (Lay et al., 1982). Therefore, it is important to understand the nature of forearc deformation and the processes that drive forearc segmentation as well as to define how persistent these segments are. Indeed, landscapes are sensitive recorders of tectonic processes and spatiotemporal variability in tectonism on various timescales, and may thus provide valuable information on the nature of seismotectonic segmentation.

Forearc studies in different regions have revealed that the subduction of topographic features, such as ridges, fracture zones or seamounts causes significant, although very localized surface-uplift anomalies (McCann and Habermann, 1989; Gardner et al., 1992; Machare and Ortlieb, 1992; Gutscher et al., 1999; Hampel et al., 2004). In addition, modeling studies suggest that basal sediment underplating and frontal accretion may cause spatially and temporally variable surface uplift signals in the upper plate (Lohrmann, 2002). Notwithstanding, in most forearc environments the controls and dynamics of deformation and segmentation remain elusive or have not been fully understood yet.

Along the coast of south-central Chile the largest earthquake ever recorded ruptured a zone between  $\sim 37^\circ$  and  $46^\circ\text{S}$  in May 1960 (Plafker and Savage, 1970). Although this extensive rupture zone suggests a more or less homogeneous plate interface along this margin, the morphology and tectonics of the regional forearc appear to be highly differentiated. This part of the Chile plate margin is thus an ideal natural laboratory to evaluate forearc segmentation, topography, and landscape evolution in relation with subduction processes.

Here, we use geomorphologic, sedimentologic, and compiled structural, as well as geophysical data to propose a model for dynamic forearc segmentation and uplift distribution in south-central Chile between  $37^\circ$  and  $41^\circ\text{S}$  and discuss their controlling parameters. In particular, we use drainage network analysis combined with sediment provenance, gravimetric modeling data (Tašárová, 2004; Hackney et al., 2006), and seismicity patterns (Engdahl et al., 1998; Bohm et al., 2002; Bruhn, 2003; Bohm, 2004; NEIC, 2006) to decipher the evolution of this actively deforming segment of the forearc of Chile.

We demonstrate that the forearc in this environment is segmented into three distinct sectors, each undergoing a semi-independent tectonic and morphologic evolution. Compared to the long-term regional forearc segmentation, earthquake rupture segments represent rather transient, second-order phenomena.

### 3.2 Regional tectonic setting

The active margin of south-central Chile (Fig. 3.1) is characterized by the fast oblique ( $\text{N}77^\circ\text{E}$ ) subduction of the oceanic Nazca Plate beneath South America, megathrust earthquakes (Cisternas et al., 2005), and a convergence rate of approximately 65 to 85

mm a<sup>-1</sup> (Demets et al., 1994; Somoza, 1998; Angermann et al., 1999). Although the Neogene-Quaternary accretionary wedge at the Arauco Peninsula at about 38°S records alternating phases of subduction erosion and accretion, the size of the accretionary prism as well as the thickness of the trench fill that has accumulated since the late Miocene suggest that this sector is in an accretional or at least non-erosional mode (Bangs and Cande, 1997).

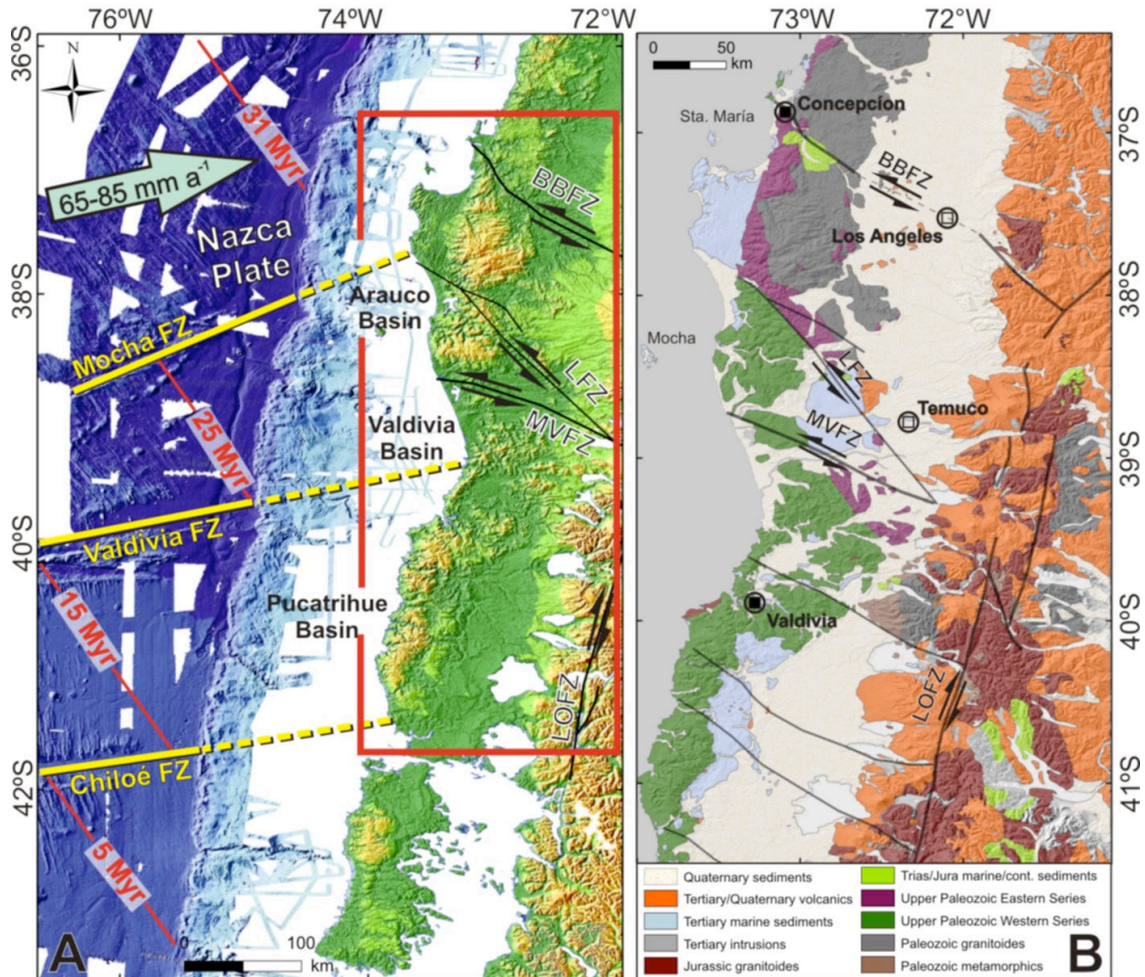


Fig. 3.1: A: Topography, bathymetry, and geology of south-central Chile. Segmentation of the Nazca Plate, ocean floor ages (in Ma) and main fault zones of the South American Plate (Tebbens and Cande, 1997). Oceanic plate structures are outlined in yellow, continental plate structures are outlined in black. The red rectangle delineates the extent of (B). B: Geology and major structural features of the study area (modified after Sernageomin (2003) and Mordojovich (1981)).

The offshore area of south-central Chile comprises several forearc basins (Arauco, Valdivia and Pucatrihue basins) (Fig. 3.1) (Mordojovich, 1981). South of 38°S the incoming plate is segmented by several fracture zones (Fig. 3.1). The northeast-striking Mocha fracture zone (FZ) at 38°S currently subducts obliquely beneath the Arauco peninsula. The almost trench-normal Valdivia FZ system at about 40°S and the oblique Chiloé FZ at about 42°S also intercept the plate margin. As a result of their obliquity with respect to the orientation of the trench these fracture zones migrate southward at rates between 40 (Mocha FZ) to 8 mm a<sup>-1</sup> (Valdivia FZ) (Vietor et al., 2005). In addition, the Valdivia FZ system separates younger, and therefore, more buoyant oceanic crust generated at the Chile Rise to the south, from older ocean floor generated at the East Pacific Rise to the north (Nelson and Manley, 1992; Tebbens and Cande, 1997).

The onshore part of south-central Chile consists of three major morphotectonic and structural provinces: the Coastal Cordillera in the west, the north-south oriented Central Depression, and the Main Cordillera in the east (Fig. 3.1). The Coastal Cordillera constitutes a Paleozoic-Triassic forearc complex, including rocks related to a Permo-Triassic accretionary wedge and parts of a Permo-Carboniferous magmatic arc (Hervé, 1977; Glodny et al., 2005) that are grouped into an Eastern and a Western Series, respectively (Fig. 3.1). At about 37.5°S the Eastern Series of the Cordillera de Nahuelbuta is dominated by high-temperature metamorphic rocks and a Carboniferous granitic batholith. Farther south, at about 41.5°S, the Western Series consists mainly of high-pressure schists, metabasites, and accreted metacherts (Aguirre Le-Bert et al., 1972; Hervé, 1977). Apatite fission track data indicates ongoing exhumation of the paleo-accretionary wedge since Eocene time with exhumation rates of  $0.04 \pm 0.01 \text{ mm a}^{-1}$  (Glodny et al., 2005).

The marine platform units of the Arauco Peninsula are predominantly composed of Cretaceous to Quaternary marine and continental sedimentary sequences bounded by NW-striking, crustal-scale basement discontinuities. In these basins, episodes of subsidence and sedimentation have alternated with uplift and erosion (Pineda, 1986), possibly related to cycles of tectonic accretion and erosion (Bangs and Cande, 1997; Melnick and Echtler, 2006a).

The Coastal Cordillera in the study area is characterized by numerous north-northeast, west and northwest oriented reactivated Paleozoic faults with strike-slip kinematics (Mordojovich, 1981; Echtler et al., 2003; Rosenau, 2004). The most prominent structures are the Bío-Bío fault, the Lanalhue fault zone separating the Eastern from the Western Series, and the Mocha-Villarica fault zone (Fig. 3.1).

The Arauco Peninsula and the Cordillera de Nahuelbuta are characterized by flights of multiple terraces, reaching elevations of up to 900 m. The terraces are tilted along a northwest-southeast oriented uplift axis, which passes through the Arauco Peninsula and the highest summits of the Cordillera de Nahuelbuta (Kaizuka et al., 1973). Terrace levels on Arauco at elevations of up to 500 m are covered by marine Tertiary sediments suggesting an origin as marine abrasion platforms (Mardones and Reuther, 1999) indicating uplift, superposed oscillating sea-levels, and erosion during and since the late Pliocene (Plafker and Savage, 1970; Kaizuka et al., 1973; Nelson and Manley, 1992; Kelm et al., 1994). In contrast, erosion surfaces higher than 500 m lack any evidence of marine origin and were interpreted as fluvial erosion surfaces (Kaizuka et al., 1973). Based on analogue modeling, Lohrmann (2002) proposed that basal accretion and antiformal stacking at the plate interface at depth in this environment may cause such differential uplift. Furthermore, inherited upper plate structures independent of accretionary processes might locally influence the locus of deformation (Echtler et al., 2003).

### 3.3 Methods

We use morphometric analyses, geomorphological and sedimentological field observations, as well as compiled structure, gravimetry and seismicity data to define the structure and long-term forearc tectonics of the south-central Coastal Cordillera. Corrected SRTM-90 m interferometry elevation data, ASTER and LANDSAT satellite images, and aerial photos at a scale of 1:70 000 serve as database.

Using common algorithms (O'Callaghan and Mark, 1984; Jenson and Domingue, 1988; Tarboton et al., 1991), the drainage network was digitally extracted and

watersheds were delineated to perform detailed basin and topography analyses. This derived channel network was validated with rivers delineated on georeferenced topographic maps (1:50000). Based on these data, morphometric properties such as area-elevation relations, swath profiles, steepness, and local relief were calculated to identify topographic anomalies and incising high-relief areas. In active tectonic settings, such areas commonly correlate with regions of ongoing rock uplift (Molin et al., 2004). Swath profiles were created along 75 and 40 km wide bands across the Coastal Cordillera. Steepness maps were interpolated from area-slope data of all channels with a best-fit  $\theta$  of 0.2, which was derived from regressions. To create local relief maps, we subtracted maximum and minimum elevations averaged over a 4.5-km-radius circle. This procedure helps discriminate areas of different erosional, and possibly, tectonic activity.

Longitudinal river profiles, profile-concavity indices, as well as DS (downstream distance – slope) plots of drainage basins were generated to detect anomalies and modifications in the stream network, including knickpoints, stream captures and low-/high-slope river segments. DS plots display the slope of a stream segment as a function of the segment's downstream distance related to the stream profile in a log-log space. This approach is helpful in identifying and discriminating knickpoints (Bishop and Goldrick, 2000). The profile concavity index (PCI) is used to quantify the general shape of a stream long profile. Following Demoulin (1998) we normalized the distances and elevations of all profiles to 1 and calculated the PCI as the ratio of the area under this normalized profile to the area of a virtual triangle linking the divide and mouth of the river (PCI = 0.5).

We also tested our morphometric results in the field. Based on prior evaluation, the channel showing the most severe drainage modifications was chosen for detailed mapping of fluvial sediments and terraces to determine paleo-channels and drainage network changes along the Tirúa-Pellahuén valley (Fig. 3.2). We distinguished fluvial terrace remnants by comparing their sediment composition applying provenance analysis via pebble counting, and determined paleo-flow directions by measuring pebble imbrications. Finally, we combined our geomorphic data with regional structural data (Echtler et al., 2003; Rosenau, 2004), bathymetry (Bangs and Cande, 1997), ocean-floor characteristics (Tebbens and Cande, 1997), gravimetry (Tašárová, 2004; Hackney et al., 2006), and earthquake data from global catalogues (Engdahl et al., 1998; NEIC, 2006), as well as local seismicity networks (Bruhn, 2003; Bohm, 2004) to better evaluate the influence of the incoming and upper plate characteristics on segmentation.

### 3.4 Results

#### 3.4.1 Drainage network analysis and sedimentological observations

The analysis of digital elevation models as well as geomorphic and structural field observations reveal three major morphologic domains along the studied area of the Coastal Cordillera: two higher-elevation areas approximately at the latitudes of 38°S and 41°S, which we term the Nahuelbuta and Bueno segments, reaching elevations of 1500 m and 1000 m, respectively. These ridges run parallel to the coastline and have an ellipsoidal shape (Fig. 3.3). These high-elevation domains are adjacent to a central, low-elevation domain with an average elevation of 60 m, referred to as the Toltén segment (Fig. 3.3). The Nahuelbuta segment is limited by the Río Bío-Bío in the north

and the Río Imperial in the south. The Río Imperial also borders the Toltén segment in the north. In turn, the Río Calle separates the Toltén and the Bueno segments (Fig. 3.2). The southern limit of the Bueno segment is the Chiloé gulf, where the Coastal Cordillera loses its topographic expression in the transition to the Patagonian archipelago.

This first-order segmentation is also documented by the local relief and steepness maps (Fig. 3.3). Both define an area of high incision and pronounced relief contrasts in the north (Nahuelbuta segment), bordered by a low-relief area to the south (Toltén segment), which in turn is limited by an area of increasing elevation and incision to the south (Bueno segment). The swath profiles of the two high-relief segments, showing the maximum, mean and minimum elevation from north to south, support these assessments (Fig. 3.3). Furthermore, our field observations in the Nahuelbuta segment revealed the existence of north and south-tilted erosion surfaces to the north and south of the highest summits, respectively.

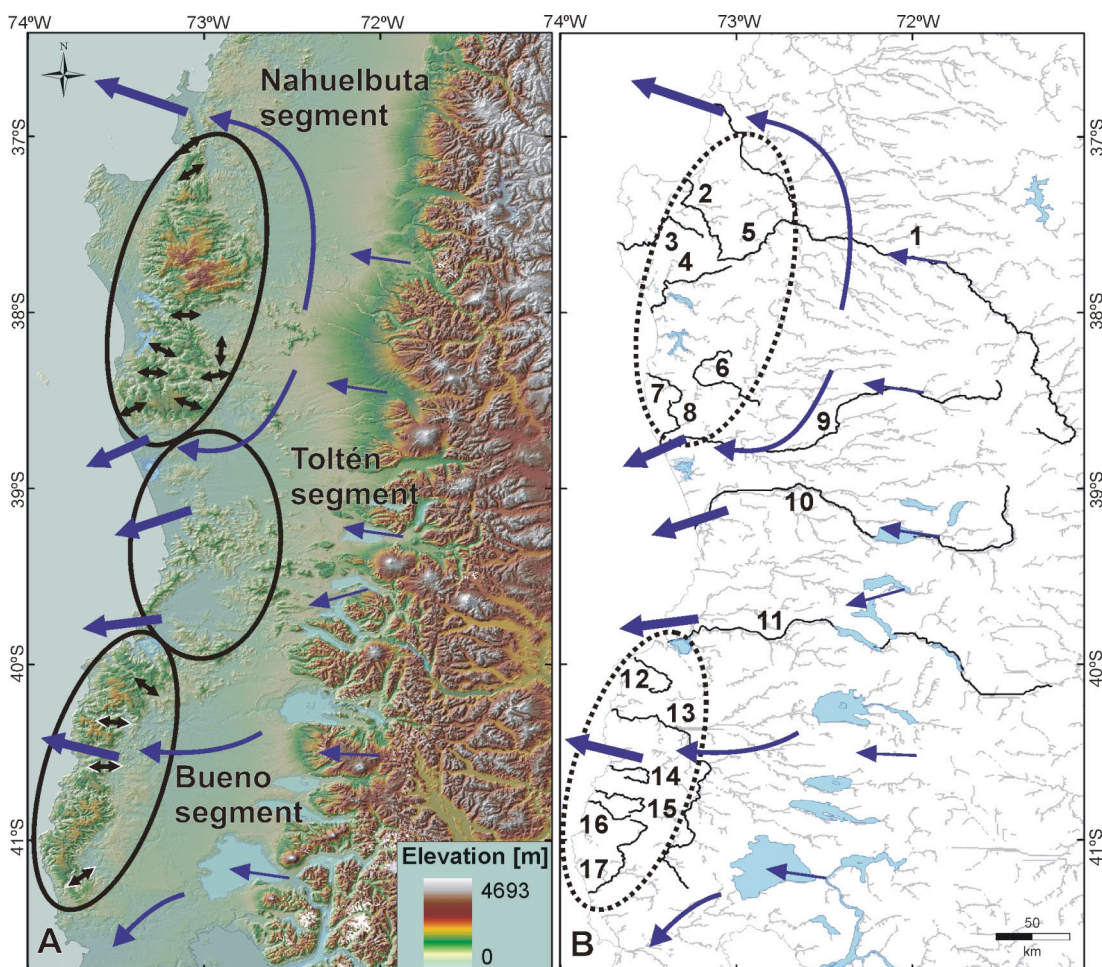
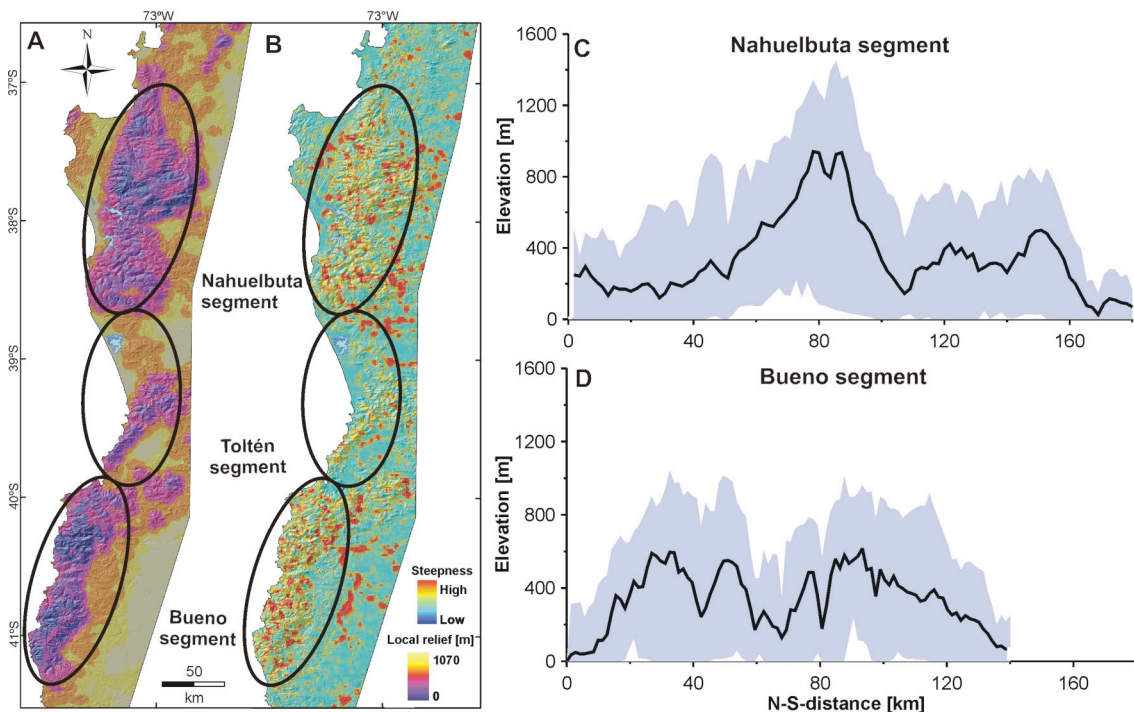


Fig. 3.2: Segmentation and drainage evolution of the south-central Chilean Coastal Cordillera – morphotectonic segments and analyzed stream profiles. (A): Shaded-relief DEM showing the morphotectonic forearc segments marked by black ellipses. Black arrows assign wind gaps, white-framed arrows depict zero-slope channel segments. Arrows point in flow direction. Blue errors delineate discharge routing. (B): Drainage network in the three morphotectonic segments, numbers mark analyzed stream profiles (1 Bío-Bío, 2 Carampangue, 3 Lebu, 4 Cayucupil/Paicaví, 5 Tavoleo, 6 Pellahuén, 7 Tirúa, 8 Moncul, 9 Imperial, 10 Toltén, 11 Calle, 12 Chaihuín, 13 Bueno, 14 Pucatrihue/Contaco, 15 Llesquehue, 16 Cruces, 17 Llico). Note that rivers in the Nahuelbuta and Bueno segments are mainly locally sourced in the Coastal Cordillera to the west, whereas large rivers originating in the Main Cordillera in the east concentrate in the Toltén segment.

The segmentation is reflected in the drainage-basin characteristics as well (Table 3.1). In general, the forearc drainage is manifested in a grid-iron pattern. Broad, swampy areas and low-slope streams that integrate large drainage basin areas characterize the Toltén segment. Conversely, the Nahuelbuta and Bueno segments record severe reorganizations of the drainage network, including wind gaps, anomalous river gradients, knickpoints, flow reversals, and stream captures (Fig. 3.2 and 3.4).

The Coastal Cordillera is primarily drained by locally sourced rivers and therefore characterized by small drainage basins (Fig. 3.2). There are only few large rivers capable of cutting through the Coastal Range. From north to south these are the Bío-Bío, Imperial, Toltén, Calle and Bueno rivers, all characterized by large contributing areas in the Main Cordillera to the east that receive high amounts of precipitation (Fig. 3.2). Three of them, the Imperial, Toltén and Calle rivers, flow in the low-relief Toltén segment where the Coastal Range has no significant topography. Thereby, these rivers route discharge and sediment transport from the Main Cordillera and the Central Depression to singular outlets in the Toltén segment and the northern terminus of the Nahuelbuta segment (Fig. 3.2).

The Nahuelbuta segment is mainly drained by rivers associated with six small local basins, beside the Río Bío-Bío in the north and the Río Imperial in the south (Fig. 3.2). In this segment we identified nine wind gaps that are systematically distributed in east-west oriented valleys (Fig. 3.2). The wind gap between the Tirúa and Pellahuén basins is the most striking paleo-drainage feature of the Nahuelbuta segment. Longitudinal channel profiles, slope indices, and digital drainage network analysis indicate a flow reversal about 10 km inland of the Río Pellahuén that formerly drained toward the Pacific. At present, this river traverses the entire Coastal Cordillera with a slope of less than 0.004 % (Fig. 3.5) and drains eastward into the Central Depression.



**Fig. 3.3:** (A) Local relief map and (B) steepness map showing high-relief clusters in the Nahuelbuta and Bueno segments. Local relief is averaged over a radius of 4.5 km. Steepness is interpolated based on area-slope regressions for all channels with a  $\theta$  of 0.2. (C) and (D) Swath profiles of the high-relief segments marked in (A) with ellipses, plotting regional minimum, mean, and maximum elevations.

Basin	Strahler order	Basin area [km <sup>2</sup> ]	Basin relief [m]	Basin length [km]	Channel relief [m]	Channel length [km]	Channel slope [m/m]	Basin elongation ratio	Hypsometric integral	PCI
BioBio	8	24026.00	3511	288.48	1615	416.99	0.0039	0.61	0.23	0.13
Carampangue	6	1264.22	1333	53.29	1165	78.45	0.0148	0.75	0.31	0.11
Lebu	5	822.15	1334	50.09	872	83.46	0.0104	0.65	0.26	0.07
Cayucupil	6	703.72	1529	34.92	853	46.63	0.0183	0.86	0.34	0.10
Tavoleo	6	1272.00	1334	46.54	1188	71.14	0.0167	0.86	0.32	0.10
Tirúa	5	385.28	866	28.58	666	35.64	0.0187	0.78	0.45	0.08
Pellahuén	5	914.50	828	43.99	515	88.90	0.0058	0.78	0.48	0.06
Moncul	5	433.61	868	29.53	731	44.93	0.0163	0.80	0.30	0.07
Imperial	8	12333.00	3075	166.37	1572	252.59	0.0062	0.75	0.14	0.10
Toltén	6	9265.42	3729	157.69	1381	427.76	0.0032	0.69	0.17	0.09
Calle	6	11580.05	906	188.23	826	257.21	0.0032	0.65	0.21	0.17
Chaihuin	3	288.74	1044	28.00	777	48.83	0.0159	0.68	0.47	0.16
Bueno	6	9137.50	2403	142.71	175	193.47	0.0009	0.76	0.08	0.14
Pucatrihue	3	363.80	803	34.96	647	46.04	0.0141	0.62	0.35	0.08
Liesquehue	3	356.74	1009	32.97	799	48.31	0.0165	0.65	0.46	0.10
Cruces	3	188.28	974	23.32	820	30.97	0.0265	0.66	0.59	0.15
Lilco	4	1414.61	907	38.08	750	77.05	0.0097	1.11	0.25	0.05

Table 3.1: Basic morphometric data of the analyzed drainage basins and their trunk streams. The basins are ordered from north to south. Shaded cells mark the rivers that drain the low-relief Toltén segment.

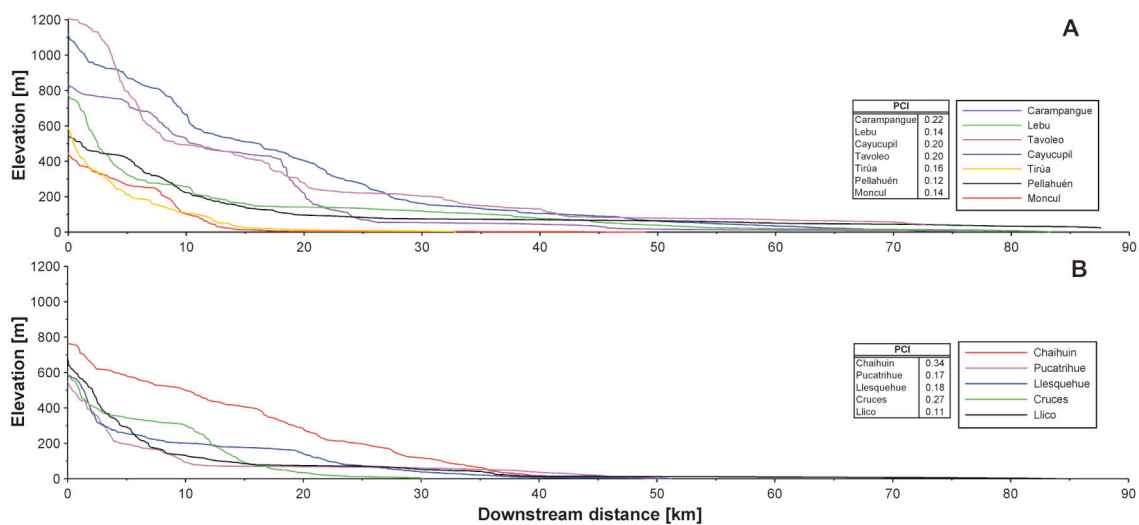


Fig. 3.4: River longitudinal profiles and profile concavity indices (PCI): (A) Nahuelbuta segment, (B) Bueno segment, documenting non-graded, partly convex channels with knickpoints and zero-slope-segments. Profiles are 15x exaggerated.

In the wind gap of the Río Pellahuén a silty alluvial plain covers the former, now completely dry river bed. Along the channel two separate terrace systems were distinguished: a lower, continuous terrace at 2 to 5 m above and parallel to the recent river bed, and a second, less well preserved upper terrace at about 10 to 90 m above the present channel (Fig. 3.6). Both terrace systems have distinct lithologic compositions. The lower terrace level consists exclusively of matrix supported, well rounded quartz and schist conglomerates. In contrast, the older upper terrace levels comprise matrix supported, very well rounded andesitic and basaltic conglomerates. The quartz and schist conglomerates are locally derived from basement rocks of the metamorphic Western Series. In contrast, the volcanic conglomerates are derived from the volcanic arc of the Main Cordillera. Alternatively, they could represent cannibalized deposits that were originally sourced in the volcanic Main Cordillera, but were temporarily stored in the Central Depression before they were remobilized. Pebble imbrication measurements from both terrace systems confirm the major drainage reorganization. The imbrication of the lower terrace deposits reflects the present southeast- to south-ward flow of the Río Pellahuén, whereas clasts from the upper terrace reflect a paleo-flow direction toward the northwest to north-northwest, indicating former drainage toward the Pacific (Fig. 3.6). The dichotomy in clast compositions and imbrications thus documents a complete drainage reversal in this area. This is further corroborated by bathymetric data revealing a large inactive submarine canyon and fan in front of the outlet of the paleo-Pellahuén river (Fig. 3.7).

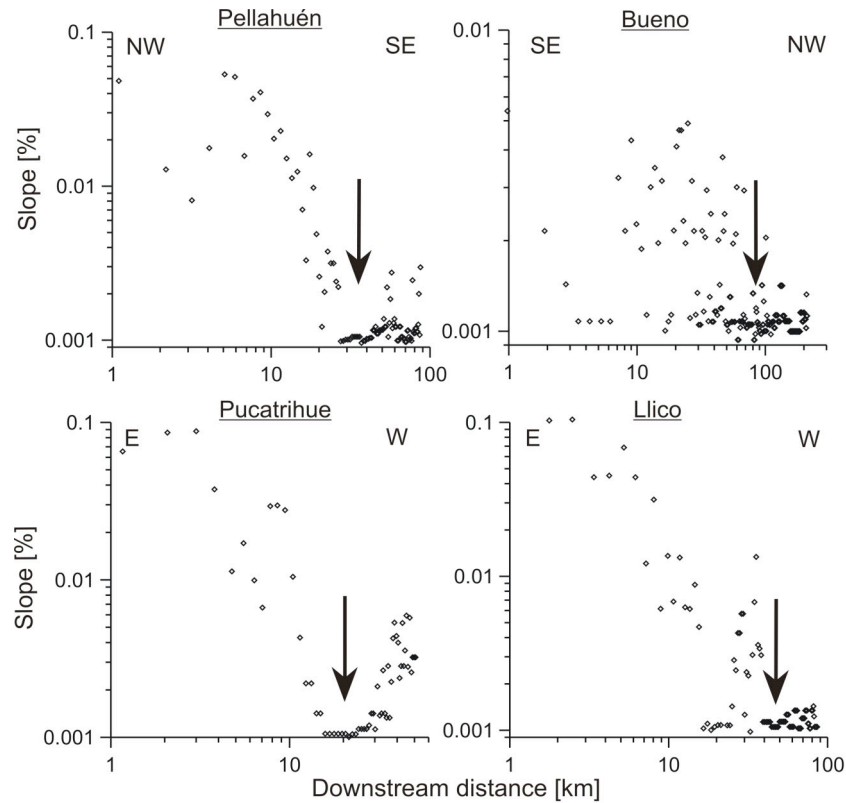


Fig. 3.5: DS plots of the streams traversing the Coastal Cordillera. Arrows mark the passage through the Coastal Cordillera. Note that all these rivers cross the range with a slope of virtually zero.

It is not known, however, when this drainage reversal occurred. Suárez and Empanan (1997) assign a Plio-Pleistocene age to volcanic conglomerates in the Central Depression that are identical in composition to the volcanic conglomerates constituting the upper terrace. In contrast, based on our field observations and regional geomorphic relationships, we infer the lower schist-bearing terrace levels to be of Holocene age. This inference is supported by the absence of colluvial deposits on this terrace, indicating that there has not been enough time for hillslope processes to generate such deposits. Since the reversal must have occurred between the formation of both terraces, the reversal should be a late Pleistocene/early Holocene event.

The Bueno segment is drained by five small local basins and the Río Bueno (Fig. 3.4). Similar to the Nahuelbuta segment, the stream networks indicate drainage disturbance, including river piracy and wind gaps. Two wind gaps are situated in the north near Río Chaihuín (Fig. 3.4). In addition, the valleys of the Bueno, Pucatrihue, Llesquehue and Llico rivers traversing the Coastal Range are characterized by virtually zero-degree slope segments (Fig. 3.5), similar to the Nahuelbuta segment. Interestingly, the Río Pucatrihue flows in an inadequately wide channel, which would have originally required much higher stream power to erode compared to the present-day small, and relatively low-relief contributing area (Fig. 3.4). This river must have lost a formerly large contributing area, similar to the Río Pellahuén in the Nahuelbuta segment. The Bueno, Llesquehue and Llico rivers also have very low stream power due to their low slope and/or small contributing areas. If this area is indeed continuously uplifting, it can be expected that their passages will be ultimately defeated. In summary, the drainage system of the Bueno segment shows the same characteristics of reorganization as the Nahuelbuta segment and thus emphasizes the fundamental influence of tectonic deformation on landscape evolution in this region.

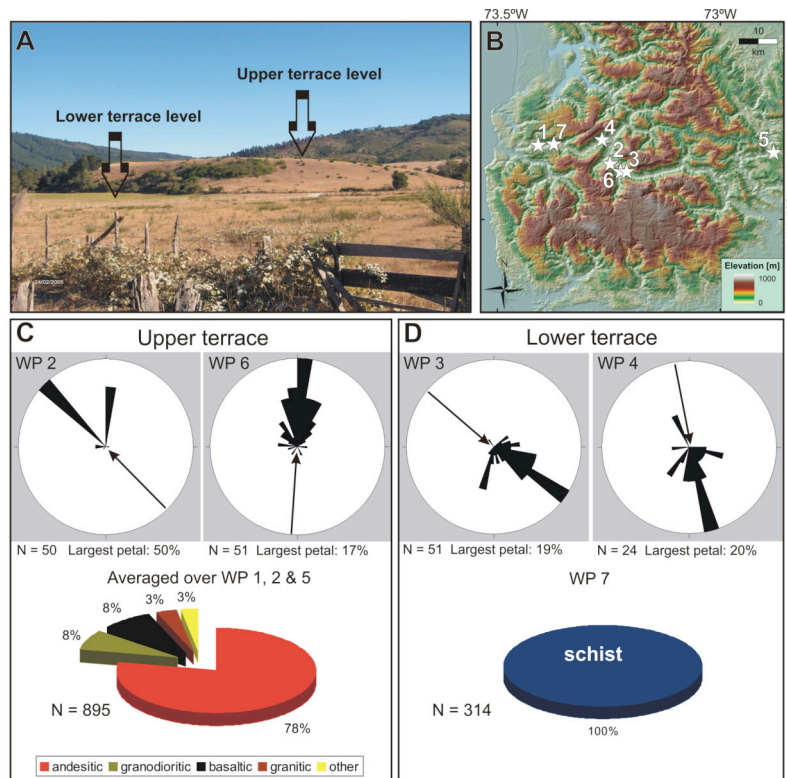


Fig. 3.6: Results of the pebble counts and flow directions measurements of alluvial terraces along the paleo-channel of the Pellahuén. (A): Photograph showing the well-preserved lower terrace ~ 5 m above river level, and a remnant of the upper terrace ~ 30 m above river level. (B): DEM denoting sampling locations. (C): Paleo-flow directions and pebble counting results of the upper terraces. WP-numbers are marked in B. Note the paleo-flow towards north-northwest, north, and the polymict terrace composition of the conglomerates. (D): Paleo-flow directions and pebble counting results of the lower terraces. WP-numbers are marked in B. Note here the opposite flow direction towards east-southeast, south, and the monomict terrace composition of the conglomerates.

Conversely, in the Toltén segment the river network is very different. The entire segment is drained by three large, well integrated basins that define the Imperial, Toltén and Calle drainages (Fig. 3.4). These basins are dominated by swamps, extensive alluvial plains and low-slope, near sea-level drainage. Evidence for incision is absent. In contrast to the other segments, these drainage systems show no signs of reorganization or modifications, and appear to be stable.

### 3.4.2 Geological and geophysical data

The subducting and overriding plates are both fragmented by inherited structural features. For example, the Bío-Bío, Lanalhue, and Mocha-Villarica fault zones are dominant, reactivated Paleozoic structures in the overriding plate (Fig. 3.1). Interestingly, the Bío-Bío Fault in the north and the Mocha-Villarica fault zone in the south broadly correspond to our morphologically defined borders of the Nahuelbuta segment. However, the other segment boundaries do not coincide with upper plate structures. Lithology and structure of the Toltén segment significantly differ from the other two segments since the Central Depression and its characteristic Tertiary-Quaternary sediment infill, common features along most of the Chilean margin, are

absent, and the basement of the Coastal Cordillera reaches into the Main Cordillera (Fig. 3.1).

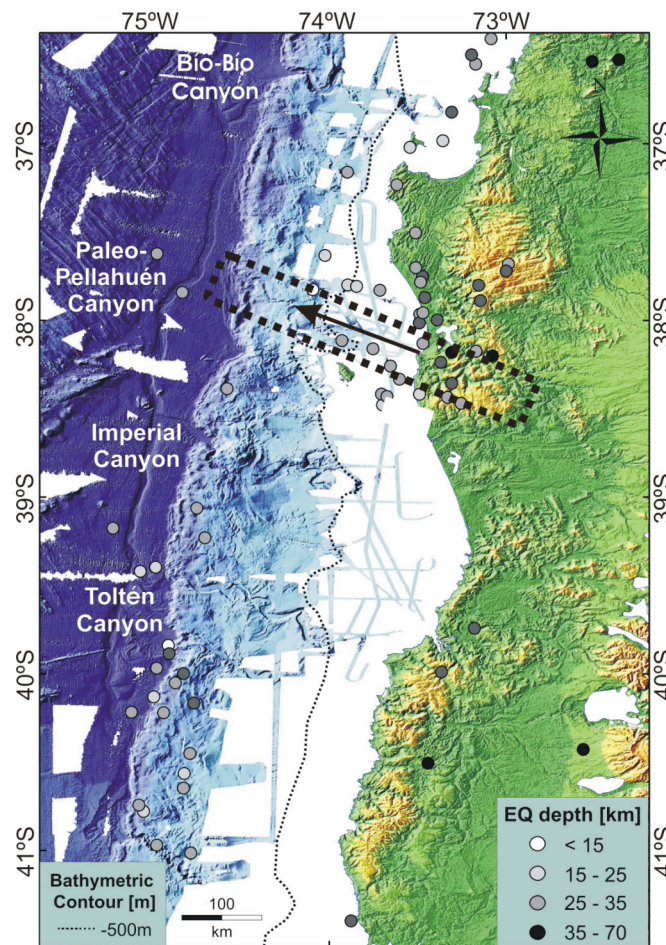


Fig. 3.7: Bathymetric map (modified after Bangs and Cande (1997)), and earthquake distribution of events with  $M_w > 5$ , derived from Engdahl et al. (1998) and the Global NEIC-Catalog, 1973 to present (2006). Note the concentration of shallow earthquakes (5-35 km) beneath the Nahuelbuta segment, and the trenchward shift of earthquake loci at 38°30'S. Note also the sparsity of large seismic events beneath the Toltén and Bueno segments. The stippled black rectangle denotes the paleo-canyon that can be attributed to the former paleo-Pellahuén river when it was still supplied by a large Andean catchment.

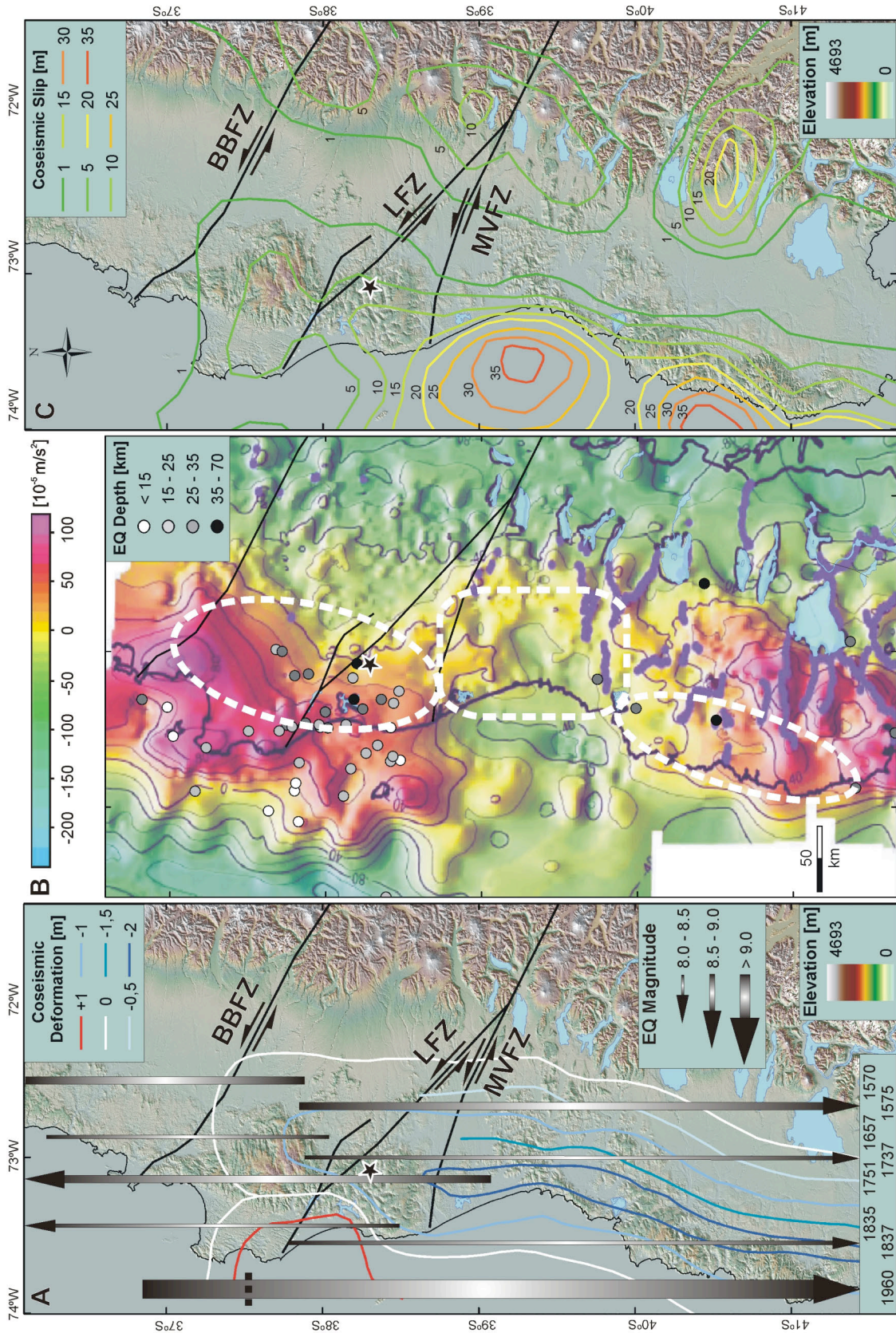
The incoming Nazca plate is segmented by three major transform fracture zones (FZ) separating oceanic crust of different age: the Mocha FZ, currently subducting beneath the Arauco Peninsula and the Cordillera de Nahuelbuta, the Valdivia FZ system, and the Chiloe FZ (Fig. 3.1). Interestingly, the distribution of offshore forearc basins that are bordered by these oceanic fracture zones correlates with our morphotectonic segmentation as well. According to ocean floor age and origin, as well as subduction geometry, the Valdivia FZ system is expected to have the strongest potential to influence the subduction process and the related long-term morphotectonic forearc evolution. First, the Mocha and Chiloe FZ subduct obliquely, resulting in fast southward migration of about  $40 \text{ m a}^{-1}$  along the margin (Vieter et al., 2005). Therefore, if ocean-floor topography and upper plate deformation and uplift are coupled, their impact should be time-transgressive. In contrast, the Valdivia FZ system remains perpendicular to the trench, and its impact, if present, must have been relatively steady over longer timescales. Second, the Valdivia FZ system separates not only oceanic crust of very different age but also of completely different origin. In fact, the extensive Valdivia FZ system broadly coincides with the Toltén segment, where the coast is significantly bent inland, a phenomenon remarkably similar to the intercept between the

Juán Fernandez Ridge and the upper plate farther north, and where topography is also different compared to adjacent sectors.

The regional earthquake distribution along the segments along the margin corroborates our assessment that the northern fracture zone systems constitute important transitions in the subducting plate. The most striking pattern in the total regional seismicity distribution is a complete westward shift in the locations of earthquakes larger than  $M_w > 5$  toward the trench at 38°S (Fig. 3.7). This coincides with the locus of subduction of the Valdivia FZ system. Thus, the earthquake distribution reflects the major changes in slab properties, such as thermal structure, buoyancy and elastic strain accumulation due to decreasing ocean-floor age (Oleskevich et al., 1999). Before shifting to the trench, shallow earthquakes (< 30 km) cluster in the upper plate beneath the Nahuelbuta segment. Their spatial distribution mirrors the position of thrust faults (Bohm et al., 2002), documenting ongoing thrusting and uplift in this segment. Beneath the Toltén segment few earthquakes can be traced, whereas in the Bueno segment large earthquakes appear to be absent. Furthermore, the coseismic forearc deformation associated with large earthquakes also varies considerably along the coast. In the Nahuelbuta segment coseismic uplift is documented (Kaizuka et al., 1973; Nelson and Manley, 1992), whereas the Toltén segment records coseismic subsidence (Barrientos and Ward, 1990; Cisternas et al., 2005).

Finally, the nature of gravity anomalies in the forearc region coincides with our geomorphic segment boundaries. Gravimetry (Tašárová, 2004) shows that the margin of southern Chile can be differentiated into three gravimetric provinces (Fig. 3.8). Whereas the Nahuelbuta and Bueno segments are both characterized by positive gravity anomalies, the Toltén segment coincides with a pronounced negative gravity anomaly.

*Fig. 3.8 (overleaf): (A) DEM with major upper-plate structures and coseismic deformation during the 1960 earthquake (modified after Plafker and Savage (1970)). Large historic earthquake-rupture zones with  $M_w > 7$  are superposed on the DEM (compiled after Lomnitz (1970), Kelleher (1972), Cifuentes (1989), Beck et al. (1998), Campos et al. (2002), Lomnitz (2004), and Cisternas et al. (2005)). Arrows mark rupture continuation. Note that morphotectonic units and rupture zones do not coincide. In fact, rupture zones always occupy areas of different morphology. The star denotes the epicenter of the 1960 earthquake. The dashed line crossing the 1960 rupture zone separates the main shock (south) from the foreshock (north). (B) Morphotectonic segments (white-dashed ellipsoids), major upper-plate structures and earthquake distribution ( $M_w > 5$ , derived from teleseismic earthquake relocation (Engdahl et al., 1998)), superposed on Bouguer anomalies [ $10^{-5} \text{ m s}^{-2}$ ] (modified after Tašárová (2004)). Note the correlation of morphotectonic segments with seismicity clusters, major upper-plate fault zones (BBFZ, MVFZ), and gravity anomalies. (C) DEM with major upper-plate structures, and coseismic slip during the 1960 earthquake (modified after Barrientos and Ward (1990)). Note the correlation of slip maxima and morphotectonic segments.*



For figure caption see previous page.

### 3.5 Discussion

Our investigations document a pronounced morphologic segmentation of the Chilean forearc between 37° and 41°S into three distinct domains. These domains constitute geomorphic entities with characteristic topography, drainage networks, and common geomorphic processes that shape these regions. Moreover, geophysical data, including remarkable gradients of earthquake distribution and gravity anomalies, correspond with these morphotectonic segments.

Maps of local relief reveal highly dynamic fluvial systems with high-relief/high-incision sectors that indicate ongoing uplift in the Nahuelbuta and Bueno segments. Both border the low-relief central Toltén segment, which does not show signs of recent river modifications and lacks significant topography and active incision. Additionally, in this segment the Central Depression and a Cenozoic sediment cover are missing as exclusively basement rocks are exposed.

Interestingly, a grid-iron fluvial pattern similar to the one found in the three segments was also described in the Himalayan foreland undergoing active folding (Gupta, 1997). There, originally transverse rivers were deflected by lateral and vertical growth of anticlines that are associated with active blind faults. These rivers exit through low-relief sectors between anticlines, but integrate large drainage-basin areas upstream due to stream diversion, rerouting and piracy. The evolution of the Chilean segments is remarkably similar. Flow reversals, abandoned marine canyons, stream captures, and low-relief outlets document that rivers are gradually deviated by the progressively uplifting Coastal Cordillera. This forces drainage to migrate laterally toward the tips of the uplift or to a confluence with transverse rivers already located there. The result is the characteristic drainage pattern with widely spaced point-source drainage outlets at the mountain front that are pinned to the tips of the mountain range in the low-elevation sectors (Fig. 3.9). The diversion of streams and the low stream power of the traversing rivers should have seriously modified the sediment supply to the Pacific ocean during the late Pleistocene and Holocene. Moreover, we expect this process to have been amplified during the last deglaciation and related exposure of the terminal lakes near the Andean mountain front, which acted as effective sediment traps. Importantly, the tectonic defeat of the river documents that the amplitude and rate of tectonic deformation in this region are high enough to outpace fluvial incision. The defeat might have been facilitated by rearrangements of the Andean contribution area that decreased the incision power of the river and thus amplified the effect of tectonics.

The central sectors of the Nahuelbuta and Bueno segments exhibit the highest variability and are divided by deeply incised, approximately east-west trending valleys. The loci of valley incision approximately coincide with the best-fit curve maxima encompassing the ellipsoid-shaped uplift zones (Fig. 3.3). This setting is reminiscent of the actively deforming Oxaya Anticline in northern Chile, where rivers have been cutting through the central part of an uplifting antiform (Zeilinger et al., 2005). There, stream piracy and wind gaps indicate migration of drainages away from crestal regions. Indeed, in the Nahuelbuta and Bueno segments the ellipsoidal shape, the tilted geomorphic surfaces, the grid-iron drainage evolution, and high central sections incised by rivers along the short axis of the uplift, emphasize that these segments are large, actively deforming crustal-scale antiformal structures.

The ultimate cause for the observed forearc segmentation is not known. Either inherited upper plate structures, characteristics of the oceanic plate or differential accretionary processes at the plate interface might influence the spatiotemporal distribution of deformation, and thereby, control the topographic evolution of the forearc. Our datasets suggest that a complex combination of factors is responsible for

the highly differential morphotectonic evolution of the Chilean margin between 37° and 41°S. The two major upper-plate structures, the Bío-Bío fault zone in the north and the Mocha-Villarica fault zone in the south (Echtler et al., 2003), coincide with the geomorphic boundaries of the Nahuelbuta segment (Fig. 3.8), but such structures are not documented in the other segments, suggesting that the segmentation may not simply be controlled by upper-plate structures alone.

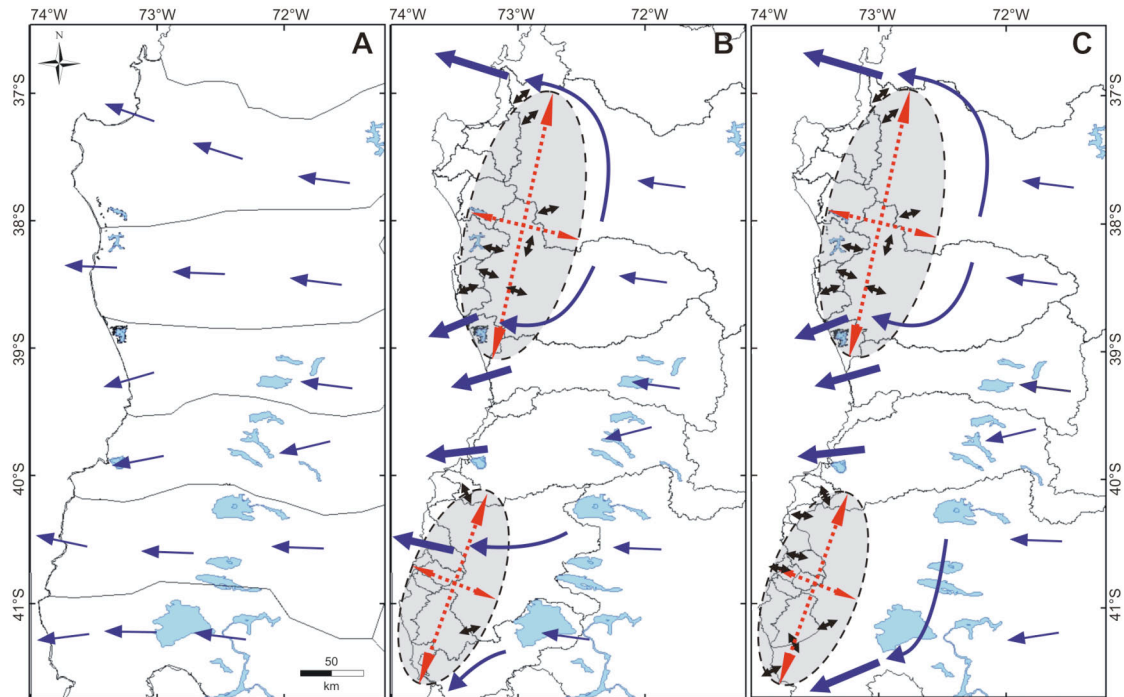


*Fig. 3.9: Evolution model of the south-central Chilean forearc. Black double-arrows mark wind gaps with flow reversals, simple blue arrows mark the regional discharge path. Uplifting antiformal structures are marked by grey-shaded ellipses with red arrows depicting the uplift axes. (A): Inferred equilibrium drainage pattern prior to the uplift of the Coastal Range. (B): Present drainage pattern, concentration of basin outlets in the middle, low-relief segment. Drainage reversal in the northern segment causes discharge rerouting towards the north and south. (C): Hypothetical future drainage pattern with scarce outlets. All rivers are forced to bypass the Coastal Ranges and pinned to the tips of the uplifting antiforms.*

The Valdivia FZ system, subducting beneath the Toltén segment, delimits a major change in ocean floor age and origin. The southward younging of the oceanic crust and the related differences in buoyancy, fluid content and thermal gradient are expected to influence the coupling at the plate interface and the thermal structure of the upper plate (Oleskevich et al., 1999; Lagabrielle et al., 2000; Heintz et al., 2005). Increased heat-flow in the upper plate induced by the warmer slab may increase the ability of the crust to store elastic strain. The southward-younging slab could thus control the deformation style of the forearc. In fact, the distribution of earthquake locations corroborates these assessments. We observe a clustering of shallow thrust-related active seismicity in the upper plate of the Nahuelbuta segment where older, colder ocean floor is subducted (Fig. 3.7). This documents that in this forearc segment the convergence is accommodated by discrete fault displacement via internal deformation of the forearc (Melnick and Echtler, 2006a). However, the resulting long-term uplift may eventually be related to progressive underplating of trench sediments as proposed by Lohrmann (2002). Interestingly, the locus of the Quaternary deformation as recorded by tilted marine terraces (Kaizuka et al., 1973) spatially coincides with the ongoing subduction of the oceanic Mocha fracture zone beneath the Nahuelbuta segment as well. Therefore, the subduction of the Mocha FZ might be another factor contributing to the Quaternary uplift of the Nahuelbuta crustal antiform. South of the Nahuelbuta seismicity cluster and the Valdivia FZ system, where younger and warmer oceanic crust is

subducted, no pronounced fault activity has been recorded. Thus, the convergence might be partly accommodated by a rather flexible response of the upper plate. Based on our results we infer that progressive buckling of the crust occurs in the Bueno segment, leading to a crustal-scale flexure with a wavelength of ca. 170 km. Consequently, the segmentation of the oceanic plate appears to have a severe impact on the style of onshore deformation, and thus ultimately on landscape evolution.

In contrast to the other segments, the Toltén segment correlates with a significant absence of a negative gravimetric anomaly. Forward modelling of this anomaly indicates that it is controlled by a sector of the oceanic slab, which appears to be located deeper beneath this segment (Tašárová, 2004). Hackney et al. (2006) explain the deeper slab position by a locally thickened forearc crust. Therefore, plate coupling appears to be stronger than in the adjacent sectors with positive anomalies. It is conceivable that the stronger coupling could prevent extensive basal accretion and uplift in the Toltén segment, which would keep this sector in a quasi-stable position. The average topography of the Toltén segment with only 60 m and the stable drainage pattern support this scenario. Nevertheless, the segment might still undergo minor uplift as indicated by the exhumation of Coastal Cordilleran basement in this sector. Our drainage-evolution model though shows that the rapid uplift of the Nahuelbuta and Bueno segments concentrates all discharge, and hence stream power, in the Toltén segment. Fluvial erosion could thus outbalance the effects of minor uplift. Observed coseismic subsidence in this segment (Barrientos and Ward, 1990; Cisternas et al., 2005) could also be attributed to strong plate coupling. However, the exposure of basement rocks and the absence of thick sedimentary sequences in the Central Depression that would be expected if this area were subsiding, exclude significant long-term subsidence of this segment. These observations suggest long-term geomorphic stability and steady-state behavior.

Our results portend that the segmentation of the Chilean forearc is determined by a combination of the physical properties of the incoming plate, and the focusing through inherited upper plate structures. This segmentation appears to be a long-term feature of the forearc-evolution that persists on timescales of  $10^5$  to  $10^6$  years. In this context, it is interesting to investigate whether earthquake rupture zones also correspond to these segments or if they are independent. Therefore, we compare rupture segments of large historic earthquakes compiled by Lomnitz (1970, 2004), Kelleher (1972) and Beck (1998) with our morphotectonic segmentation (Fig. 3.8). Earthquakes in 1570, 1657, 1751 and 1835 ruptured the Nahuelbuta segment. Earthquakes in 1939 and 1953 terminated at the northern part of the Nahuelbuta segment. Conversely, large earthquakes in 1575, 1737, 1837 and 1960 produced extensive ruptures that developed irrespective of segment boundaries. This suggests that morphotectonic segments can influence earthquake rupture, yet, there might be a seismic energy threshold above which segments fail irrespective of morphotectonic or structural boundaries. Therefore, earthquake-rupture segments are rather transient phenomena, whereas the identified morphotectonic domains are sustained on much longer timescales. Notwithstanding, a closer inspection of the well-studied 1960-earthquake reveals that although this megathrust earthquake ruptured throughout all segment boundaries, the coseismic slip was non-uniformly distributed. For example, the zones of greatest coseismic slip were centered beneath the Valdivia, Pucatrihue and Chiloé offshore basins documenting an inhomogeneous rupture process (Barrientos and Ward, 1990; Wells and Blakely, 2003). Intriguingly, these coseismic slip sectors and the offshore basins also coincide with the onshore morphotectonic segments. This suggests that there might be not only a relationship between earthquake rupture and forearc basins as shown by Wells and Blakely (2003), and a relationship between earthquake rupture and gravity anomalies as proposed by Song and Simons (2003), but also a link between earthquake rupture, offshore basin formation, gravity anomalies, and onshore morphotectonic segmentation. This

hypothesis needs further exploration and testing in other active forearc regions, and could be another step on the way to a better understanding of the relations between subduction processes and landscape response.

### 3.6 Conclusions

In this paper, we investigated the forearc of the southern Chilean active convergent margin in that area of the rupture zone of the Chilean megathrust earthquake of 1960. We combined remote sensing, geomorphologic, sedimentologic and geophysical data to develop a model of dynamic forearc evolution for south-central Chile, and discuss its controlling parameters.

We document that the forearc is morphotectonically divided into three segments, the Nahuelbuta, Toltén, and Bueno segments that exhibit a grid-iron drainage pattern. The Nahuelbuta and Bueno regions are characterized by highly dynamic catchments, rerouting of sediments, and a migration of watersheds indicating ongoing Quaternary uplift. Conversely, the Toltén segment appears to be stable and in long-term steady-state. This shows that these segments are affected by different modes of deformation. Apparently, the three morphotectonic segments have been persistent over long timescales, whereas earthquake rupture zones are transient and quite variable on short timescales and my often rupture across morphotectonic boundaries.

Our data suggests that the highly diverse landscape evolution of the forearc in south-central Chile is controlled by the physical properties of the subducting plate as well as forearc rheology, and focused by inherited structures in the upper plate. Hence, landscape evolution in forearc regions does not form a uniform principle, but rather reveals a complex interplay between subduction processes, inherited structures, and highly differentiated surface response.

### Acknowledgements

This work was funded by Deutsche Forschungsgemeinschaft through the Leibniz Award to Manfred Strecker (STR373-18-1), the A. Cox fund of Stanford University, and supported by the GeoForschungsZentrum Potsdam as well as the DAAD, the German Academic Exchange Program, to Katrin Rehak. We appreciate discussions with George Hilley.

## 4. Reconstructing surface uplift using cosmogenic nuclides, the Coastal Cordillera in south-central Chile

### Abstract

*Although segmented forearcs are very sensitive to subduction-system changes and therefore effective recorders of subduction processes, the relationship between subduction and surface processes remain uncertain due to difficulties in quantifying forearc uplift and changes in the subduction mode. Specifically, it is not yet understood how persistent morphotectonic forearc segments are, despite the fact that they are common features along many subduction margins.*

*The Coastal Cordillera of south-central Chile provides a range of evidence of subduction-system behavior through constraints on uplift provided by flights of marine terraces, displaced erosion surfaces, emerged strandlines, and pronounced drainage-system perturbations. Dating of low-relief surfaces originally graded to sea level from concentrations of in-situ produced cosmogenic  $^{10}\text{Be}$  and  $^{26}\text{Al}$  indicate that there was active uplift from 4.8 to 2.6 Ma ago at a mean rate of  $0.21 \text{ mm a}^{-1}$ , a value which is similar to long-term denudation rates based on thermochronology and estimates of offshore uplift from the region. The initiation of uplift is related to a switch from erosive to accretive subduction  $\sim 5 \text{ Ma}$  ago which has been attributed to an increase in sediment thickness in the adjacent trench in response to the onset of glaciation in the region. This interpretation implies that forearc uplift is controlled by enhanced basal accretion of sediments. The relation between global cooling, change in subduction mode, and forearc uplift indicates that uplift of the Coastal Cordillera along the south-central Chile margin is a consequence of climate change.*

*Ultimately, the present-day forearc segmentation has been established in Pliocene suggesting that morphotectonic segments can be persistent over millions of years and are independent of short-term earthquake-rupture segments.*

**KEYWORDS:** *cosmogenic nuclides, surface uplift, forearc, Chile, subduction, segmentation, geomorphology*

### 4.1 Introduction

Forearc regions are among the most tectonically active environments worldwide, often being characterized by rapid and pronounced uplift and subsidence in response to accretive or erosive subduction modes (e.g. Muhs et al., 1990; Pazzaglia and Brandon, 2001; Clift et al., 2003; Marquardt et al., 2004; Molin et al., 2004). The record of surface-uplift and subsidence and the associated response of the onshore landscape system in such regions may thus furnish important insights into the factors that govern the geodynamic and structural evolution of these dynamic tectonic settings. Moreover, about 50% of the total length of global coastlines are located in active tectonic regions, in many instances in association with significant concentrations of population and

economic activity, and forearcs are consequently a research priority for tectonic, tectono-geomorphic, and seismic hazard studies (e.g. Mogi, 1969; Plafker and Savage, 1970; Kelleher, 1972; Sykes and Nishenko, 1984).

Patterns of forearc deformation can vary significantly along plate boundaries, typically resulting in the formation of different morphotectonic segments (Wells et al., 1988; Ryan and Scholl, 1993; Gutscher et al., 1999; Rehak et al., 2008). Deformation and landscape development in these segments is controlled by a variety of factors comprising bathymetric heights on the subducting plate (e.g. McCann and Habermann, 1989; Hsu, 1992; Mann et al., 1998; Gardner et al., 2001; Laursen et al., 2002; Taylor et al., 2005), inherited, reactivated structures of the upper plate (Echtler et al., 2003; Rosenau et al., 2006), and the mode of subduction (Lamb and Davis, 2003; Clift and Vannucchi, 2004). The latter may alter over time in response to changes in subducting-plate buoyancy, plate-convergence rate, and trench-fill thickness (von Huene and Scholl, 1991; Lallemand et al., 1994; Bangs and Cande, 1997; Lamb and Davis, 2003; Clift and Vannucchi, 2004; Melnick and Echtler, 2006a).

The mode of subduction is a crucial part of the subduction process since it influences the entire deformation and magmatic system of the upper plate, which in turn may determine the lifetime of morpho- and seismotectonic segments. Nevertheless, in many cases it is still not clear when changes in subduction mode occurred, how deformation in the forearc was affected by such changes, and whether these new conditions determine the spacing and internal development of forearc segments. One way to elucidate these questions is to quantify the uplift and geomorphic history of the forearc in a geodynamic setting where a relatively recent switch in subduction mode has occurred. However, this approach is often hampered by the problem of unambiguously determining the onset of such changes and the resulting uplift history due to the lack of suitable materials for dating. Nevertheless, cosmogenic-nuclide dating of geomorphic surfaces, which has been increasingly applied over the last 15 years (e.g. Bierman, 1994; Cerling and Craig, 1994; Gosse and Phillips, 2001; Niedermann, 2002), has proved a useful tool in reconstructing landscape development (e.g. Dunai et al., 2005; Nishiizumi et al., 2005; Fabel et al., 2006), and clearly has potential in addressing outstanding questions of forearc behavior.

Here, we use measurements of cosmogenic  $^{10}\text{Be}$  and  $^{26}\text{Al}$  on in-situ quartz clasts in the Coastal Cordillera of south-central Chile to date a paleo-surface in order to infer the recent uplift history of this forearc region. The paleo-surface is a well-preserved low-relief upland at about 750 m that appears to be a remnant of a formerly continuous regional erosion surface. This field area was selected because of its sustained tectonic activity during the Cenozoic, a relatively well dated young change in subduction regime, elevated paleo-surfaces formerly located at, or near, sea level, and pronounced surface ruptures as well as vertical movements during large earthquakes.

This region constitutes an exceptional active margin, stationary since Paleozoic (Glodny et al., 2005), and has experienced a change from subduction erosion to subduction accretion in late Miocene to early Pliocene time (Bangs and Cande, 1997; Melnick and Echtler, 2006a). This forearc is also characterized by different seismotectonic and geomorphic segments, documenting a distinct spatio-temporal tectonic development (Hackney et al., 2006; Rehak et al., 2008). For example, the northern Nahuelbuta segment represents the highest sector of the Coastal Cordillera and has been subjected to uplift during the Quaternary (Kaizuka et al., 1973; Nelson and Manley, 1992; Mardones and Reuther, 1999; Bookhagen et al., 2006a; Melnick et al., 2006; Melnick and Echtler, 2006a; Rehak et al., 2008). However, it is not known when surface uplift in the Coastal Cordillera began and therefore how rapidly the range has developed, even though this information is crucial in assessing whether the onset of uplift is coupled with the shift in subduction mode and deciphering the temporal evolution of the present morphotectonic segmentation. Furthermore, data on the

geometry and onset of uplift and the long-term development of morphologically distinct forearc sectors would assist in the differentiation of landscape behavior influenced by tectonic movements on short time scales, such as through several seismic cycles, and on longer time scales of the order of  $10^5$  to  $10^6$  years.

## 4.2 Regional setting

The Nahuelbuta segment study area in the Coastal Cordillera (Fig. 4.1) forms a part of the southern Andean accretionary margin (Bangs and Cande, 1997; Melnick and Echtler, 2006a). This plate boundary is characterized by the oblique ( $N77^\circ E$ ) subduction of the oceanic Nazca plate beneath the South American continent at a rate of approximately  $65$  to  $85$   $\text{mm a}^{-1}$  (Demets et al., 1994; Somoza, 1998; Angermann et al., 1999). The forearc in this region comprises three morphotectonic segments, each of which has experienced a distinct tectono-geomorphic evolution (Rehak et al., 2008). Two high-relief/high-incision sectors, the Nahuelbuta and Bueno segments, with highly dynamic fluvial systems reflecting continuing active uplift resulting in tectonically induced stream captures, flow reversals, and deep incision, border the low-relief central Toltén segment. The Toltén segment lacks both significant topographic contrasts as well as active incision, suggesting long-term geomorphic stability (Fig. 4.1) (Rehak et al., 2008). Here, we focus on the southern part of the actively uplifting Nahuelbuta segment of the Coastal Cordillera between  $38^\circ$  and  $38.5^\circ S$  (Fig. 4.1) (Kaizuka et al., 1973; Rehak et al., 2008).

The Coastal Cordillera around  $38^\circ S$  comprises a Paleozoic-Triassic forearc complex, including rocks related to a Permo-Triassic accretionary wedge and parts of a Permo-Carboniferous magmatic arc that are grouped into an Eastern and a Western Series (Fig. 4.1) (e.g. Hervé, 1977; Glodny et al., 2005; Glodny et al., in press). The Eastern Series of the Cordillera de Nahuelbuta is dominated by high-temperature metamorphic rocks and a Carboniferous granitic batholith. In the study area the basement rocks are dominated by high-pressure schists, metabasites, and accreted metacherts of the Western Series (Aguirre Le-Bert et al., 1972; Hervé, 1977) and these lithologies provide excellent sources of quartz for cosmogenic nuclide dating. The mountain range is characterized by numerous reactivated north-northeast, west, and northwest -striking Paleozoic faults with strike-slip kinematics (Mordojovich, 1981; Echtler et al., 2003; Rosenau, 2004). The most prominent structures are the Bío-Bío, the Lanalhue (Glodny et al., in press), and the Mocha-Villarica fault zones (Melnick and Echtler, 2006b) (Fig. 4.1).

The Coastal Cordillera reaches elevations of  $1600$  m and is characterized by flights of tilted marine terraces and remnants of marine/fluvial erosion surfaces, reaching elevations of up to  $900$  m. The staircase morphology of these surfaces documents protracted deformation and uplift of this forearc segment. Continuing river incision, tectonically induced stream piracy and the existence of seismogenic faults support the notion that this mountain range is tectonically active (Haberland et al., 2006; Rehak et al., 2008). Terrace levels at elevations of up to  $500$  m are covered by marine Tertiary sediments indicating marine erosion and uplift superposed on oscillating sea levels since the late Pliocene (Plafker and Savage, 1970; Kaizuka et al., 1973; Nelson and Manley, 1992; Kelm et al., 1994; Mardones and Reuther, 1999; Melnick and Echtler, 2006a). In contrast, low-relief surfaces reaching elevations between  $500$  m and  $900$  m lack any evidence of a former marine sedimentary cover and may be of fluvial origin or, alternatively, may constitute uplifted marine abrasion

platforms whose thin veneer of marine sediments has been removed (Kaizuka et al., 1973).

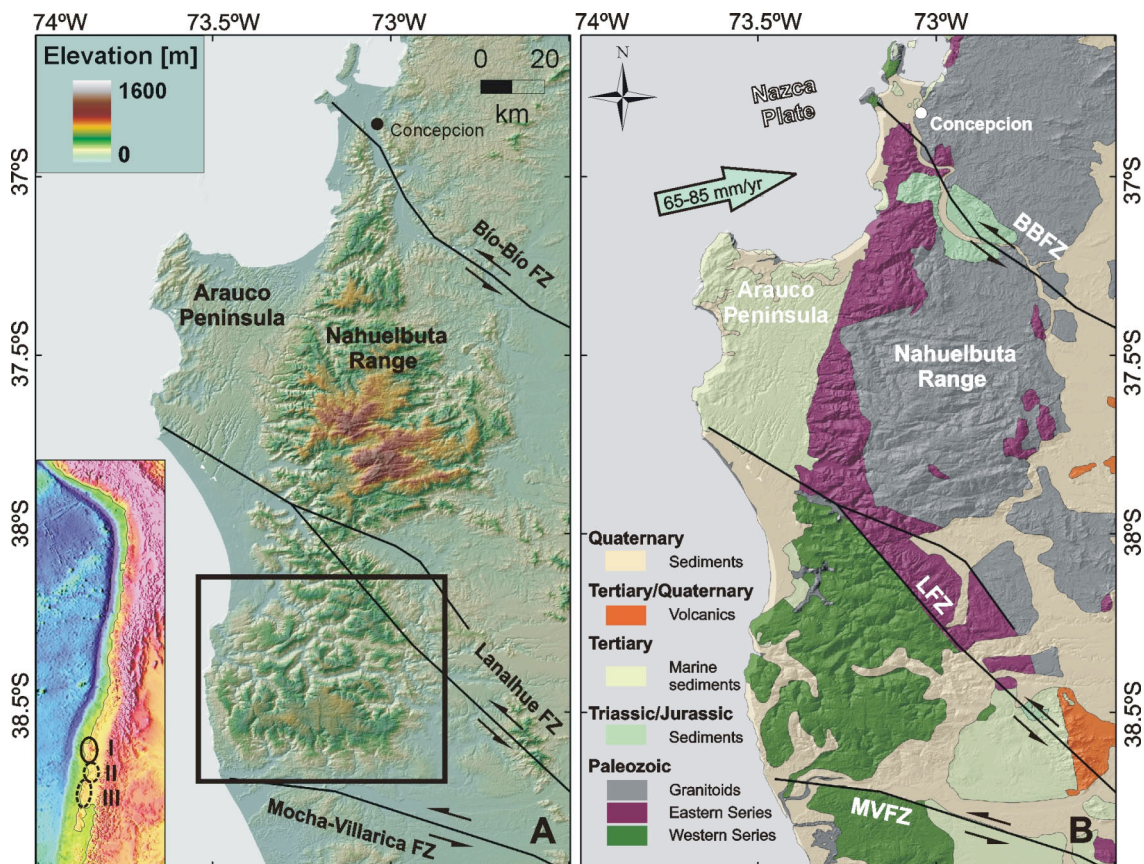


Fig. 4.1: Regional setting of the south-central Chile forearc. (A): DEM with major fault zones. The inset marks the morphotectonic forearc segments (I – Nahuelbuta segment, II – Toltén segment, III – Bueno segment after Rehak (2008)). Here, we focus on the northern Nahuelbuta segment. The black box delineates the working area. (B): Geological map of the forearc. The study area is lithologically homogeneous and comprises high-pressure schists from the Paleozoic Western Series.

Offshore forearc basins in this region have been inverted since 4.4 Ma, after an earlier phase of protracted extension and subsidence (Mordojevich, 1981; Melnick and Echtler, 2006a; Finger et al., 2007). Long-term denudation rates derived from apatite fission-track thermochronology for rock samples collected in the Coastal Cordillera average  $0.04 \text{ mm a}^{-1}$  for the last 70 Ma. However, the dataset has a clear inflection point at 5 Ma, which marks the onset of accelerated denudation at rates of  $0.20 \text{ mm a}^{-1}$  (Glodny et al., 2007).

### 4.3 Methodology

In-situ produced cosmogenic nuclides provide the unique possibility to constrain surface-exposure ages on intermediate timescales of  $10^5$  to  $10^6$  years (e.g. Nishiizumi et al., 1991; Cerling and Craig, 1994; Repka et al., 1997; Fabel and Harbor, 1999; Granger and Muzikar, 2001; Bierman et al., 2002; Bookhagen et al., 2006b). The underlying principle is the accumulation of cosmogenic nuclides in the rock due to the bombardment of the earth's surface with secondary cosmic rays (Lal and Peters, 1967). When the production rate of the nuclide and its concentration within the rock are

known, the time of surface exposure can be calculated if subsequent erosion has been negligible or can be independently constrained (Gosse and Phillips, 2001; Niedermann, 2002). Additionally, cosmogenic nuclide concentrations can also be measured in soil profiles (e.g. Brown et al., 1988; Monaghan et al., 1992; McKean et al., 1993; Heimsath et al., 1997; Riebe et al., 2001).

Here, we use cosmogenic  $^{10}\text{Be}$  and  $^{26}\text{Al}$  to unravel the initiation of uplift of a mountain range by dating an uplifted low-relief upland. First, we conducted a detailed morphometric analysis of the Coastal Cordillera identifying several low-relief surfaces and sampling targets. Subsequently, the surfaces were inspected in the field. The sampling sites constitute planar, slightly tilted geomorphic surface with a slope  $< 4^\circ$ . For our study, we selected the best-preserved, uppermost flat surface at an elevation of 700 to 800 m  $\sim 38.5^\circ\text{S}$  on top of the range consisting of exposed basement schist and regolith (Fig. 4.2). Localized erosion and incision are absent except around the outer surface edges where a pronounced break in slope delineates the limit of dissection by headward-eroding valleys. The bedrock is mantled by regolith, which slowly grades from weathered basement to a clay-rich soil horizon constituting an in-situ weathering profile (Fig. 4.3). All samples were collected in a nature reserve where the primary vegetation is preserved excluding human influences. We sampled profiles along road cuts and excavated trenches. All quartz clasts in the profiles were highly angular with no signs of transport. About 80 individual clasts per sample were collected, with a long-axis diameter of 1 to 2 cm. The samples were crushed and sieved to a grain size of 125 to 500  $\mu\text{m}$  and processed for cosmogenic  $^{10}\text{Be}$  and  $^{26}\text{Al}$  analysis using standard techniques (e.g. Kohl and Nishiizumi, 1992; Bierman et al., 2002). In preparation for Accelerator Mass Spectrometry (AMS) the samples were mixed with Nb and Ag, respectively, and measured at the AMS Laboratory at the Scottish Universities Environmental Research Centre (SUERC). Beryllium measurements were normalized to the NIST SRM 4325 standard with an assumed  $^{10}\text{Be}/^9\text{Be}$  ratio of  $3.06 \cdot 10^{-11}$ . Aluminium isotope ratios were normalized to the Z92-0222 standard with an assumed  $^{26}\text{Al}/^{27}\text{Al}$  value of  $4.11 \cdot 10^{-11}$ . Measurement errors are below 3%. We assumed an additional analytical error of 2% for the  $^9\text{Be}$ -carrier and  $^{27}\text{Al}$ -carrier.

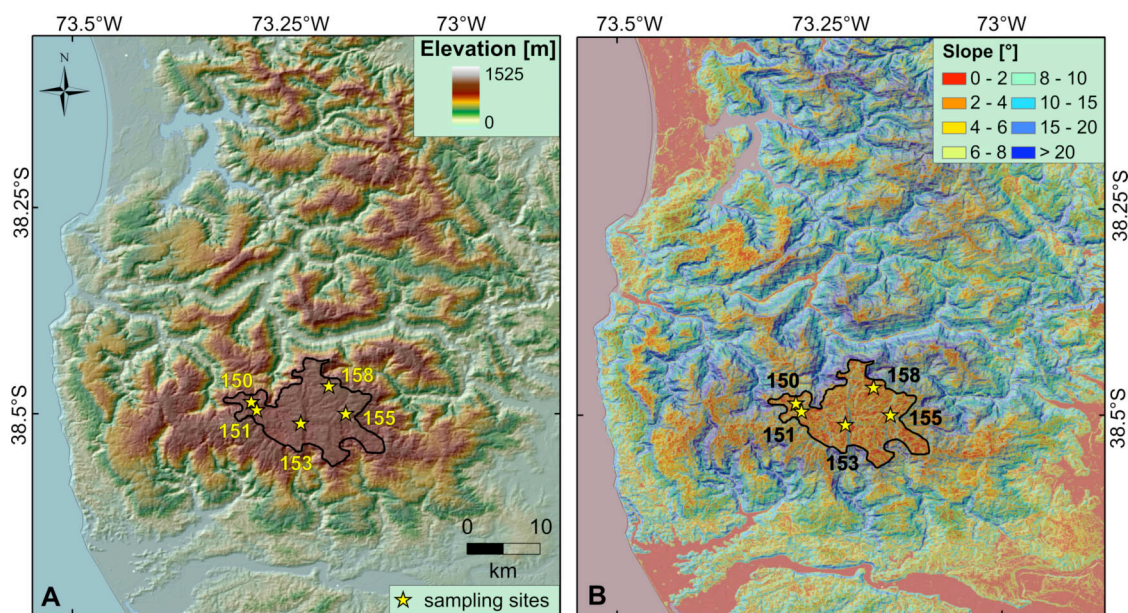


Fig. 4.2: Low-relief upland on top of the Coastal Cordillera at an elevation of about 750 m. (A): Digital elevation model with sampling sites. (B): Local slope map with sampling sites. Note the low slope of the surface.

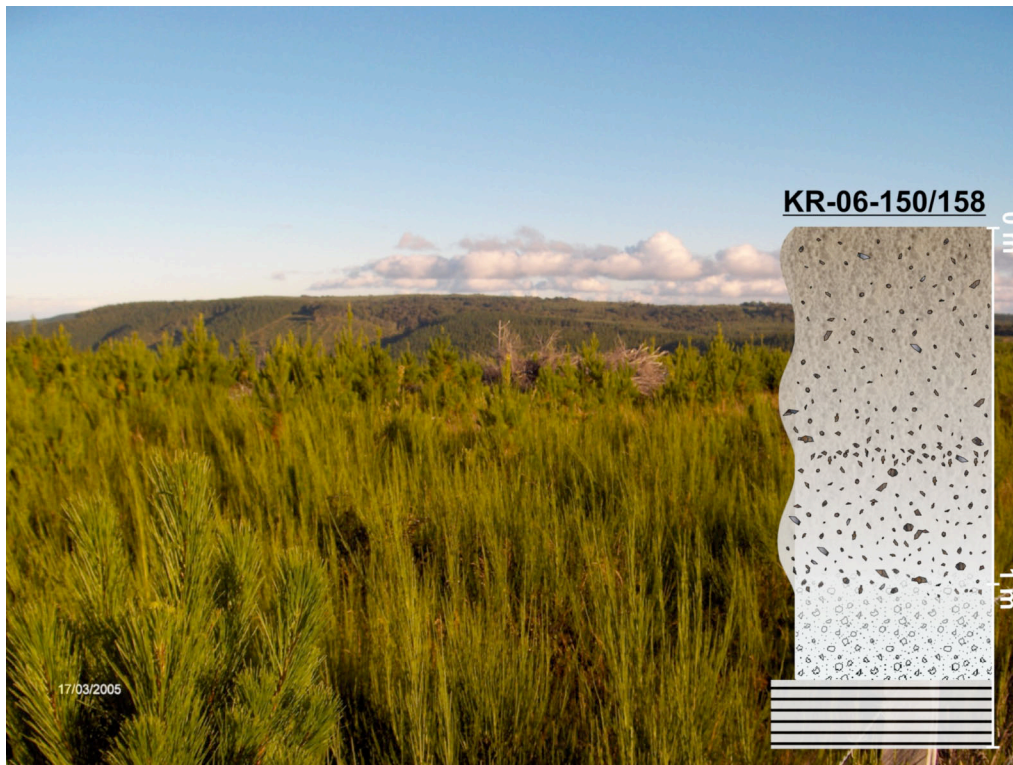


Fig. 4.3: Low-relief upland in the Coastal Cordillera at an elevation of 750 m. The inset represents a typical weathering profile on this surface, bedrock – saprolite – regolith – soil. The basement schists constitute the base of the profile. They grade to reddish, clay-rich, acidic ultisols (U.S. Soil Taxonomy, 2003).

We used nuclide-production rates of  $5.1 \pm 0.3$  for  $^{10}\text{Be}$  (Stone, 1999), and  $31.1 \pm 1.9$  for  $^{26}\text{Al}$  (Nishiizumi et al., 1989; Bierman and Steig, 1996). These production rates were scaled according to Dunai (2000) and Stone (2000), and we found that our results are not sensitive to the scaling method employed (Fig. 4.5). We assumed a 10 % uncertainty on both  $^{10}\text{Be}$  and  $^{26}\text{Al}$  scaled production rates. All samples were corrected for topographic shielding and sample depth (Dunne et al., 1999). According to the clay and sand content of the regolith and soil layers, we assume an average density of  $1.45 \text{ g}\cdot\text{cm}^{-3}$  in our calculations. Additionally, we account for potential vegetation cover with a 5 % error on the production rate. Incorporation of these uncertainties aggregates to a total error of 18.5 % on our calculated results.

Based on our measured cosmogenic  $^{10}\text{Be}$  and  $^{26}\text{Al}$  concentrations we quantitatively assessed the viability of different tectono-geomorphic scenarios. This analysis was then used to identify the scenario that best fitted geomorphic and geologic conditions, and this, in turn, was used to place constraints on the timing of the onset and subsequent rate of uplift in the Coastal Cordillera.

#### 4.4 Results

The results of our measurements and calculations are summarized in Table 4.1. We measured paired radionuclides in order to be able to identify complex exposure histories. The production rate of  $^{26}\text{Al}$  and  $^{10}\text{Be}$  is in the ratio 6 : 1, but if samples experience a period of dominant decay without significant production, this ratio will decline and approach a new equilibrium since  $^{26}\text{Al}$  decays faster than  $^{10}\text{Be}$  (Lal, 1991). Our samples exhibit  $^{26}\text{Al}/^{10}\text{Be}$ -ratios well below 6.1 and concentrations far from

saturation. This indicates that they have experienced a complex exposure history with a period of decay dominance, either as a result of prolonged burial following exposure, or due to prolonged residence at a depth where the rate of decay exceeded the rate of production (Fig. 4.4).

Sample ID	Latitude [°S]	Longitude [°W]	Sample elevation [m asl]	Sample depth [cm below surface]	Shielding factor	Quartz mass [g]	Be-9 carrier mass [g]	Al-27 carrier mass [g]	$\sigma$ Be-9 and Al-27 carrier mass [%]	ICP Al-27 mass [g]	$\sigma$ ICP Al-27 mass [%]
KR-06-150	-38.49	-73.27	718	75	1.0000	27.27	2.53E-04	1.55E-03	2.00	1.64E-03	2.00
KR-06-151	-38.49	-73.26	664	60	0.9998	27.58	2.54E-04	1.55E-03	2.00	1.78E-03	2.00
KR-06-153	-38.51	-73.20	729	60	1.0000	27.49	2.55E-04	1.55E-03	2.00	1.91E-03	2.00
KR-06-155	-38.50	-73.14	771	50	1.0000	26.36	2.63E-04	1.54E-03	2.00	1.74E-03	2.00
KR-06-158	-38.46	-73.17	799	30	1.0000	30.49	2.53E-04	1.55E-03	2.00	1.79E-03	2.00
KR-06-Blank	---	---	---	---	---	---	2.57E-04	1.55E-03	2.00	1.84E-03	2.00

Sample ID	Be-10/9 AMS result	$\sigma$ Be-10/9 AMS result [%]	Al-26/27 AMS result	$\sigma$ Al-26/27 AMS result [%]	Be-10 nuclide concentration [at/g]	$\sigma$ Be-10 nuclide concentration [%]	Al-26 nuclide concentration [at/g]	$\sigma$ Al-26 nuclide concentration [%]	Al-26/Be-10 ratio
KR-06-150	7.63E-13	2.59	1.78E-12	2.48	4.57E+05	3.42	2.38E+06	3.20	5.21
KR-06-151	3.98E-12	2.49	8.01E-12	1.93	2.44E+06	3.22	1.15E+07	2.78	4.73
KR-06-153	2.04E-12	2.53	4.09E-12	1.96	1.25E+06	3.27	6.34E+06	2.81	5.08
KR-06-155	1.30E-12	2.59	3.03E-12	1.97	8.51E+05	3.34	4.46E+06	2.82	5.24
KR-06-158	1.23E-12	2.84	2.63E-12	2.03	6.70E+05	3.56	3.45E+06	2.86	5.14
KR-06-Blank	2.48E-14	13.61	5.99E-15	33.33	---	---	---	---	---

Sample ID	Scaling factor (Dunai, 2000)	Be-10				Al-26					
		Production rate [at/g/yr] (Stone, 1999)	$\sigma$ production rate [%]	Scaling factor (Stone, 2000)	Dunai-corrected production rate [at/g/yr]	Stone-corrected production rate [at/g/yr]	Production rate [at/g/yr] (Nishiizumi, 1989; Bierman, 1996)	$\sigma$ production rate [%]	Scaling factor [Stone, 2000]	Dunai-corrected production rate [at/g/yr]	Stone-corrected production rate [at/g/yr]
KR-06-150	1.54	5.1	5.88	1.67	7.86	8.49	31.1	6.11	1.67	47.93	51.87
KR-06-151	1.49	5.1	5.88	1.61	7.60	8.22	31.1	6.11	1.62	46.33	50.23
KR-06-153	1.59	5.1	5.88	1.71	8.10	8.73	31.1	6.11	1.72	49.41	53.35
KR-06-155	1.65	5.1	5.88	1.78	8.43	9.07	31.1	6.11	1.78	51.41	55.39
KR-06-158	1.68	5.1	5.88	1.80	8.55	9.20	31.1	6.11	1.81	52.15	56.19

Sample ID	$\sigma$ scaling [%]	$\sigma$ field [%]	$\sigma$ Be [%]	$\sigma$ Al [%]	$\sigma$ total [%]
KR-06-150	10.00	5.00	13.09	13.14	18.54
KR-06-151	10.00	5.00	13.04	13.04	18.44
KR-06-153	10.00	5.00	13.05	13.05	18.45
KR-06-155	10.00	5.00	13.07	13.05	18.47
KR-06-158	10.00	5.00	13.12	13.06	18.51

**Table 4.1: Summary of AMS-measurements, nuclide concentrations, nuclide ratios, production rates, scaling, and errors. The samples were spiked with a commercial  $^9\text{Be}$  carrier (Spectrosol) with a known  $^{10}\text{Be}/^9\text{Be}$  ratio of  $\sim 1\text{-}2\cdot 10^{-14}$ . A laboratory blank prepared in tandem with the samples provided low  $^{10}\text{Be}$  and  $^{26}\text{Al}$  yields. These blank values have been subtracted from the appropriate samples to derive the concentrations shown.**

The former (burial-re-exposure) scenario occurs in three stages. First, a low-relief surface is carved into bedrock and experiences initial exposure to cosmic radiation and acquires a concentration of cosmogenic nuclides. This bedrock surface is then buried to a depth where shielding becomes significant and the initial concentrations of  $^{26}\text{Al}$  and  $^{10}\text{Be}$  decrease differentially causing a change in the  $^{26}\text{Al}/^{10}\text{Be}$  ratio. Finally, the surface experiences renewed erosion and the samples reach a depth where cosmogenic-nuclide production exceeds decay before eventually being re-exposed at the surface.

The latter (two-stage exposure) scenario involves progressive sample ascent from depth relative to the surface in two discrete periods of erosion. First, during the initial phase a sample moves upward relative to the eroding bedrock surface to a depth sufficiently shallow to enable minor cosmogenic nuclide production. Prolonged residence at this depth  $z$  then occurs such that decay exceeds production. Subsequently further erosion leads to the movement of the sample to its presently observed depth of  $< 75$  cm where production exceeds decay.

The burial-re-exposure scenario implies that the samples were located at the bedrock surface prior to sample burial and after the removal of the shielding sediments. This means that erosion after burial would have had to stop exactly at the exhumed surface. This scenario, however, is highly implausible and unrealistic in the light of the tectonic, climatic, and geomorphic history of the region.

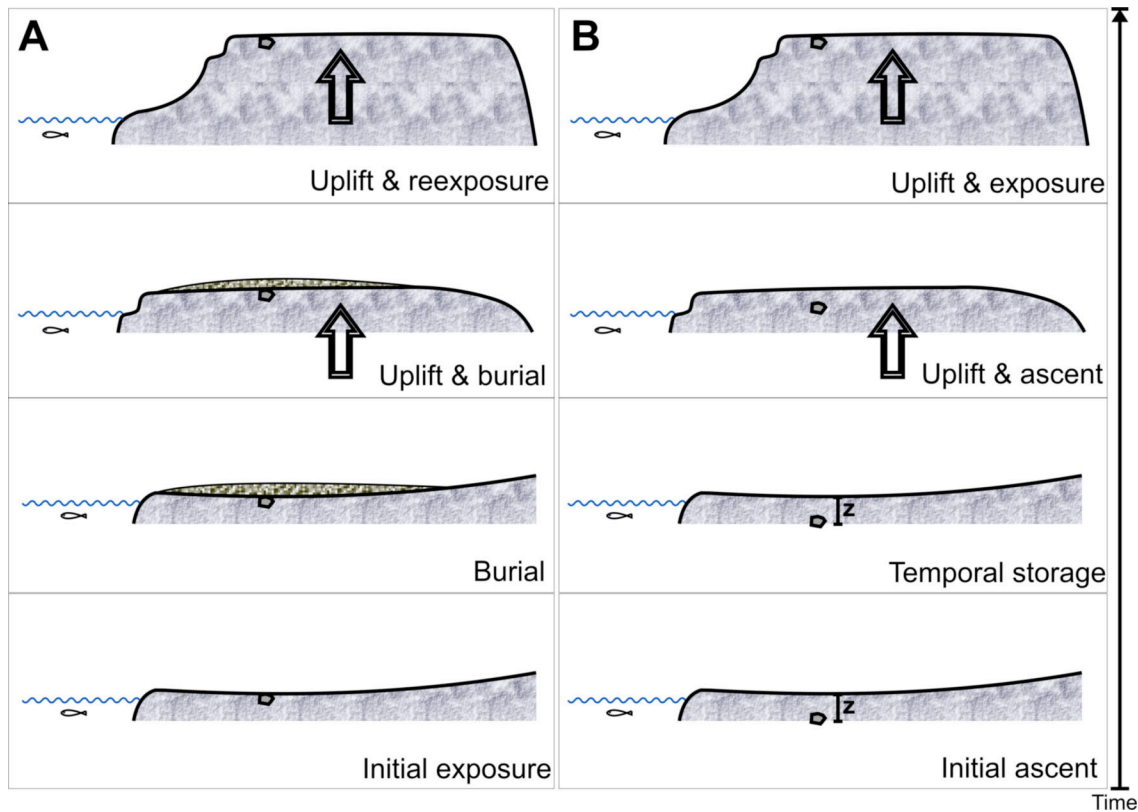


Fig. 4.4: Two alternative evolutionary sequences of surface development in the Coastal Cordillera. (A): Scenario A assumes the complete erosion of the shielding sediments without any erosion of the bedrock. (B): Scenario B implies a progressive ascent of the samples due to slow successive surface erosion initiated by tectonic uplift.

The two-stage exposure scenario requires progressive erosional exposure of the samples towards the surface to a depth where they resided for a certain period. This is viable if the surface were in a relatively stable position close to base level and was not in a topographic setting conducive to enhanced erosion. However, the second phase of erosion requires a change in erosional regime and a likely cause of this is a lowering of base level. Theoretically, surface uplift might have occurred earlier and erosion may have been restricted to a subsequent period of erosion. Nevertheless, we argue that this is not a realistic assumption since: 1) it is not reasonable in this environment to assume that surface uplift would not have been accompanied by erosion; and 2) the extension and flatness of the surface prevent efficient material transport rendering the possibility to instantly remove about 4 m of the surface impractical. We thus propose that the second phase of erosion is indeed coupled to base level fall induced by tectonic uplift.

Conclusively, the two-stage exposure scenario is our favored interpretation as it requires fewer assumptions and does not imply geomorphologically implausible conditions. The nuclide-accumulation history inferred for the two-stage exposure scenario can be mathematically described by an equation from Heisinger (1998).

$$N_{CN}(x, z) = P_{CN}(z) \cdot \tau_{CN} \cdot e^{-\frac{x}{\tau_{CN}}} + P_{CN}(h) \cdot \tau_{CN} \cdot (1 - e^{-\frac{x}{\tau_{CN}}})$$

$N_{CN}(x, z)$  is the concentration of cosmogenic nuclide CN after the ascent from depth  $z$  and an exposure time  $x$ .  $P_{CN}(z)$  is the production rate of the cosmogenic nuclide at sea level at depth  $z$ .  $P_{CN}(h)$  is the production rate of cosmogenic nuclides at elevation  $h$  at

the depth below the surface where the sample was collected. The increase in production rate that would occur in response to any increase in surface elevation is not included in the calculations. However, end-member tests show that depth  $z$  is very robust and insensitive to changes of  $P_{CN}(h)$  within the possible altitudinal range of our working area.  $\tau_{CN}$  is the mean life of cosmogenic nuclides, and we used  $\tau_{Al} = 1.02 \pm 0.04$  Ma (Norris et al., 1983) and  $\tau_{Be} = 2.18 \pm 0.09$  Ma (Hofmann et al., 1987). With this equation we can calculate the depth at which the samples resided temporarily after creation of a low-relief surface and prior to their final exposition and the exposure time near the surface. Additionally, we can estimate the erosion rate at which the samples ascended towards the surface, the time of ascent, and the uplift rate of the surface.

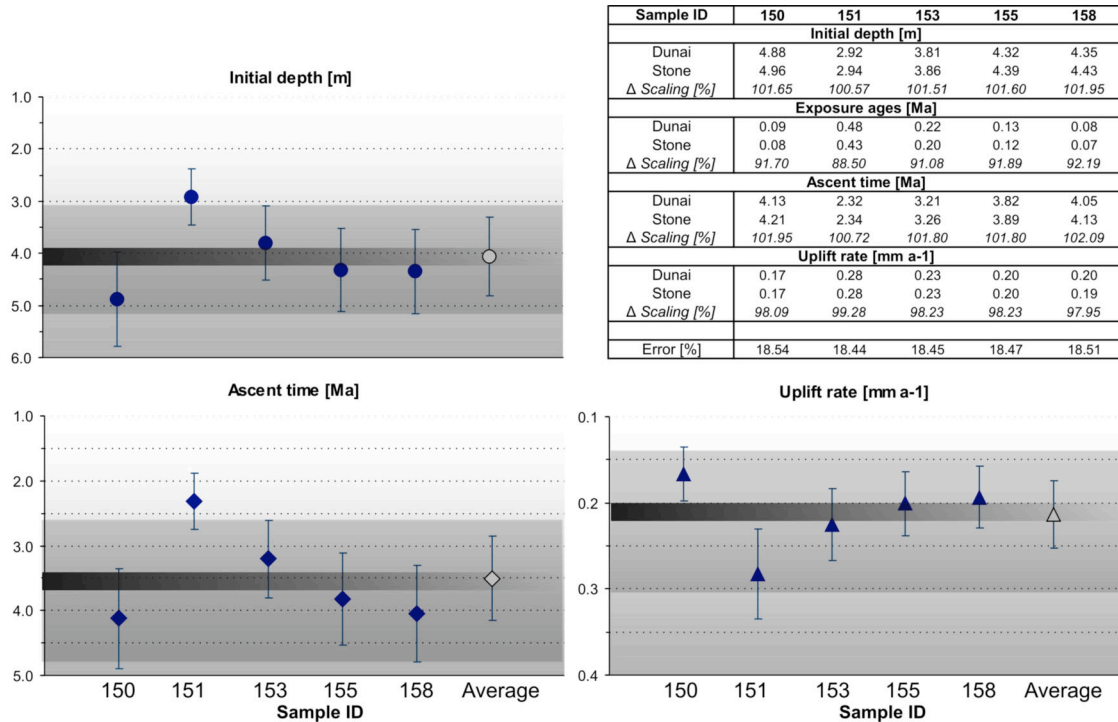


Fig. 4.5: Depth, ascent time, and uplift rates calculated based on the equations from Heisinger (1998). The table documents the difference between two scaling methods (Dunai, 2000; Stone, 2000). Note that the discrepancies are negligible, hence, we apply the scaling of Dunai (2000). Initial sample depth (first stage in scenario B) ranges from 2.92 to 4.88 m. The ascent time of the samples (from the first to the last stage in scenario B) is in the range of 2.32 to 4.13 Ma. The resulting uplift rates comprise values between 0.17 and 0.28 mm a<sup>-1</sup>. In average, depth, ascent time, and uplift rate provide values of 4 m, 3.5 Ma, and 0.21 mm a<sup>-1</sup>, respectively.

Our analysis gives values for  $z$  ranging from 2.92 to 4.88 m including analytical errors (Fig. 4.5). Furthermore, we can identify the erosion rate of the surface by testing the  $^{26}\text{Al}/^{10}\text{Be}$ -ratios in the Heisinger plots for different erosion rates. Due to the humid climate in our working area it is not reasonable to assume zero erosion. In fact, erosion rates slower than 0.001 mm a<sup>-1</sup> do not explain our data well. However, erosion rates faster than 0.001 mm a<sup>-1</sup> imply a saturation concentration that is lower than our measured values. Therefore, we conclude that the best-fit average erosion rate approximates 0.001 mm a<sup>-1</sup> (Fig. 4.6). Furthermore, we can calculate the time required for the samples to have ascended from depth  $z$  to their present position. Dividing the best-fit erosion rate of 0.001 mm a<sup>-1</sup> by the difference between depth  $z$  and the depth position of each sample, we derive an ascent time of 2.3 to 4.1 Ma. Since the samples started to ascend in response to a change in erosional regime which we attribute to base-level lowering as discussed above, these ages mark the onset of range uplift. In

turn, based on the present-day elevation this provides average uplift rates between 0.17 and 0.28 mm a<sup>-1</sup>, including analytical errors.

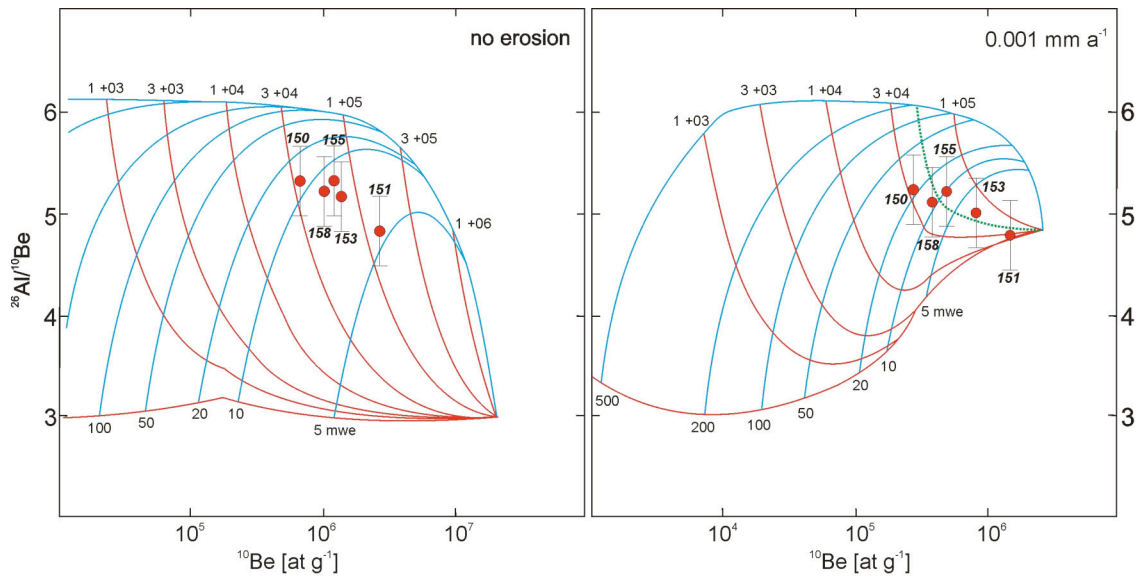


Fig. 4.6: Nuclide-ratio plots following Heisinger (1998). In light of the humid climate, the case of no erosion is an invalid assumption. In addition, isolines in the no-erosion case do not fit the data. Note that nuclide concentrations in the samples cannot be explained with erosion rates greater than 0.001 mm a<sup>-1</sup> (1 m Ma<sup>-1</sup>). An erosion rate of 0.001 mm a<sup>-1</sup> fits the data reasonably well.

## 4.5 Discussion

Our results obtained from measurements of concentrations of cosmogenic <sup>10</sup>Be- and <sup>26</sup>Al in in-situ quartz clasts allow two different interpretations – either burial and re-exposure or two-stage progressive erosion and exposure of the surface. On the basis of geomorphic considerations we favor the latter scenario, and suggest that our sampled low-relief upland was initially cut across bedrock and graded to sea level and that this subsequently experienced a second phase of erosion in response to base-level fall associated with a major uplift event. We are aware of the uncertainties inherent in our calculations, such as potential vegetation or snow cover, regolith density, and time-averaged erosion rates, and account for them by in our estimated errors and by interpreting ages and uplift rates as ranges rather than single values. Nevertheless, we stress the importance of the local tectonic and geomorphic context in the interpretation of our cosmogenic-nuclide data. Taking these considerations into account, our results suggest that the Coastal Cordillera started to uplift about 2 to 5 Ma ago. However, only one sample defines the lower end of this range, whereas the other samples document uplift to have started between 2.6 and 4.8 Ma (Fig. 4.5). Inferred uplift rates span a range between 0.14 to 0.34 mm a<sup>-1</sup>. Discarding the “youngest” sample the uplift rate for the surface averages 0.21 mm a<sup>-1</sup> (Fig. 4.5).

Our data show that the Coastal Cordillera of the study area is a Pliocene/Quaternary feature. Consequently, the observed morphotectonic segmentation, including adjacent sectors, must also have been established in the Pliocene. Offshore forearc basins along the coast of our working area record extension and subsidence during late Miocene. In contrast, these basins were inverted,

shortened and uplifted during the Pliocene, and a compressional regime continues to the present (Melnick and Echtler, 2006a). During inversion these basins experienced at least 1500 m of uplift, documented by subaerial exposure of early Pliocene lower bathyal siltstones (Melnick and Echtler, 2006a; Finger et al., 2007).

The history of the offshore forearc basins and the development of the onshore Coastal Cordillera indicate that they must have been uplifted contemporaneously. Both are the expression of regional changes in the geodynamic conditions of the southern Andean margin. Furthermore, apatite fission-track dating of samples collected in a vertical transect in the basement of the Coastal Cordillera, record an inflection point in the age-elevation distribution at approximately 5 Ma (Glodny et al., 2007). This inflection suggests an episode of accelerated denudation at a mean rate of  $\sim 0.20 \text{ mm a}^{-1}$  beginning 5 Ma ago compared with a previously lower rate of  $0.04 \text{ mm a}^{-1}$  (Glodny et al., 2007). Both the onset of accelerated denudation and the offshore surface uplift indicated by geologic data are in accord with our data interpretation. Interestingly, the denudation rates based on apatite fission-track thermochronology are similar to our inferred rate of surface uplift implying that soon after the initiation of uplift that created the Coastal Cordillera an approximate topographic steady-state was attained, albeit some localities, such as our study area low-relief upland, experiencing limited erosion.

These pronounced changes in forearc behavior during the early Pliocene require a significant change in boundary conditions in the subduction system. Indeed, our proposed timing for the onset of uplift accords with the interpretation that in late Miocene to early Pliocene time the subduction mode in south-central Chile switched from erosion to accretion (Bangs and Cande, 1997; Melnick and Echtler, 2006a). It has been proposed that one factor controlling the mode of subduction in this environment is the thickness of sediments in the trench (von Huene and Scholl, 1991; Lamb and Davis, 2003; Cliff and Vannucchi, 2004). In fact, many studies along the Chile margin reveal that sediment flux varies significantly according to the prevailing climate conditions and topographic barriers on the subducting plate (Lamb and Davis, 2003). Maximum sediment flux in the trench depositional system, however, has been shown to coincide with glacial periods (Scholl et al., 1970; Lamy et al., 1999; Hebbeln et al., 2007). This suggests that with the onset of global cooling and the initiation of subsequent glaciation in Patagonia about 6 Ma ago (Mercer and Sutter, 1982; Zachos et al., 2001), the trench-fill thickness increased significantly (Bangs and Cande, 1997; Melnick and Echtler, 2006a). Consequently, the enhanced subduction of sediments appears to have stopped subduction erosion and forced subduction accretion (Lamb and Davis, 2003). Similar to the uplift of the inverted submerged basins, the uplift of the now subaerial sectors of the forearc might thus be explained by: 1) basal underplating of sediments, which is supported by observations in the subduction channel (Bohm et al., 2002; Lohrmann, 2002; Hackney et al., 2006); 2) internal deformation of the forearc as the taper angle of the forearc wedge changed due to frontal accretion (Davis et al., 1983; Melnick and Echtler, 2006a); or 3) a combination of both mechanisms. We also suggest that the coincidence between the onset of glaciations in southern South America and the change in subduction mode implies that the emergence of the Coastal Cordillera in south-central Chile may ultimately be linked to the effects of global cooling on the surface-process system.

## 4.6 Conclusions

Forearc systems are among the most sensitive recorders of subduction dynamics, although interrelationships between subduction and surface processes are difficult to assess. Surface dating with cosmogenic nuclides provides indications of the timing of forearc uplift and thus allows the detection and evaluation of controlling mechanisms.

We have dated an uplifted low-relief surface in the Coastal Cordillera of south-central Chile with cosmogenic  $^{10}\text{Be}$  and  $^{26}\text{Al}$  in order to elucidate the timing of tectonic uplift in this forearc region. This has provided insights into recent morphotectonic segmentation, changes in the forearc deformation, and the role of a significant switch in the subduction mode.

More specifically, our results suggest that the uplift of the Coastal Cordillera started 2.6 to 4.8 Ma ago and that therefore the range constitutes a tectonically active Pliocene to Quaternary feature. Our data interpretation inferring surface uplift at this time are compatible with other data from this region. The surface-uplift rates are of the order of  $\sim 0.21 \text{ mm a}^{-1}$  and similar to rates of denudation of  $0.20 \text{ mm a}^{-1}$  derived from apatite fission-track thermochronology. This implies that the surface uplift event we document prompted an increase in denudation rates that rapidly matched uplift rates and established an approximate steady-state topography. Our data corroborates a major change in subduction dynamics that occurred  $\sim 5 \text{ Ma}$  ago related to a change from subduction erosion to accretion. Subduction accretion probably started due to the significant thickening of sediments in the trench controlled by the onset of glaciation in Patagonia. This switch in subduction mode substantially modified the pattern of forearc deformation and apparently initiated the uplift of the Coastal Cordillera. Additionally, on the basis of our data we propose that the present-day forearc segmentation was established in the Pliocene and did not exist before the formation of the Coastal Cordillera. This in turn implies that in contrast to short-lived earthquake-rupture segments morphotectonic segments are long-lived phenomena that appear to be capable of persisting over millions of years.

## Acknowledgements

This work was funded by Deutsche Forschungsgemeinschaft through the Leibniz Award to Manfred Strecker (STR373-18-1), the A. Cox fund of Stanford University, and supported by the GeoForschungsZentrum Potsdam as well as the DAAD, the German Academic Exchange Program, to Katrin Rehak. We appreciate discussions with Maria Mardones, Tim Vietor, Bodo Bookhagen and Daniel Melnick.

## 5. Late Pleistocene landscape evolution in south-central Chile constrained by luminescence and stable cosmogenic nuclide dating

### Abstract

*Subduction margins constitute highly dynamic settings shaped by tectonic deformation and surface processes. In order to understand the development of these landscapes and distinguish between tectonic and climatic forcing it is fundamental to quantify geomorphic rates on different time scales.*

*Here, we present new luminescence and cosmogenic-nuclide ages of geomorphic markers in the Coastal Cordillera and the Central Depression of south-central Chile. Although this region provides an ideal setting to elucidate the response of surface processes to climatic and tectonic forcing, it attained few attention due to intricacies in quantifying the age of depositional surfaces. However, we use optically stimulated luminescence and stable cosmogenic nuclides ( $^3\text{He}$ ,  $^{21}\text{Ne}$ ) to constrain exposure and burial of conglomeratic units constituting the spatially most extensive surfaces in the Central Depression and characteristic valley fills in the Coastal Cordillera. These valley fills record a tectonically induced flow reversal in the formerly westward draining Pellahuén river. We propose that the defeat of the river is controlled by local uplift above a blind reverse fault. Based on the exposure and burial ages, we constrain the timing of flow reversal, derive late Pleistocene incision and uplift rates, and discuss these results in the light of tectonic as well as climatic influences. The extensive depositional surfaces in the Central Depression formed 150 to 350 ka ago, probably as glacial outwash fans. The valley fills in the Coastal Cordillera bracketing the flow reversal show ages of 80 and 255 ka, respectively. Incision rates approximate  $0.45 \text{ mm a}^{-1}$ , in contrast to short-term uplift rates of  $0.88 \text{ mm a}^{-1}$ . In turn, the latter are significantly higher than independently derived long-term surface-uplift rates.*

*Consequently, we conclude that tectonic uplift in this region varies significantly in time and space and appears to be accelerating during the late Pleistocene. Nevertheless, our data proposes that sediment accumulation is primarily related to glacial cessation periods and hence climatically driven.*

**KEYWORDS:** *cosmogenic nuclides, forearc, uplift, incision, geomorphology*

### 5.1 Introduction

Landscape evolution in tectonically active regions is characterized by the interplay between climate and tectonics determining erosion, sediment transport, and accumulation. Sedimentary geomorphic markers can thus provide important information on the deformation and climate history of active margins.

The tectonically active margin of south-central Chile has been subjected to significant changes in climatic and tectonic conditions during the late Miocene- early Pliocene boundary, i.e. the onset of Patagonian glaciation about 6 Ma ago (Mercer and Sutter, 1982; Zachos et al., 2001) and the subsequent shift from subduction erosion to accretion around 5 Ma ago (Bangs and Cande, 1997; Melnick and Echtler, 2006a). This shift in subduction mode initiated the inversion of offshore forearc basins (Melnick and Echtler, 2006a) as well as the uplift and accelerated exhumation of the Coastal Cordillera since about 4 Ma (Glodny et al., 2007; Rehak et al., submitted). However, late Quaternary uplift rates appear to be still an order of magnitude higher than Pliocene-averaged uplift rates (Kaizuka et al., 1973; Nelson and Manley, 1992; Bookhagen et al., 2006a; Melnick et al., 2006; Rehak et al., submitted) suggesting that tectonic uplift may vary through time. Active uplift during late Quaternary is also reflected by elevated beach berms, flights of marine terraces, dammed lakes, as well as tectonically disturbed drainage patterns (Kaizuka et al., 1973; Nelson and Manley, 1992; Mardones and Reuther, 1999; Bookhagen et al., 2006a; Melnick et al., 2006; Rehak et al., 2008). This is corroborated by structural, seismic, and geodetic data documenting pronounced active internal deformation of the south-central Chile forearc (Bohm et al., 2002; Haberland et al., 2006; Melnick et al., 2006; Moreno et al., submitted). Thus, differential, localized fault-related uplift is also likely responsible for a prominent drainage reversal, which is recorded in fluvial conglomerates in paleo-valleys in the Coastal Cordillera that were formerly adjusted to the Pacific coast (Rehak et al., 2008). Similar conglomerates also constitute extensive, gently sloping depositional surfaces in the Central Depression between 38° and 39°S, a low-relief corridor between the Coastal Cordillera in the west and the Main Cordillera in the east (Fig. 5.1). Nevertheless, it is not known when the flow reversal occurred and whether it is induced by a regional acceleration of uplift or controlled by fault displacement. Additionally, it is not understood whether and which relations exist between accumulation as well as incision of the conglomerate sequences, tectonic uplift, and climatic forcing. The fluvial deposits are thus a key to understand the short-term tectonic and geomorphic evolution of this forearc and provide insights into the principles of sediment routing and storage in this tectonically active environment that has also been affected by climatic changes in the past.

Here, we derive ages and rates of landscape evolution on a time scale of  $10^5$  years by dating the depositional surfaces in the Central Depression with cosmogenic  $^3\text{He}$  and  $^{21}\text{Ne}$ . In a second step, we test and complement these surface-exposure ages by dating sandy intervals in the conglomerates in the Coastal Cordillera using optically stimulated luminescence.

## 5.2 Regional setting

The forearc of south-central Chile between 37.5° and 38.5°S is part of the South Andean accretionary margin (Bangs and Cande, 1997; Melnick and Echtler, 2006a) and consists of three major morphostructural provinces: the Coastal Cordillera in the west, the north-south oriented Central Depression, and the Main Cordillera in the east. The basement of the Coastal Cordillera comprises high-pressure schists, metabasites, accreted metacherts, and serpentinites related to a Permo-Triassic accretionary wedge and a Carboniferous granitic batholith associated with a late Paleozoic arc domain (Fig. 5.1) (e.g. Aguirre Le-Bert et al., 1972; Hervé, 1977; Glodny et al., 2005). The range is characterized by numerous reactivated north-northeast, west, and northwest striking Paleozoic faults with strike-slip kinematics (Fig. 5.1) (Mordojovich, 1981; Echtler et al., 2003; Rosenau, 2004; Melnick and Echtler, 2006b; Glodny et al., in

press). It has been shown that the Coastal Cordillera started to uplift during the Pliocene,  $\sim 4$  Ma ago, with an average uplift rate of  $0.2 \text{ mm a}^{-1}$ , coeval with the inversion of offshore forearc basins (Melnick and Echtler, 2006a; Rehak et al., submitted).

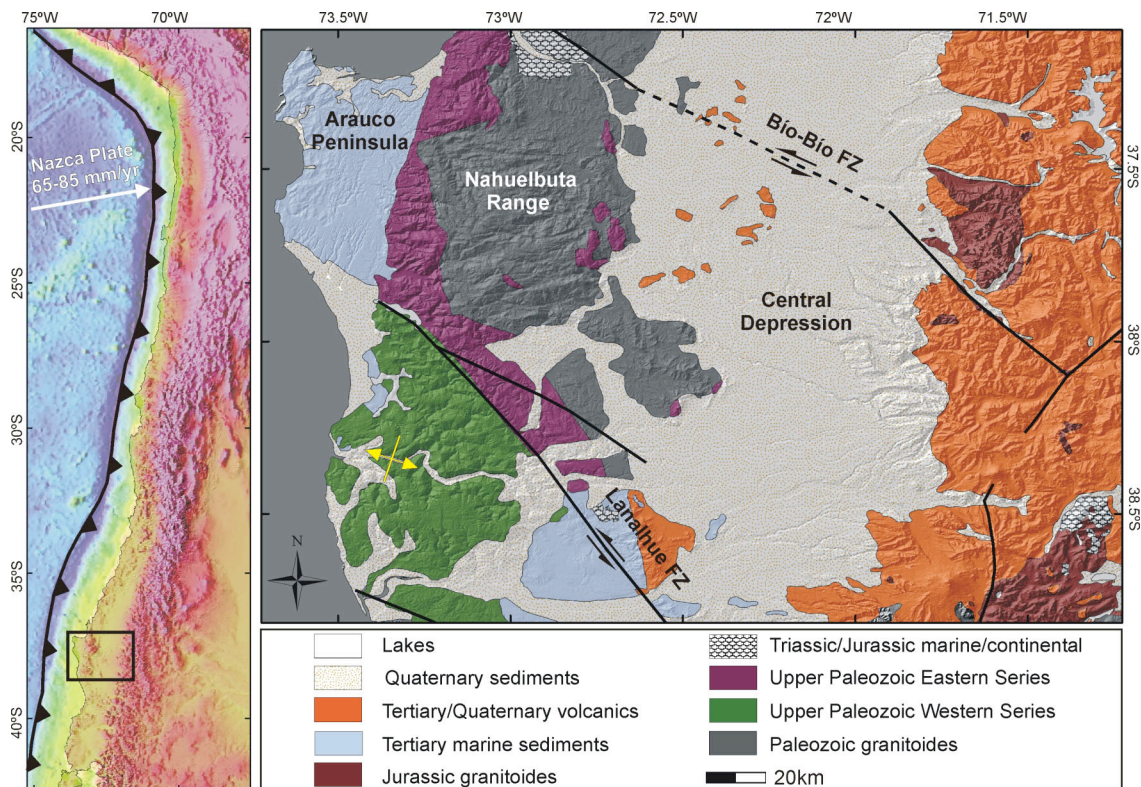


Fig. 5.1: Study area in the forearc of south-central Chile. The geological map delineates the main lithologic units and structures (modified after Sernageomin, 2003). The yellow arrow marks the location of the tectonically induced flow reversal.

The Central Depression is a low-relief sector of tectonic genesis that has been argued to persist since Oligocene (Muñoz et al., 2000). The basement of the Central Depression is inferred to consist of the same Paleozoic metamorphic rocks as the Coastal Cordillera and is overlain by up to 3000 m of marine and terrestrial sediments (Fig. 5.2) (Illies, 1967; Muñoz et al., 2000; Jordan et al., 2001). The oldest forearc-related sedimentary units south of the Arauco peninsula are the Eocene San Pedro and Pupunahue Formations characterized by  $\sim 1000$ -m-thick sandstones with interbedded conglomerates, shales, and coal (Illies, 1967). These continental series are overlain by  $\sim 1000$ -m-thick Miocene marine sediments (Darwin, 1846; Katz, 1963; Illies, 1967; Finger et al., 2007; Encinas et al., 2008). The Pliocene continental Mininco Formation marks the shift from marine to continental deposition and consists of pyroclastic units, bedded sandstones, and siltstones (Muñoz-Cristi, 1960). This unit is spatially irregularly overlain by volcanoclastics and conglomerates of the Malleco formation which constitute the depositional surfaces in the Central Depression (Fig. 5.2) (Suárez and Emparan, 1997). This formation comprises oligomictic weathered conglomerates comprising andesitic and basaltic pebbles that have been termed “rodados multicolores” by Hauser (1970), who established their fluvial origin and eastern (arc) provenance based on systematic imbrication indicating westward flow (Hauser, 1983). Interestingly, in the Patagonian foreland similar units were first described by Darwin (1846), who termed them “Patagonian gravels”, and later by Mercer (1976), who proposed that these deposits were deposited between 1.0 and 3.5 Ma ago as glacial outwash related to early Pleistocene glaciations. Maximum-age estimates for the “rodados multicolores” in the south-central Chile forearc were provided by two K/Ar-ages on lava and obsidian layers, intercalated with the clastic

formations. They were dated to 1.3 to 3.4 Ma (Suárez and Emparan, 1997) and  $760 \pm 210$  ka (Vergara and Munizaga, 1974), respectively. These dated units are located on the eastern border of the Central Depression and overlain by the multicolored conglomerates, but the age of the gravel surfaces was not known. These surfaces are geomorphically continuous, cover major parts of the Central Depression in south-central Chile, and gently slope towards the west.

Quaternary		Pleistocene	Malleco Fm.	conglomerates ("rodados multicolores")	continental
		Pliocene			
Tertiary	Neogene	Miocene	(Navidad Fm.)	clastic sediments	marine

Fig. 5.2: Schematic stratigraphy of the Central Depression around 38° to 39°S (Muñoz-Cristi, 1960; Suárez and Emparan, 1997). The investigated sediments can be assigned to the Malleco Formation.

The andesitic-basaltic conglomerates that constitute these fans can be traced through the Coastal Cordillera until the Pacific coast as remnants of fluvial valley-fills. The latter document a prominent flow reversal of the Pellahuén river that formerly crossed the entire range, drained into the Pacific ocean, and presently exhibits a wind gap at  $\sim 37.7^\circ\text{S}$  (Rehak et al., 2008). The Pellahuén valley comprises two different terrace systems with distinct lithologies that represent pre- and post-reversal deposits. The older, upper, pre-reversal terrace remnants consist of the volcanic conglomerates that originated in the Main Cordillera or they may represent reworked clasts of the large depositional surfaces in the Central Depression. In contrast, the lower post-reversal terraces are composed of locally-derived, monomict schist conglomerates integrating exclusively clasts from the metamorphic basement (Rehak et al., 2008).

The Main Cordillera in the study area comprises volcanic rocks of mainly Oligocene to Holocene age (Parada et al., 2007), which constitute the source rock of the "rodados multicolores", the andesitic-basaltic conglomerates of the Malleco Formation.

In summary, these "rodados multicolores" pose an interesting problem regarding the evolution of the tectonically influenced drainage networks and the potential superposition of climate-driven processes.

### 5.3 Methodology

The depositional surfaces in the Central Depression were sampled for cosmogenic-nuclide measurements, the pre- and post-reversal sediments within the Pellahuén valley for luminescence dating in order to quantify exposure ages and constrain the timing of tectonically-induced flow reversal, respectively.

#### 5.3.1 Cosmogenic nuclide dating

Cosmogenic nuclides develop in rocks exposed at the surface of the Earth due to the bombardment of target minerals with secondary cosmic-ray neutrons (Lal and Peters, 1967; Lal, 1991; Gosse and Phillips, 2001; Niedermann, 2002). Hence, the measurement of the concentration of cosmogenic nuclides within a rock is a function of exposure time.

Here, we measure concentrations of the stable cosmogenic nuclides  $^3\text{He}$  and  $^{21}\text{Ne}$  in olivines and pyroxenes from andesitic and basaltic conglomerates. Each analyzed sample comprises a minimum of 10 clasts with a size of 10 to 15 cm. The source rocks are mainly Oligocene to Quaternary volcanics from the Main Cordillera (Parada et al., 2007). Samples were collected from the surface and from 1 m depth (Table 5.1). We added several shielded samples from 5 to 6 m depth in order to correct for non-cosmogenic and inherited nuclide components. Furthermore, we sampled the oligomictic conglomerates constituting the upper fluvial terraces in the Coastal Cordillera to test whether these conglomerates were temporarily stored in the Central Depression or transported directly to their current position. In the latter case, their cosmogenic-nuclide concentrations are expected to be extremely low and should approximate the concentrations in the shielded samples.

We separated minerals with a grain size of 250 to 1000  $\mu\text{m}$  applying common magnetic and density separation techniques. Additionally, the samples were cleaned in a sonicator with 5 %  $\text{HNO}_3/\text{HCl}$  dilutes for 20 min. The chemical composition of each sample was determined by ICP-AES analysis. This is a prerequisite to calculate production rates which depend on the element concentrations in the minerals. Finally, aliquots of each sample were packed into aluminium-foil capsules and heated in two temperature steps, 900°C and 1750°C, in a resistance-heated ultra-high vacuum furnace at GFZ Potsdam. Condensable gases such as  $\text{H}_2\text{O}$  were frozen to a dry-ice cooled trap. Subsequently, other chemically active gases were absorbed by two Ti sponge and two ZrAl (SAES) getters in three successive steps. The cleaned noble gases were physically adsorbed on activated charcoal or a stainless steel frit in cryogenic absorbers achieving a temperature of 11 K (-262°C) by expansion cooling in a closed circuit of compressed helium at 16 bar. At successively higher temperatures the noble gases were released one after another, allowing each of them to be introduced into the mass spectrometer and analyzed separately, as required in order to prevent mutual influences reducing the accuracy of the measurement. Prior to admission of the He- and Ne-fractions to the mass spectrometer and during the measurements, the gas was exposed to activated charcoal and a stainless steel frit cooled with liquid nitrogen to reduce the background of Ar and hydrocarbons. We determined the abundances of all noble gases and the isotopic compositions of He, Ne and Ar using the sector field mass spectrometer Micromass VG 5400, which guarantees a resolution of  $m/\Delta m \geq 600$  on the multiplier detector. This is required to resolve  $^3\text{He}^+$  (3.016 amu) from  $\text{HD}^+$  (3.022 amu), allowing accurate determinations of the  $^3\text{He}/^4\text{He}$  ratios.  $^4\text{He}$  and  $^{40}\text{Ar}$  were measured with a Faraday cup, while all other

noble-gas nuclides were detected by ion counting using an electron multiplier. Noble-gas concentrations and isotopic compositions were calculated based on pipettes of a calibration gas consisting of an artificial mixture of the five noble gases in nitrogen with an enhanced  $^3\text{He}/^4\text{He}$  ratio of  $(21.66 \pm 0.24) \cdot 10^{-6}$ . Further details of the analytical procedure and data reduction methods can be found in Niedermann et al. (1997).

In addition to stepwise heating, aliquots of two samples were crushed in a bellows-tightened spindle press under ultra-high vacuum conditions in order to assess the contribution and isotopic composition of He and Ne trapped in fluid inclusions and between grain boundaries.

### 5.3.2 Luminescence dating

Luminescence dating uses a light-sensitive signal in quartz and feldspar grains that is induced by naturally occurring radioactivity and is zeroed during sediment transport when the grains are exposed to daylight (e.g. Aitken, 1998; Preusser et al., in press). In the laboratory, the latent luminescence signal is stimulated by exposure to light sources (blue and IR diodes, respectively). The intensity of the resulting light exposure is quantified by comparing the natural luminescence-emission intensity with that of known given laboratory doses administered to the sample. The amount of dose absorbed by the natural sample is called paleodose and proportional to both burial time as well as the amount of radioactivity influencing the sample per time (dose rate).

We measured the paleodose of both quartz and feldspar separates derived from two different valley fills. The samples KR-06-08/09/10 were collected from a sand layer 8 m below surface in the pre-reversal multicolored conglomerates constituting the upper terrace levels (Table 5.1). The samples KR-06-11/12/13 are related to post-reversal alluvial sands that cover the former valley floor of the Pellahuén river in the wind gap and were collected in 1 to 2 m depth. These sand layers are intercalated with thin bands of quartz pebbles.

Additionally, we collected bulk samples for gamma spectrometry to measure elements that are relevant to calculate the dose rate (K, Th, U) (e.g. Preusser and Kasper, 2001). Two grain-size fractions were separated from each sample: silt (4-11  $\mu\text{m}$ ) and fine sand (100 to 150  $\mu\text{m}$ ). However, the samples KR-06-10 and KR-06-12 were too coarse to allow extraction of a sufficient amount of silt-size grains. First, samples were treated with HCl and  $\text{H}_2\text{O}_2$  in order to remove carbonates and organic material. In the sand fraction, quartz and K-feldspar were density-separated with Na-polytungstate. No quartz could be isolated from the samples KR-06-8, -9, and -10 due to the scarcity of that mineral in the sediment. Finally, quartz samples were etched in 40 % HF for 60 min to remove any remaining feldspars and the outer rim of the quartz grains.

Paleodose was measured using the single-aliquot regenerative-dose (SAR) protocol of Murray and Wintle (2000) using a Risø DA-20 TL/OSL reader. We used blue and IR diodes to excite optically stimulated luminescence (OSL) in quartz (filter: Hoya U340) and infrared stimulated luminescence (IRSL) in feldspar (410 nm interference filter), respectively. A number of experiments, i.e. dose recovery, thermal transfer, were carried out to identify the correct measurement conditions (Wintle and Murray, 2006). Thereby, we finally used preheating for 10 s at 250°C (quartz) and 290°C (feldspar), respectively. Furthermore, we measured 5 and 12 aliquots per sample in the silt and sand fraction, respectively.

Dose rates were calculated by ADELE software (Kulig, 2005) using the concentration of dose-rate relevant elements (Table 5.1). The contribution of cosmic

radiation to the total dose rate has been corrected for elevation and geographical position. Mean sediment moisture has been assumed based on modern water content. We included an uncertainty for possible past changes in hydrological conditions. The K-content in K-feldspar was initially set at  $12.5 \pm 0.5$  % (Huntley and Baril, 1998), however, our measurements suggest that the actual value is much lower in some of our samples (see discussion below).

## 5.4 Results

### 5.4.1 Cosmogenic nuclide dating

The measured  $^3\text{He}$  and  $^{21}\text{Ne}$  concentrations and exposure ages of all samples are presented in Table 5.1. Measured  $^3\text{He}/^4\text{He}$ - and  $^{21}\text{Ne}/^{20}\text{Ne}$ -ratios are on the order of  $8 \cdot 10^{-5}$  and  $4.5 \cdot 10^{-5}$ , respectively. Blanks for  $^3\text{He}/^4\text{He}$  and  $^{21}\text{Ne}/^{20}\text{Ne}$  are atmospheric.  $^3\text{He}$ -blanks constitute in average 0.62 % of the concentrations in the samples and never more than 6.4 % (Table 5.2).

A complication of dating surfaces using stable cosmogenic nuclides is the discrimination of cosmogenic against other nuclide components such as trapped, radiogenic, and nucleogenic He and Ne. Trapped, primordial components are located in the lattice or fluid inclusions, e.g. from solution in magma and incorporation of air or water during eruption. Radiogenic and nucleogenic components can be produced by radioactive decay of U, Th, and  $^{40}\text{K}$ , or naturally occurring nuclear reactions after crystallization. Hence, in order to correct for non-cosmogenic He- and Ne-components as well as inherited cosmogenic nuclides, we additionally measured three shielded and two crushed samples. Shielded samples have  $^3\text{He}/^4\text{He}$ - and  $^{21}\text{Ne}/^{20}\text{Ne}$ -ratios on the order of  $6 \cdot 10^{-6}$  and  $3 \cdot 10^{-5}$ , respectively (Table 5.2). The low concentrations of  $^3\text{He}$  in the crushed, as well as the small  $^3\text{He}/^4\text{He}$ -ratio in the shielded samples suggest that magmatic He plays a negligible role in our samples. We thus consider all  $^3\text{He}$  measured cosmogenic. Nevertheless, we tested the robustness of the  $^3\text{He}$ -concentrations by excluding potential magmatic  $^3\text{He}$  applying the following equations (Gosse and Phillips, 2001):

$$^3\text{H}_{\text{cosmogenic}} = ^3\text{He}_{\text{furnace}} - ^3\text{He}_{\text{magmatic}} \quad (1)$$

$$^3\text{He}_{\text{magmatic}} = ^4\text{He}_{\text{furnace}} \left( \frac{^3\text{He}}{^4\text{He}} \right)_{\text{crushed}} \quad (2)$$

Sample ID	Latitude	Longitude	Altitude [m]	Sample depth [cm]	Shielding factor	Scaling factor	Sample weight MS analysis [g]	He-3			Ne-21			3He age with 3He magmatic [ka]	3He age without 3He magmatic [ka]	21Ne-age [ka]
								Production rate [at/g/a]	Corrected production rate [at/g/a]	Depth-corrected production rate [at/g/a]	Production rate [at/g/a]	Corrected production rate [at/g/a]	Depth-corrected production rate [at/g/a]			
KR-06-19	-38.301	-72.687	240	100	1.000	1.028	0.458	116.0	119.2	48.2	38.9	40.0	16.2	290 ± 26	267 ± 13	272 ± 59
KR-06-20	-38.263	-72.593	237	100	1.000	1.024	0.495	116.0	118.8	48.0	40.9	41.9	16.9	154 ± 38	146 ± 14	170 ± 11
KR-06-25	-38.410	-72.980	220	0 (60)	1.000	1.012	0.512	116.0	117.4	117.4 (68.1)	37.9	38.4	38.4 (22.3)	87 ± 16 (150 ± 28)	85 ± 6 (147 ± 10)	60 ± 7 (103 ± 12)
KR-06-15	-38.390	-72.741	230	600	1.000	1.020	0.251	116.0	118.4	0.5	32.6	33.3	0.7	---	---	---
KR-06-16	-38.427	-72.782	190	100	1.000	0.985	0.324	116.0	114.3	46.2	38.1	37.5	15.2	190 ± 32	196 ± 15	138 ± 16
KR-06-17	-38.430	-72.769	190	100	1.000	0.985	0.447	116.0	114.3	46.2	23.6	23.2	9.4	255 ± 34	263 ± 17	257 ± 28
KR-06-26	-38.446	-72.789	190	0 (60)	1.000	0.986	0.642	116.0	114.3	114.3 (66.4)	30.2	29.8	29.8 (17.3)	106 ± 9 (183 ± 15)	101 ± 7 (174 ± 11)	104 ± 11 (179 ± 19)
KR-06-24	-38.421	-72.782	120	500	1.000	0.925	0.179	116.0	107.3	1.2	35.6	33.0	0.4	---	---	---
KR-06-22	-38.246	-72.311	382	0 (60)	0.998	1.164	0.512	116.0	135.0	135.0 (78.4)	40.1	46.6	46.6 (27.1)	0 ± 21	72 ± 6 (124 ± 10)	15 ± 11 (26 ± 20)
KR-06-23	-38.246	-72.476	294	0	1.000	1.077	0.456	116.0	124.9	124.9	36.1	38.9	38.9	334 ± 19	341 ± 15	269 ± 8
KR-06-21	-38.356	-71.934	600	600	1.000	1.410	0.423	116.0	163.6	0.7	34.5	48.6	0.2	---	---	---
KR-06-29	-38.337	-73.404	48	300	1.000	0.865	0.378	116.0	100.4	6.6	26.8	23.2	1.5	---	---	---
Sample ID	Latitude	Longitude	Altitude [m]	Sample depth [m]	Moisture [%]	Water [%]	N	K [%]	Th [ppm]	U [ppm]	Minerals	Grain size [µm]	D [Gy/ka]	De [Gy]	Age [ka]	
KR-06-08	-38.386	-73.219	76	8.0	50.4	50 ± 10	12	0.26 ± 0.01	2.78 ± 0.04	0.68 ± 0.02	F	100-150	0.93 ± 0.06	168.8 ± 28.5	182 ± 33	
KR-06-08	-38.386	-73.219	76	8.0	50.4	50 ± 10	5	0.26 ± 0.01	2.78 ± 0.04	0.68 ± 0.02	FG	4-11	0.65 ± 0.08	172.7 ± 3.6	262 ± 34	
KR-06-09	-38.386	-73.219	76	8.0	51.4	50 ± 10	12	0.26 ± 0.01	2.78 ± 0.04	0.68 ± 0.02	F	100-150	0.93 ± 0.06	162.8 ± 19.8	175 ± 24	
KR-06-10	-38.386	-73.219	76	8.0	49.7	50 ± 10	5	0.26 ± 0.01	2.78 ± 0.04	0.68 ± 0.02	FG	4-11	0.65 ± 0.08	159.8 ± 24.1	249 ± 49	
KR-06-11	-38.341	-73.325	114	1.0	38.2	35 ± 10	12	1.08 ± 0.03	9.78 ± 0.11	1.96 ± 0.05	F	100-150	0.91 ± 0.07	154.6 ± 24.7	170 ± 30	
KR-06-11	-38.341	-73.325	114	1.0	38.2	35 ± 10	5	1.08 ± 0.03	9.78 ± 0.11	1.96 ± 0.05	FG	4-11	2.32 ± 0.22	41.7 ± 2.4	18 ± 2	
KR-06-11	-38.341	-73.325	114	1.0	38.2	35 ± 10	12	1.08 ± 0.03	9.78 ± 0.11	1.96 ± 0.05	Q	100-150	1.79 ± 0.17	148.2 ± 7.1	69 ± 12	
KR-06-12	-38.341	-73.325	114	1.5	33.0	35 ± 10	12	1.38 ± 0.04	9.54 ± 0.11	2.19 ± 0.06	F	100-150	2.52 ± 0.27	93.1 ± 2.3	37 ± 4	
KR-06-12	-38.341	-73.325	114	1.5	33.0	35 ± 10	6	1.38 ± 0.04	9.54 ± 0.11	2.19 ± 0.06	Q	100-150	1.78 ± 0.18	131.5 ± 5.7	74 ± 8	
KR-06-13	-38.341	-73.325	114	2.0	12.6	12 ± 4	12	1.67 ± 0.05	8.97 ± 0.10	2.00 ± 0.05	F	100-150	2.61 ± 0.24	107.2 ± 3.4	41 ± 4	
KR-06-13	-38.341	-73.325	114	2.0	12.6	12 ± 4	5	1.67 ± 0.05	8.97 ± 0.10	2.00 ± 0.05	FG	4-11	2.72 ± 0.32	119.6 ± 8.0	44 ± 6	
KR-06-13	-38.341	-73.325	114	2.0	12.6	12 ± 4	4	1.67 ± 0.05	8.97 ± 0.10	2.00 ± 0.05	Q	100-150	2.14 ± 0.23	164.7 ± 15.6	77 ± 11	

Table 5.1: Sampling details, production-rate scaling, and nuclide ages. Note that ages are calculated with considering magmatic  $^3\text{He}$  and without considering magmatic  $^3\text{He}$ . Nevertheless, both ages match very well.

Sample ID	Temperature step [°C]	He-4 [10 <sup>-8</sup> ]	He-3/4 [10 <sup>-6</sup> ]	He-3 [10 <sup>-14</sup> g]	He-3 [Mat/g]	Ne-20 [10 <sup>-12</sup> ]	Ne-22/20	Ne-21/20	Ne-21	Ne-21 [Mat/g]
KR-06-19	900	0.2344 ± 0.0118	71.94 ± 3.56	36.79 ± 2.59	9.88 ± 0.70	200.92 ± 11.77	0.0992 ± 0.0033	0.0030 ± 0.0002	0.0208 ± 0.0035	0.56 ± 0.95
	1750	0.0654 ± 0.0056	134.49 ± 15.15	19.18 ± 2.05	5.15 ± 0.55	131.68 ± 6.85	0.1042 ± 0.0009	0.0035 ± 0.0001	0.1552 ± 0.0139	4.17 ± 0.37
KR-06-20	900	0.4570 ± 0.0229	20.90 ± 2.95	19.29 ± 2.89	5.18 ± 0.78	7.69 ± 0.61	0.1036 ± 0.0036	0.0035 ± 0.0004	0.0094 ± 0.0031	0.25 ± 0.08
	1750	0.1088 ± 0.0073	68.18 ± 6.29	14.97 ± 1.48	4.02 ± 0.67	9.81 ± 0.70	0.1092 ± 0.0028	0.0085 ± 0.0007	0.1099 ± 0.0073	2.95 ± 0.20
KR-06-25	600	0.4104 ± 0.0206	22.16 ± 2.38	17.72 ± 2.11	4.76 ± 0.57	15.73 ± 0.93	0.1023 ± 0.0013	0.0030 ± 0.0003	0.0005 ± 0.0004	0.01 ± 0.15
	900	0.1226 ± 0.0062	73.33 ± 5.21	17.55 ± 1.53	4.71 ± 0.41	1.33 ± 0.53	0.1063 ± 0.0105	0.0049 ± 0.0010	0.0106 ± 0.0028	0.29 ± 0.07
KR-06-15	1750	0.1044 ± 0.0078	50.01 ± 7.43	10.19 ± 1.52	2.74 ± 0.41	28.96 ± 1.74	0.1038 ± 0.0013	0.0045 ± 0.0003	0.0869 ± 0.0096	2.33 ± 0.26
	900	0.7356 ± 0.0369	2.45 ± 0.42	7.17 ± 1.30	1.93 ± 0.35	12.41 ± 0.80	0.1018 ± 0.0016	0.0029 ± 0.0002	0.0000	0.00
KR-06-16	1750	0.0589 ± 0.0054	4.14 ± 1.76	0.97 ± 0.41	0.26 ± 0.11	16.79 ± 0.97	0.1029 ± 0.0021	0.0032 ± 0.0004	0.0149 ± 0.0073	0.40 ± 0.20
	900	0.2417 ± 0.0122	37.29 ± 2.51	27.80 ± 2.33	7.47 ± 0.63	25.22 ± 1.57	0.1028 ± 0.0046	0.0031 ± 0.0002	0.0135 ± 0.0056	0.36 ± 0.15
KR-06-17	1750	0.0532 ± 0.0052	62.31 ± 10.27	10.23 ± 1.59	2.75 ± 0.43	59.12 ± 3.34	0.1026 ± 0.0010	0.0034 ± 0.0002	0.0794 ± 0.0094	2.13 ± 0.25
	900	0.3749 ± 0.0188	46.79 ± 2.38	39.21 ± 2.80	10.53 ± 0.75	14.24 ± 1.01	0.1015 ± 0.0011	0.0034 ± 0.0005	0.0155 ± 0.0064	0.42 ± 0.17
KR-06-26	1750	0.0504 ± 0.0051	91.85 ± 15.09	10.35 ± 1.58	2.78 ± 0.42	31.74 ± 1.84	0.1023 ± 0.0017	0.0042 ± 0.0003	0.0893 ± 0.0092	2.40 ± 0.25
	900	0.1987 ± 0.0100	85.56 ± 7.38	26.48 ± 2.64	7.11 ± 0.71	7.29 ± 0.70	0.1066 ± 0.0054	0.0040 ± 0.0008	0.0123 ± 0.0056	0.33 ± 0.15
KR-06-24	1750	0.0453 ± 0.0050	297.73 ± 32.25	21.00 ± 1.68	5.64 ± 0.45	33.28 ± 1.93	0.1040 ± 0.0012	0.0052 ± 0.0004	0.1176 ± 0.0129	3.16 ± 0.35
	900	1.0602 ± 0.0531	1.02 ± 0.30	2.13 ± 0.63	0.57 ± 0.17	36.35 ± 0.75	0.1018 ± 0.0015	0.0030 ± 0.0003	0.0054 ± 0.0098	0.14 ± 0.26
KR-06-22	1750	0.0447 ± 0.0033	25.90 ± 3.39	2.29 ± 0.30	0.61 ± 0.08	16.42 ± 1.34	0.1031 ± 0.0024	0.0032 ± 0.0003	0.0096 ± 0.0050	0.26 ± 0.13
	900	1.7152 ± 0.0858	3.54 ± 0.27	33.96 ± 3.12	9.12 ± 0.84	10.45 ± 1.25	0.1020 ± 0.0040	0.0031 ± 0.0003	0.0074 ± 0.0034	0.20 ± 0.09
KR-06-23	1750	0.1898 ± 0.0102	4.11 ± 0.34	4.45 ± 0.43	1.19 ± 0.12	17.58 ± 1.52	0.0975 ± 0.0014	0.0032 ± 0.0004	0.0195 ± 0.0066	0.52 ± 0.18
	900	0.3710 ± 0.0186	113.49 ± 3.83	92.33 ± 5.57	24.80 ± 1.5	8.60 ± 1.04	0.1064 ± 0.0034	0.0050 ± 0.0005	0.0376 ± 0.0037	1.01 ± 0.10
KR-06-21	1750	0.0826 ± 0.0050	379.65 ± 16.70	68.74 ± 4.29	18.46 ± 1.15	14.00 ± 1.24	0.1144 ± 0.0048	0.0144 ± 0.0008	0.3525 ± 0.0105	9.47 ± 0.28
	900	0.5411 ± 0.0271	1.09 ± 0.22	1.40 ± 0.29	0.38 ± 0.08	6.67 ± 0.96	0.1056 ± 0.0071	0.0030 ± 0.0004	0.0071 ± 0.0024	0.03 ± 0.06
KR-06-29	1750	0.0628 ± 0.0041	5.84 ± 2.27	0.87 ± 0.34	0.23 ± 0.09	12.04 ± 1.00	0.1019 ± 0.0031	0.0029 ± 0.0004	0.0000	0.00
	900	4.2900 ± 0.2147	1.27 ± 0.14	14.46 ± 1.70	3.88 ± 0.46	17.33 ± 1.02	0.1028 ± 0.0009	0.0031 ± 0.0003	0.0048 ± 0.0047	0.13 ± 0.13
Blanks	600	0.0010 ± 0.0003	1.39	0.50 ± 0.20	0.2959	11.67 ± 0.73	0.1027 ± 0.0026	0.0038 ± 0.0002	0.0257 ± 0.0024	0.69 ± 0.06
		0.0010 ± 0.0003	1.39	1.50 ± 0.50	0.1020	0.2959	0.0657	0.0005	0.2196	0.0131
Blanks	900	0.0010 ± 0.0003	1.39	1.20 ± 0.50	0.2959	0.0642	0.0005	0.2352	0.0061	0.1419
		0.0012 ± 0.0004	1.39	2.60 ± 0.80	0.1020	0.2959	0.0954	0.0004	0.2126	0.0108
Blanks	1750	0.0012 ± 0.0004	1.39	2.40 ± 0.80	0.2959	0.0709	0.0015	0.1660	0.0472	0.1450
		0.0012 ± 0.0004	1.39	2.50 ± 0.80	0.1020	0.2959	0.0708	0.0012	0.2134	0.0110
Blanks	Cru- sher	0.0012 ± 0.0004	1.39	1.00 ± 0.40	0.2959	0.0624	0.0026	0.0869	0.1403	0.0635
		0.0013 ± 0.0004	1.39	2.70 ± 1.00	0.1020	0.2959	0.0663	0.0019	0.1459	0.0851
KR-06-25	Cru- sher	0.0080 ± 0.0020	1.39	2.50 ± 0.80	0.2959	0.0687	0.0009	0.1927	0.0349	0.1675
		0.0080 ± 0.0020	1.39	1.90 ± 0.60	0.1020	0.2959	0.0638	0.0003	0.2285	0.0216
KR-06-26	Cru- sher	0.0100 ± 0.0040	1.39	0.90 ± 0.40	0.2959	0.1017	0.0011	0.1963	0.0170	0.1599
		0.0120 ± 0.0040	1.39	1.30 ± 0.40	0.1020	0.2959	0.1000	0.0020	0.1802	0.0375
KR-06-26	Cru- sher	0.0130 ± 0.0040	1.39	1.20 ± 0.40	0.2959	0.0623	0.0020	0.1070	0.0389	0.0980
		0.0160 ± 0.0050	1.39	1.40 ± 0.50	0.1020	0.2959	0.0623	0.0020	0.1070	0.0389
KR-06-25	Cru- sher	0.0226 ± 0.0017	5.80 ± 4.60	16.62 ± 0.91	0.0330	10.2200 ± 0.1500	0.2960 ± 0.0330	0.2960 ± 0.0330	0.2960 ± 0.0330	0.2960 ± 0.0330
		0.0063 ± 0.0010	14.00 ± 31.00/14.00	24.60 ± 1.30	0.0830	0.3010 ± 0.0290	10.2630 ± 0.0830	0.3010 ± 0.0290	0.3010 ± 0.0290	0.3010 ± 0.0290

Table 5.2: Mass-spectrometry results for each temperature step, blank values for the different temperature steps, and ICP-results to constrain nuclide-production rates.

Concentrations of cosmogenic  $^3\text{He}$  derived from these equations differ only slightly, on average 4 % and at maximum 9 %, from the concentrations calculated without considering magmatic  $^3\text{He}$ . Additionally, we argue that in our case the magmatic  $^3\text{He}$  will be overestimated in these equations. Consequently, we use the total  $^3\text{He}$  to calculate surface-exposure ages.  $^3\text{He}$  also originates from the  $^6\text{Li}(n,\alpha)^3\text{H}(\beta)^3\text{He}$  reaction produced by thermalized neutrons from  $(\alpha,n)$  reactions within the rocks (Aldrich and Nier, 1948; Morrison and Pine, 1955; Lal, 1987). Nevertheless, olivines and pyroxenes are Li-poor minerals with Li-concentrations usually below 2 ppm (Brenan et al., 1998; Ryan and Kyle, 2004; Seitz et al., 2004). A test run with a Li-induced  $^3\text{He}$ -production of  $6.13 \cdot 10^{-6}$  at  $\text{g}^{-1} \text{a}^{-1} \cdot \text{ppm}^{-1}$  (Lal, 1987) returns nucleogenic  $^3\text{He}$ -concentrations in the source rocks, which amounts to at maximum 0.06 % of the total  $^3\text{He}$  in the samples including the shielded ones. Li-related production of  $^3\text{He}$  is therefore negligible in our samples. We account for inherited  $^3\text{He}$  and other He-components by subtracting the total  $^3\text{He}$  in the shielded samples from the exposed samples.

$^{21}\text{Ne}$ -concentrations are measured as excess to air. Also, Ne comprises different components such as radiogenic, magmatic, and nucleogenic Ne. Nevertheless, as cosmogenic Ne is characterized by a unique  $^{21}\text{Ne}/^{22}\text{Ne}$ -ratio, it is possible to test, whether the excess  $^{21}\text{Ne}$  is cosmogenic by plotting the measured ratios in a three-isotope systematic (Niedermann et al., 1993; Niedermann et al., 1994). If the excess  $^{21}\text{Ne}$  is cosmogenic, the values plot on the spallation line (Schäfer et al., 1999). Deviations from this line indicate contributions from other components, such as nucleogenic Ne or trapped mantle-Ne. Figure 5.3 shows that within error the  $^{21}\text{Ne}$  in all of our samples, except the KR-06-24, 1750°C, can be considered cosmogenic. In addition,  $^{21}\text{Ne}$ -exposure ages are calculated analogous to the  $^3\text{He}$ -ages by correcting for the inherited and non-cosmogenic Ne-concentrations with the shielded samples.

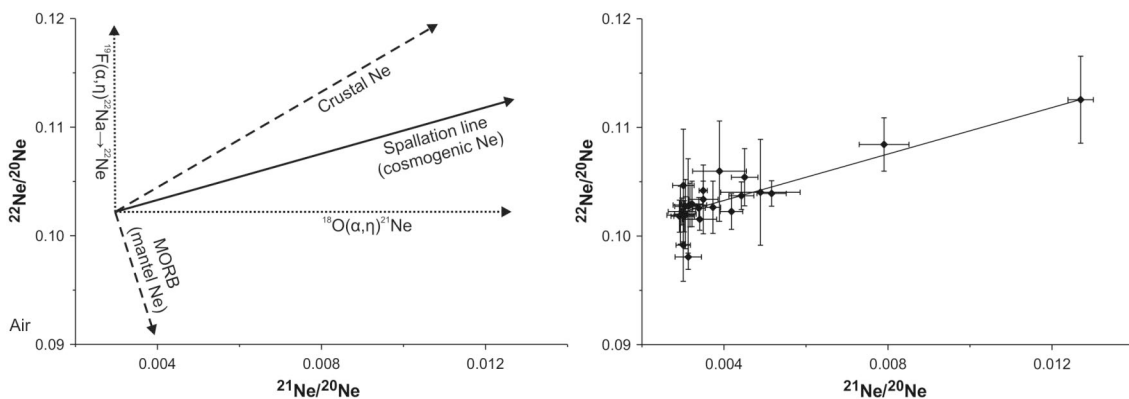


Fig. 5.3: Three-isotope plot for Ne-ratios (Niedermann et al., 1993; Niedermann et al., 1994). The characteristic isotope ratio of cosmogenic Ne determines the location of the spallation line (Schäfer et al., 1999). Note that all except one sample plot within errors on this spallation line documenting that they comprise cosmogenic  $^{21}\text{Ne}$ .

Production rates of  $^3\text{He}$  and  $^{21}\text{Ne}$  are still poorly constrained, since determinations vary up to 30 % (Cerling and Craig, 1994; Licciardi et al., 1999; Dunai and Wijbrans, 2000; Masarik, 2002; Kober et al., 2005). Other factors contributing to a potential age bias, such as temporal variations in the production rate, shielding due to snow or vegetation, and minor erosion, are insignificant compared to the uncertainties introduced by the production rates. We apply production rates of  $116$  at  $\text{g}^{-1} \text{a}^{-1}$  for  $^3\text{He}$  and element-specific production rates for  $^{21}\text{Ne}$  (Table 5.1) (Masarik, 2002). Production rates were scaled to latitude and altitude using the scaling factors of Dunai (2000). Individual depth corrections were applied. Given errors are analytical errors and do not comprise production-rate or scaling uncertainties.

$^3\text{He}$ - and  $^{21}\text{Ne}$ -exposure ages mostly agree well within errors and are both in the range of 150 to 350 ka (Fig. 5.4, Table 5.1). Among the four samples we collected

directly from the surface, three samples display significantly younger ages. However, the nuclide concentrations are similar to the other samples (Table 5.1). The age difference can therefore be explained by lower production rates, implying an originally deeper position of the samples below the surface. In the field, it was impossible to entirely rule out previous agricultural land use. We thus suggest that land use practices may have exposed these samples recently. If we assume an original position of the samples at a depth of 60 cm, the potential reach of a plough, exposure ages of these possibly relocated samples increase and remarkably fit the other ages derived from samples collected at 1 m depth (Table 5.1). Nevertheless, these ages have to be treated with caution. Sample KR-06-24 contains anomalously low nuclide concentrations and is the only sample not located on the Ne-spallation line (Fig. 5.3). The field site does not provide information about sampling bias, we thus discard this sample from our interpretations.

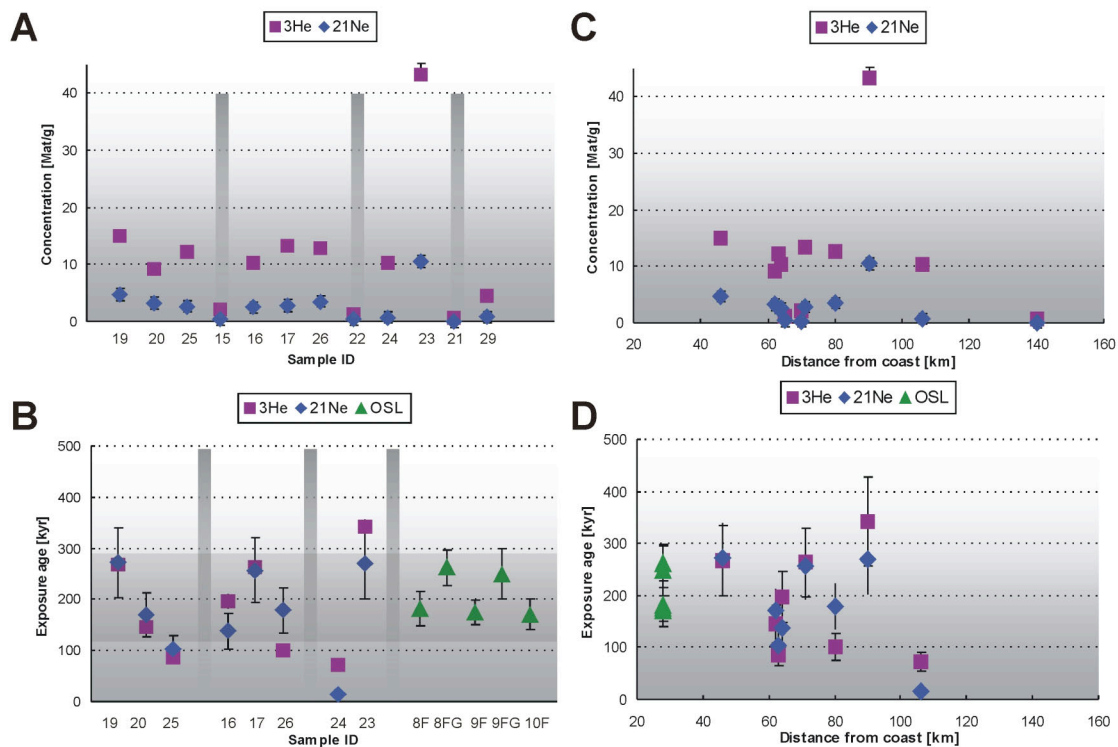


Fig. 5.4: Age distribution of the analyzed samples. A: Concentrations of cosmogenic  $^3\text{He}$  and  $^{21}\text{Ne}$  in  $\text{Mat g}^{-1}$ . The grey bars indicate the shielded samples. Note the low nuclide concentrations in these shielded samples. They are used to correct for inheritance and non-cosmogenic nuclide components. B: Exposure ages derived from  $^3\text{He}$ - and  $^{21}\text{Ne}$ - as well as burial ages derived from OSL-measurements. Grey bars are the same as in A. Note the very good agreement between cosmogenic and OSL-ages. C and D: Cosmogenic-nuclide concentration and exposure ages as a function of the distance from coast. Note that there is no systematic trend suggesting that the surfaces in the Central Depression and the terrace sequences in the Coastal Cordillera developed simultaneously.

### 5.4.2 Luminescence dating

For the post-reversal fluvial deposits derived from basement schist, we calculated three quartz ages of  $83 \pm 9$  ka (KR-06-11),  $74 \pm 8$  ka (KR-06-12) and  $77 \pm 11$  ka (KR-06-13) that are internally perfectly consistent within errors. Beside this internal consistency,

these samples show good luminescence properties, i.e. the OSL signal is dominated by the fast component, thermal transfer and recuperation are absent, the dose recovery is acceptable (Fig. 5.5), there are no indications for partial bleaching (Fig. 5.6). Therefore, we consider these ages very reliable.

In contrast, the results of the K-feldspar and polymineral fine grains for the same samples significantly underestimate the quartz ages by up to  $\sim 50\%$ . A possible explanation for this discrepancy is the often observed anomalous fading of IRSL (Wintle, 1973; Lamothe et al., 2003). In fact, we confirmed this hypothesis by storage tests that reveal a significant loss of IRSL with time. These ages have thus to be considered minimum estimates. Consequently, we use the reliable quartz ages in our interpretation.

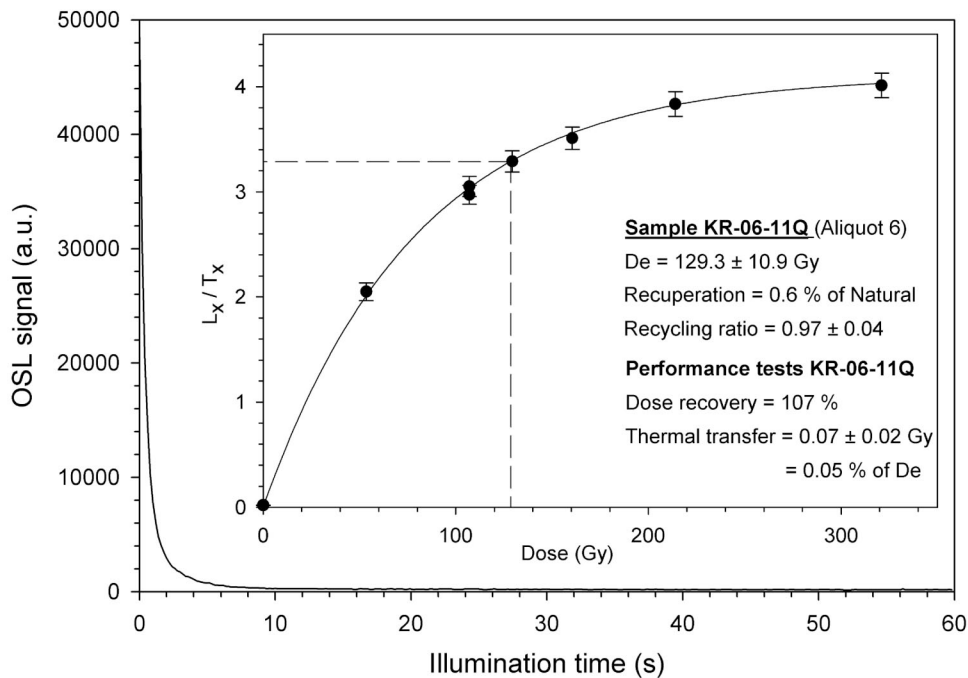


Fig. 5.5: OSL depletion curve of aliquot 6 of sample KR-06-11Q documenting that the signal is dominated by the fast component. The inset plots the dose-response curve for the same aliquot with key data describing the performance of the SAR protocol (Wintle and Murray, 2006).

Recuperation reflects that measurement of a zero dose should give zero signal, however charge transfer from deeper traps due to pre-heating may induce an OSL signal. Murray and Wintle (2000) recommend that recuperation should be  $< 5\%$ . Note that recuperation in our case is 0.6 %.

The recycling ratio reflects the reproducibility of the measurements. The dose 107 Gy has been measured twice, at the beginning and at the end of the SAR cycle. Ideally, the ratio of both measurements would be 1.00, values within 10 % error are considered acceptable (Murray and Wintle, 2000). Note that the dose is reproducible within 0.97 %.

The dose recovery tests, whether a known artificial dose administered to a sample, whose OSL signal has been erased before by light exposure, can be recovered. Ideally, dose recovery would be 100 %. Note that dose recovery is 107 %.

The thermal transfer reflects a similar effect as recuperation, but affects the natural signal only. Note that thermal transfer is negligible for the samples investigated here.

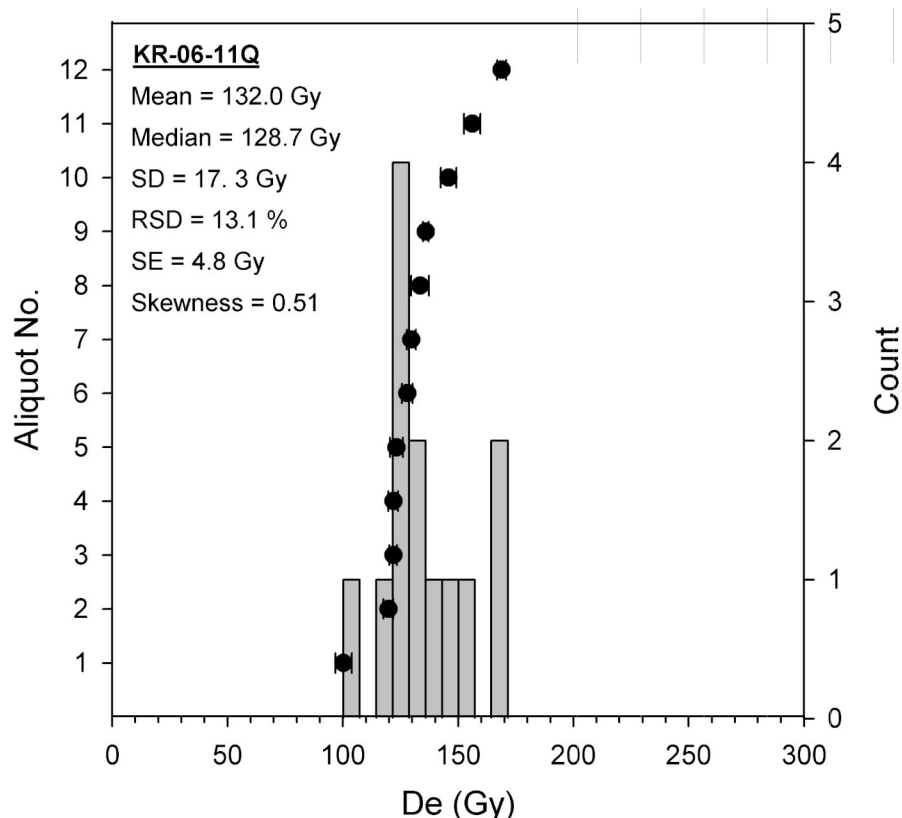


Fig. 5.6: Dose-distribution plot for sample KR-06-11Q with key data documenting the shape of the distribution and frequency-histogram plot. The Gaussian-like shape of the distribution together with the relatively low standard deviation imply complete bleaching of OSL prior to deposition.

SD = Standard deviation; RED = Relative Standard Deviation; SE = Standard Error.

For the pre-reversal deposits derived from arc volcanics, we identified two clusters of ages being internally consistent. It was not possible to separate sufficient amounts of quartz from these samples. However, the sand-fraction K-feldspar clusters around 170 ka, whereas the polymineral fine-grains cluster around 255 ka (Table 5.1). In contrast to the schist-derived grains, we do not observe anomalous fading of IRSL in storage tests in the volcanic grains. Therefore, we favor an alternative explanation for the age difference. The distinct differences in mineral composition of both valley fills were confirmed by the dosimetric measurements, which revealed a much lower concentration of radioactive elements in the pre-reversal deposits. The very low K-content led us to investigate the samples microscopically. In fact, they contain a large number of plagioclase and almost no K-feldspar. Both feldspars differ significantly in their K-content, nevertheless the K-content is an important factor in IRSL dating, specifically with respect to the dose rate. While K-contributions to the dose rate in K-feldspar are fundamental, they are minor for plagioclase. Small percentages of plagioclase are normally negligible in the blue emission spectrum (Krbetschek et al., 1997). However, in our case, considering the near absence of K-feldspar in the samples, the plagioclases are relevant. As a consequence, the assumption of  $12.5 \pm 0.5$  % K overestimates the real K-content in our samples and hence also the average dose rate for the sand-size samples, eventually leading to an underestimation of their ages. In contrast, the contribution from internal K is dispensable in the silt-fraction. Consequently, we argue that the ages derived from the polymineral silt-fraction represent the real depositional age of the sediment.



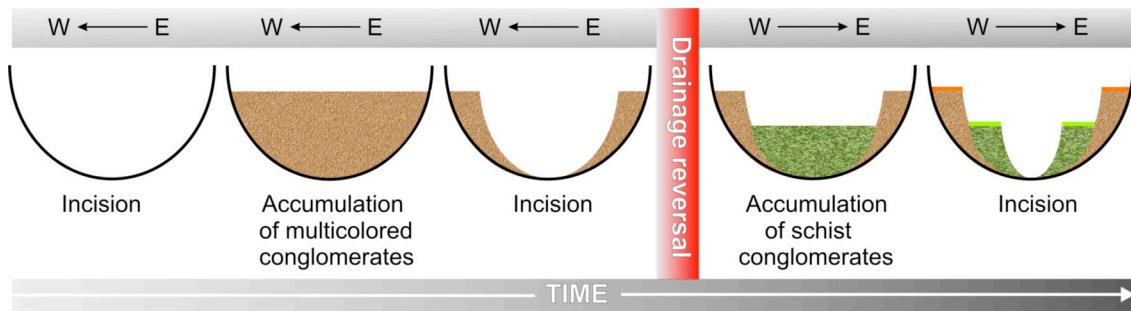


Fig. 5.8: Evolution model of the Pellahuén valley. The upper grey bar marks the flow direction. The figure progresses in time towards the right. The valley evolution comprises different phases of accumulation and incision. As a result, we observe two distinct valley fills and terrace levels along the river

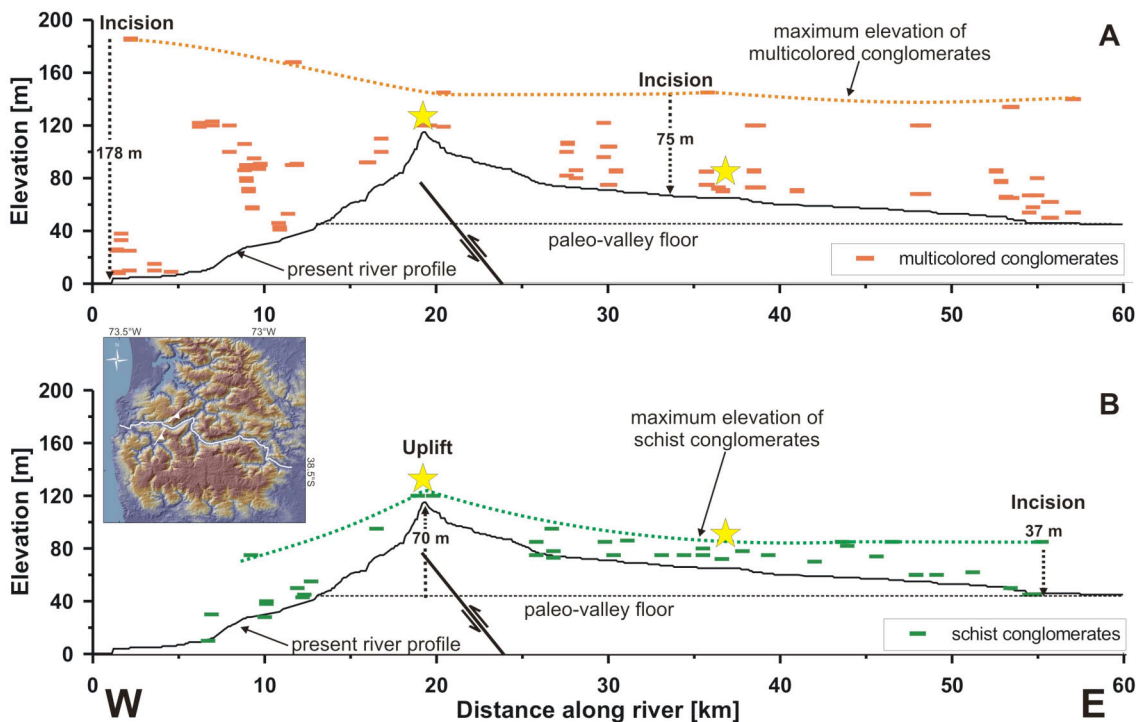


Fig. 5.9: Thalweg profile along the Pellahuén valley. A: Distribution of multicolored conglomerates. Note that they reach maximum elevations of 180 m, but mainly 75 m above present river level. The wind gap is the most elevated part of the profile. The flow reversal is inferred to be controlled by displacement of a blind reverse fault, schematically depicted beneath the wind gap. The paleo-valley floor is the lowest possible valley bottom enabling westward flow of the river. B: Distribution of schist terraces. Note that they reach maximum elevations of 37 m above present river level. The inset outlines the location of the profile with a white line. Yellow stars mark the sample locations.

In the field, we identified two distinct terrace systems along the Pellahuén valley in detail described by Rehak et al. (2008). Figure 5.8 depicts a terrace-evolution model in order to visualize the development of this valley, leading us to propose the following scenario: 4 Ma ago the Coastal Cordillera started to uplift (Rehak et al., submitted). While uplifting, the antecedent Pellahuén river kept up incising. This incision was followed by an aggradational cycle in the Central Depression and the Coastal Cordillera, where up to 180 m of the andesitic and basaltic conglomerates were accumulated within the valley. These pre-reversal valley-fills were incised again, thus creating the upper terrace levels. However, probably the initiation of localized uplift progressively decreased the slope of the river, consequently reducing its stream power.

Finally, incision waned resulting in the tectonic defeat and ultimately the reversal of the river. This stream reversal changed the contributing area completely. Now, the local basement was eroded and another aggradational phase filled the valley with up to 40 m of locally derived schist conglomerates. During continuous uplift these schist units were also incised, creating the lower terrace levels (Fig. 5.8).

Thus, uplift-related drainage reversal took place after the deposition of the upper conglomerates, around 250 to 260 ka ago and prior to the accumulation of the alluvial deposits in the wind gap around 80 ka ago as indicated by OSL ages. Consequently, the incision of these conglomerates and the flow reversal in the Coastal Cordillera occurred between 255 and 80 ka (175 ka). The conglomerates must have been completely eroded prior to the reversal since they were evacuated from the wind gap as well. The andesitic-basaltic conglomerates in the Pellahuén valley can be mapped from 8 to 186 m above sea level (asl) (Fig. 5.9). However, they are mostly abundant between 70 and 145 m asl along the river (Fig. 5.9). The contact between the upper and lower terrace sediments is located 2 m above the present-day river level (arl). This documents that during maximal 175 ka on average 75 m, locally up to 178 m, of former conglomerate fill was evacuated, implying pre-reversal minimum incision rates of 0.43, and locally 1.02 mm a<sup>-1</sup> (Table 5.3). The same calculation can be conducted for the post-reversal sediments. The schist conglomerates can be mapped up to 37 m arl reflecting post-reversal incision of at least 37 m since 80 to 255 ka. Consequently, post-reversal incision rates range between 0.15 and 0.46 mm a<sup>-1</sup>.

	Elevation difference [m]	Elapsed time [ka]	Incision/Uplift rate [mm a <sup>-1</sup> ]
Prereversal incision			
min	75	175	<b>0.43</b>
	178	175	1.02
Postreversal incision			
min	37	255	0.15
max	37	80	<b>0.46</b>
Postreversal uplift			
min	70	255	0.27
max	70	80	<b>0.88</b>

Table 5.3: Incision and uplift rates in the Pellahuén valley. Bold numbers mark incision and uplift rates when the flow reversal occurred 80 ka ago (see text for discussion).

Additionally, we decipher local uplift rates by reconstructing the paleo-valley floor beneath the wind gap (Fig. 5.9). Prior to the reversal the river drained into the Pacific, which could only have been possible when the valley bottom did not exceed an elevation of 45 m asl. At present, the valley floor is located at an elevation of 115 m asl. These 70 m of uplift occurred at maximum after 255 ka and at minimum after 80 ka, resulting in local uplift rates of 0.27 and 0.88 mm a<sup>-1</sup>, respectively (Table 5.3). The incision- and uplift-rate ranges are conservative estimates. However, as indicated by the low-energy deposits in the wind gap and due to the fact that the multicolored conglomerates must have been evacuated prior to the reversal, we suggest that the river was probably defeated close to 80 ka. Consequently, pre-reversal incision rates, post-reversal incision rates, and post-reversal uplift rates are most likely represented by the endmembers 0.43 mm a<sup>-1</sup>, 0.46 mm a<sup>-1</sup>, and 0.88 mm a<sup>-1</sup>, respectively (Table 5.3). Interestingly, whereas incision rates are slower than our inferred post-reversal uplift rate, both incision and short-term uplift rates are significantly higher than long-term surface uplift and exhumation rates, which were shown to average around 0.2 mm a<sup>-1</sup> for the last 5 Ma (Glodny et al., 2007; Rehak et al., submitted). The spatial restriction of uplift, the geometry of the uplifted valley, and the morphology of the adjacent ridges suggest that local deformation is controlled by a blind thrust and reverse faulting (Figure 5.9). Uplift might thus be mainly accommodated by displacement along faults. A regional extrapolation inferring accelerated uplift from our observed increased uplift rates may thus be suggested. Moreover, an acceleration of

uplift during latest Pleistocene times is congruent with other datasets in the region (Kaizuka et al., 1973; Nelson and Manley, 1992; Bookhagen et al., 2006a; Melnick et al., 2006; Melnick and Echtler, 2006a). Such crustal-scale faults control the distribution of low-wavelength surface features by folding the upper crust between and probably also during interplate events. Consequently, we conclude that (1) subduction-zone interplate earthquakes and upper-plate faults, which individually accommodate low magnitudes of shortening, determine the degree and spatial extent of surface deformation and uplift (Melnick et al., 2006); (2) deformation of the forearc is transient; and (3) uplift rates vary significantly in time and space.

	Production rate at 300 cm depth [at/g/a]	Production rate at surface [at/g/a]	Nuclide concentration [at/g]	Deposition in river bed [a]	Post-burial concentration [at/g]	Pre-burial concentration [at/g]	Storage at surface [a]
KR-06-29	<b><sup>3</sup>He</b>						
	6.62	100.39	4.55E+06	2.56E+05	1.70E+06	2.85E+06	2.84E+04
	<b><sup>21</sup>Ne</b>						
	1.53	23.23	8.18E+05	2.56E+05	3.92E+05	4.26E+05	1.83E+04

Table 5.4: Temporal sediment storage in the Central Depression. We calculated the postburial production based on the present location and the depositional ages derived by OSL dating. Storage times are minimum estimates since we assume storage at the surface where production rate is highest.

In a next step, we will explore the influence of climate on sediment accumulation in the Coastal Cordillera and the Central Depression as well as the relation between both depositional settings. The depositional surfaces in the Central Depression have ages between 146 and 341 ka. These ages are consistent with the age of the valley fills in the Coastal Cordillera. Nevertheless, it is not possible to decide yet, whether the deposition in the Coastal Cordillera and the Central Depression occurred coevally, since the resolution of these dates might mask a lag time between two potential accumulation events. Hence, we measured <sup>3</sup>He- and <sup>21</sup>Ne-concentrations also in the fluvial conglomerates in the Coastal Cordillera in order to compare both sedimentary units. If the conglomerates are directly derived from the Main Cordillera and have been transported without transient storage directly to their current position within the valley in the Coastal Cordillera, we would expect extremely low nuclide concentrations that would approximate the concentrations in the shielded-samples. In fact, in the test sample KR-06-29 we measure significantly lower concentrations than in all other samples. However, the concentrations are still about twice as high as the shielded-sample concentrations. This suggests that these conglomerates had been stored at or near the surface prior to their final deposition. Consequently, we calculated the post-burial production, i.e. the concentration accumulated after final deposition. Subtracting this concentration from the total cosmogenic-nuclide inventory of the sample, we can provide an estimate of how long the samples must have been temporarily stored prior to their re-deposition. Assuming a surficial position, we derive storage times of 20 (<sup>21</sup>Ne) to 30 (<sup>3</sup>He) ka (Table 5.4). Since the boulders might have been stored below the surface, these storage times are minimum estimates. Based on these considerations, we argue that the fluvial conglomerates in the Coastal Cordillera are indeed remobilized sediments originating from the recycling of the alluvial deposits in the Central Depression. Conclusively, our study area experienced alternating phases of sediment accumulation and evacuation.

Finally, we strive to test the relation between climate and sediment accumulation. Therefore, we superpose the depositional ages on a sea level curve (Fig. 5.10). This shows that with one exception all accumulation events correspond to sea-level minima, i.e. glacial periods. This is supported by the fact that identical conglomerate units are located on the strongly uplifted island Mocha, ~ 30 km off the coast (Echtler, 2008). Present water depth between the coast and the island reaches

some tens of meters implying that these sediments were deposited during a sea-level low stand, hence during a glacial period. However, sediment deposition can be related either to a reduction of transport capacity, or an increase in sediment input. The base-level fall during glacials is expected to increase channel slope and thereby transport capacity, and should thus promote incision and material transport towards the trench. Consequently, the extensive sediment accumulation in the forearc was probably controlled by a significant increase in sediment flux. Such an increase in sediment flux related to glacial periods is commonly observed when the glaciers retreat and expose eroded material. We hence propose that (1) the accumulation events in the south-central Chile forearc are related to cessation of glacials and (2) the surfaces in the Central Depression constitute large glacial outwash fans similar to the southern “Patagonian gravels” as proposed by Mercer (1976).

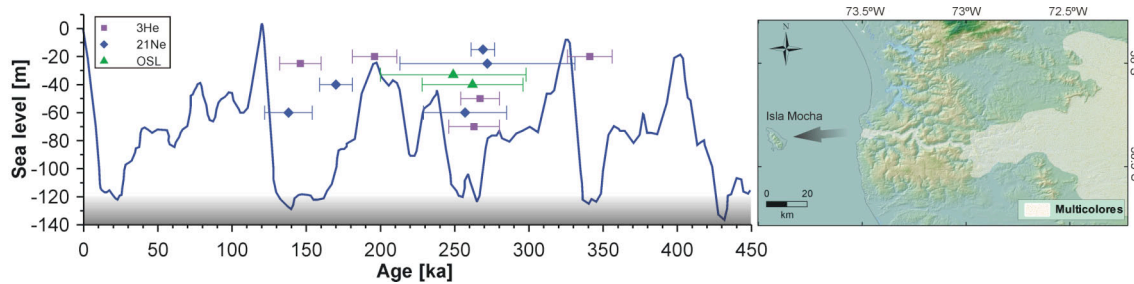


Fig. 5.10: Correlation of sediment accumulation and sea level. Note that most of the sample plot in glacial periods with low sea level. The transport and accumulation during glacials is supported by the occurrence of identical conglomerate units on Mocha Island whose location require a subaerial shelf and thus a low sea level during transport and accumulation. Consequently, incision appears to preferably occur during interglacial stages.

## 5.6 Conclusions

We explored the late Pleistocene landscape evolution of the south-central Chile forearc by dating fluvial valley fills and depositional surfaces in the Coastal Cordillera and the Central Depression, respectively. The data presented here documents that the surfaces in the Central Depression were deposited 150 to 350 ka ago probably related to Pleistocene glacial cessations. The multicolored conglomerates within the valley of the reversed Pellahuén river constitute remobilized sediments, originally derived from the Main Cordillera, but temporarily stored in the large fans in the Central Depression.

The late Pleistocene geomorphic evolution of the Pellahuén valley comprises at least two phases, which are recorded in the sediments accumulated along the river. Prior to 80 ka the river drained into the Pacific constituting a major transport channel for arc-derived material. However, progressive uplift with on average  $0.88 \text{ mm a}^{-1}$ , probably related to displacement along a blind thrust, eventually defeated the river. Incision rates both prior and after the reversal approximate  $0.45 \text{ mm a}^{-1}$  and are thus slower than short-term uplift, but faster than long-term uplift rates. In fact, a comparison between long-term and short-term uplift rates indicates that uplift of this segment of the Chile forearc is accelerating during the late Pleistocene. This is in agreement with other studies from this region.

Conclusively, sediment accumulation in this forearc appears to be primarily controlled by climate. Thus, while tectonics have always played an important role in the evolution of this margin, climatic forcing has left a major imprint on the morphology of the landscape.

### **Acknowledgements**

This work was funded by Deutsche Forschungsgemeinschaft through the Leibniz Award to Manfred Strecker (STR373-18-1), the A. Cox fund of Stanford University, and supported by the GeoForschungsZentrum Potsdam. We appreciate discussions with Maria Mardones, Tim Vietor, Bodo Bookhagen as well as Daniel Melnick, and thank Enzio Schnabel for technical support.

## 6. Climatic controls on drainage-basin morphology – the western Andean flank between 15.5° and 41.5°S

### Abstract

*Mountain-range topography in tectonically active regions is determined by the complex interplay between tectonics, climate, and erosion. However, it is still controversially discussed how topography is influenced by climate.*

*The Andes provide a unique natural setting for investigating the relationship between climate and topographic evolution. The meridionally oriented, tectonically active mountain belt encompasses various climatic zones with pronounced differences in rainfall and geomorphic processes under fairly identical plate-boundary conditions. In the Central to Southern Western Andes, climatic zones range from hyperarid in and around the Atacama Desert at 22 to 23°S with mean annual rainfall of  $\sim 5 \text{ mm a}^{-1}$  to year-round humid conditions south of Valdivia at  $\sim 40^\circ\text{S}$ , with  $> 2500 \text{ mm a}^{-1}$ . This zonation is controlled by long-lived hemisphere-scale atmospheric circulation patterns.*

*Here, we present an analysis of 120 drainage basins along the watershed of the western Andean flank between 15.5° and 41.5°S. For our study, we used SRTMV3-90m topographic data as well as a 10-year remotely sensed rainfall dataset with a spatial resolution of 30 x 30 km. The basins comprise drainage areas of 1 to  $\sim 30 \cdot 10^3 \text{ km}^2$  split into different subsets according to position and size. For each basin, we extracted a variety of geometry, relief, and climate parameters in order to unravel the factors determining drainage-basin morphology.*

*We distinguish two different, climatically-controlled mechanisms shaping topography: moderate rainfall promoting diffusion processes which smooth relief and glacial erosion that generates relief. Our data show that river profile concavity, basin maximum elevation, and basin mean elevation decrease with increasing rainfall and descending snowline. Interestingly, our results document that local relief (calculated over a 4.5-km-radius) reaches maximum values of  $\sim 750 \text{ m}$  in a broad zone between 28° to 35°S. During glacial stages this region was affected by the northward shift of the Westerlies, providing moisture for valley-glacier formation. Relief generation in this transition zone appears thus to be related to Pleistocene glaciations. Apparently, the interaction between sparse, highly episodic rainfall and protracted periods of aridity facilitates relief preservation in regions where material can be quickly transported out of the orogen and does not accumulate in intramontane basins. In contrast, the southern regions between 35° to 40°S receiving higher rainfall show a lower local relief of  $\sim 200 \text{ m}$ . This might be controlled by more efficient fluvial erosion and diffusive hillslope processes above a rainfall threshold of  $\sim 800 \text{ mm a}^{-1}$  due to a higher drainage density. Ultimately, our data suggests that the catchment-scale relief of the Andes reflects a pronounced transient component recording past and present climatic conditions. This implies that due care has to be exercised when interpreting landscapes as mirrors of modern climates.*

**KEYWORDS:** drainage basins, topography, morphometry, climate, erosion

## 6.1 Introduction

Landscapes are sensitive recorders of climatic boundary conditions. They can thus provide important insights in the complex interaction between climate, surface processes, and topography. It has been proposed that climate plays a major role in creating relief and shaping topography due to erosion (Molnar and England, 1990). However, climate-change induced relief production has been challenged, arguing that active mountain belts are already characterized by threshold relief (Whipple et al., 1999; Montgomery and Brandon, 2002). Additionally, previous studies have shown that the distribution of glaciers in a mountain range limits range height by concentrating erosion near the peaks, on the other hand, glaciers enhance local relief by creating steep topography at and above the equilibrium-line altitude (ELA) (Brozovic et al., 1997; Whipple et al., 1999; Montgomery et al., 2001; Tomkin and Braun, 2002; Mitchell and Montgomery, 2006). Furthermore, modeling studies suggest that increased precipitation might cause a reduction of mountain-range topography and strongly influence drainage-basin morphology as well as river profile concavity (Tucker and Slingerland, 1997; Whipple and Tucker, 1999; Roe et al., 2002; Roe et al., 2003). These inferred feedbacks are generally corroborated by field studies (Montgomery et al., 2001; Gabet et al., 2004). However, these different issues and controversies emphasize that fundamental key questions concerning the interactions between topography and climate have not been fully answered yet. In this context, it is extremely important to investigate the influence of climate on mountain-range topography as the link between tectonics and climate with data collected from real orogens. Such studies are still scarce and often suffer from low spatial and temporal resolution.

Collecting and interpreting empirical data on morphology and its relation with climate is hindered by three major problems. First, it is often difficult to distinguish between climatic and tectonic influences on morphology. For example, a fluvial channel could adjust both to an increase in precipitation and a decrease in uplift rate by reducing channel slope. Second, landscapes might reflect past climate regimes impeding the correlation of present morphology with prevailing climatic conditions. However, if identified, these landscapes provide the chance to reconstruct paleo-climatic forcing. A third problem is that an ideal setting to analyze links between climate and topography has to provide large gradients in climatic parameters, but possibly homogeneity in all other dependent variables as lithology, uplift rate etc., which is virtually impossible to find in natural systems. However, an alternative starting point could constitute a setting where climatic parameters display significant gradients and systematic variation, whereas other variables vary unsystematically. Ideally, one would thus have to choose a geodynamic and climatic setting where the overall characteristics of the climatic conditions have been sustained over long time scales in a well constrained tectonic system. The sustenance of climatic patterns is important in order to maximize the probability to examine a climate-adapted landscape. These requirements are reasonably well fulfilled along the west coast of South America.

Indeed, the Andes provide a unique setting for investigating the relationship between climate and topography. More than 7000 km long, the Andes are a meridionally oriented, tectonically active orogen spanning large gradients of various climatic zones and rainfall regimes from hyperarid to humid, controlled by stable, hemisphere-scale atmospheric circulation patterns that persisted at least during Quaternary and possibly over the Neogene (Weischet, 1970; Schwerdtfeger, 1976; Bice et al., 2000; Haselton et al., 2002). Lithology varies non-systematically along this margin and does not correlate with climatic parameters. Data on surface-uplift rates in the Main Cordillera is extremely sparse, thus, we have to use proxy indicators such as

surface-uplift data from the forearc, the intensity of active deformation, and trench-normal shortening.

Based on a medium-resolution TRMM (Tropical Rainfall Measurement Mission) dataset, we conducted a detailed analysis of the western Andean flank between 15.5°S and 41.5°S extracting 19 geometry, relief, and climate parameters for 120 drainage basins. This enables us to characterize and better understand the climatic controls of relief generation in mountain ranges, especially with regard to transience in landscapes and the role of rainfall on relief evolution.

## 6.2 Regional setting

### 6.2.1 Geologic setting

The Andean margin is characterized by the subduction of the Nazca plate beneath the South American continent at a rate of approximately 65 to 85 mm a<sup>-1</sup> (Demets et al., 1994; Somoza, 1998; Angermann et al., 1999). The pre-Andean basement evolved during a period of already east-directed subduction. The basement is subdivided into crustal segments comprising exotic terranes, the Precordillera Terrane, as well as late Paleozoic to early Mesozoic igneous and metamorphic rocks, batholiths, and accreted marine sequences that constitute arc-forearc complexes (Hervé, 1988; Mpodozis and Ramos, 1989; Parada, 1990; Hervé et al., 2007; Pankhurst and Hervé, 2007). This basement was strongly overprinted by subduction-related tectonic and magmatic processes operating since the Jurassic period (Mpodozis and Ramos, 1989; Allmendinger et al., 1997).

The recent phase of contraction and shortening that initiated the uplift of the Andean mountain range and was accompanied by extensive arc activity starting in Eocene in the Central Andes and propagating southwards where it reached the Northern Patagonian Andes in early Miocene (Allmendinger et al., 1990; Jordan, 1993; Kley and Monaldi, 1998; Oncken et al., 2006). Total shortening decreases southward from ~ 300 km in the Central Andes to only ~ 15 km in the Northern Patagonian Andes (Isacks, 1988; Allmendinger et al., 1990; Diraison et al., 1998; Kley et al., 1999; Gregory-Wodzicki, 2000; Oncken et al., 2006; Vietor and Echtler, 2006) (Fig. 6.1). GPS measurements corroborate this pattern and document higher shortening rates in the Central Andes (Dewey and Lamb, 1992; Klotz et al., 2001; Brooks et al., 2003). Based on shortening rates and tectonic activity, the Central to Southern Andes can be differentiated into four tectonic provinces (Fig. 6.1). (1) The central part from 14° to 27°S comprises the Coastal Cordillera, the Central Depression, the Precordillera and the Main Cordillera with the internally drained intra-orogenic plateaus of the Altiplano and Puna encompassing mean elevations of 4000 m. This sector displays pronounced crustal shortening in the Main Cordillera and the Subandean Ranges (Mpodozis and Ramos, 1989). (2) The region between 27° and 33°S is characterized by flat-slab subduction and a related absence of Quaternary volcanism and the Central Depression (Jordan et al., 1983; Mpodozis and Ramos, 1989; Kay and Mpodozis, 2002; Ramos et al., 2002). However, this region comprises the broken foreland of the Sierras Pampeanas that experiences active deformation and destructive earthquakes (Jordan and Allmendinger, 1986; Allmendinger et al., 1990). (3) Starting at 31°S, total shortening is significantly reduced implicating thick-skinned eastern foreland deformation (Vietor and Echtler, 2006). South of 33°S the western on-shore active margin shows a pronounced morphotectonic segmentation integrating the forearc

Coastal Cordillera, the Central Depression, and the Main Cordillera (Muñoz et al., 2000). (4) South of  $\sim 38^{\circ}\text{S}$  the Main Cordillera is called Patagonian Cordillera. Here, deformation is dominated by strain partitioning and intra-arc strike-slip tectonics along the Liquine-Ofqui fault zone (Cembrano et al., 2000; Thomson, 2002; Rosenau et al., 2006).

Surface-uplift rates in the Main Cordillera are poorly constrained and only few discrete data points are available (Fig. 6.1) (Farias et al., 2005; Charrier et al., 2007; Schildgen et al., 2007). Nevertheless, they are in very good agreement with Neogene uplift rates derived in the forearc along the coast that vary between  $0.2$  and  $2 \text{ mm a}^{-1}$  and are relatively constant along the margin, except a patch of faster uplift in the region around the Arauco peninsula at  $\sim 37^{\circ}\text{S}$ , possibly controlled by local high-angle reverse faults (Fig. 6.1) (Kaizuka et al., 1973; Radtke, 1989; Atwater et al., 1992; Nelson and Manley, 1992; Ortlieb et al., 1996a; Ortlieb et al., 1996b; Marquardt et al., 2004; Le Roux et al., 2005; Melnick et al., 2005; Pino and Navarro, 2005; Bookhagen et al., 2006a; Le Roux et al., 2006).

### 6.2.2 Climatic setting

From  $15^{\circ}$  to  $42^{\circ}\text{S}$  the western flank of the Andes spans various climatic zones and rainfall regimes from the hyperarid subtropical Atacama Desert with 12 months of aridity in the north and semiarid environments with few months of winter rain in the central part, to year-round humid regions in the south (Fig. 6.1). Mean annual precipitation increases from virtually zero in the core of the Atacama desert at  $22^{\circ}\text{S}$  to about  $3500 \text{ mm a}^{-1}$  on the windward side of the Andes at  $41^{\circ}\text{S}$  (e.g. Kummerow et al., 2000; New et al., 2002; TRMM, 2007; Bookhagen and Strecker, 2008). In the north the prevailing humid trade winds from the east and the low-level Andean Jet from the northeast are blocked by the Andean topography, which together with the upwelling cold water of the Humboldt Current promotes hyperaridity on the western flanks in the north (Weischet, 1970; Schwerdtfeger, 1976). In contrast, the Westerlies directly deliver moisture to the western flanks south of  $\sim 30^{\circ}\text{S}$ . The equator-near position of the Pacific anticyclone enables these frontal systems from the west to penetrate northwards and carry moisture as far north as  $30^{\circ}\text{S}$ , occasionally during mid-winter even up to  $27^{\circ}\text{S}$  into the arid regions (Schwerdtfeger, 1976). Between  $27^{\circ}$  and  $30^{\circ}\text{S}$  this frontal rain occurs between May and August accounting for 90 % of the total annual rainfall with each month's precipitation normally originating from only one frontal passage (Weischet, 1970; Schwerdtfeger, 1976). The largest precipitation gradient occurs between  $30^{\circ}$  and  $35^{\circ}\text{S}$ , where precipitation rates increase by one order of magnitude from  $300$  to  $3000 \text{ mm a}^{-1}$ .

Superposed on annual periodic rainfall variation, the region around  $28^{\circ}\text{S}$  is subjected to episodic variations from arid to subhumid climate due to increased moisture transport from the south controlled by a northward shift of the Southern Westerlies during glacial periods (e.g. Scholl et al., 1970; Heusser, 1989; Clapperton, 1993; Veit, 1996; Lamy et al., 1998; Lamy et al., 2000; Jenny et al., 2002; Romero et al., 2006; Hebbeln et al., 2007).

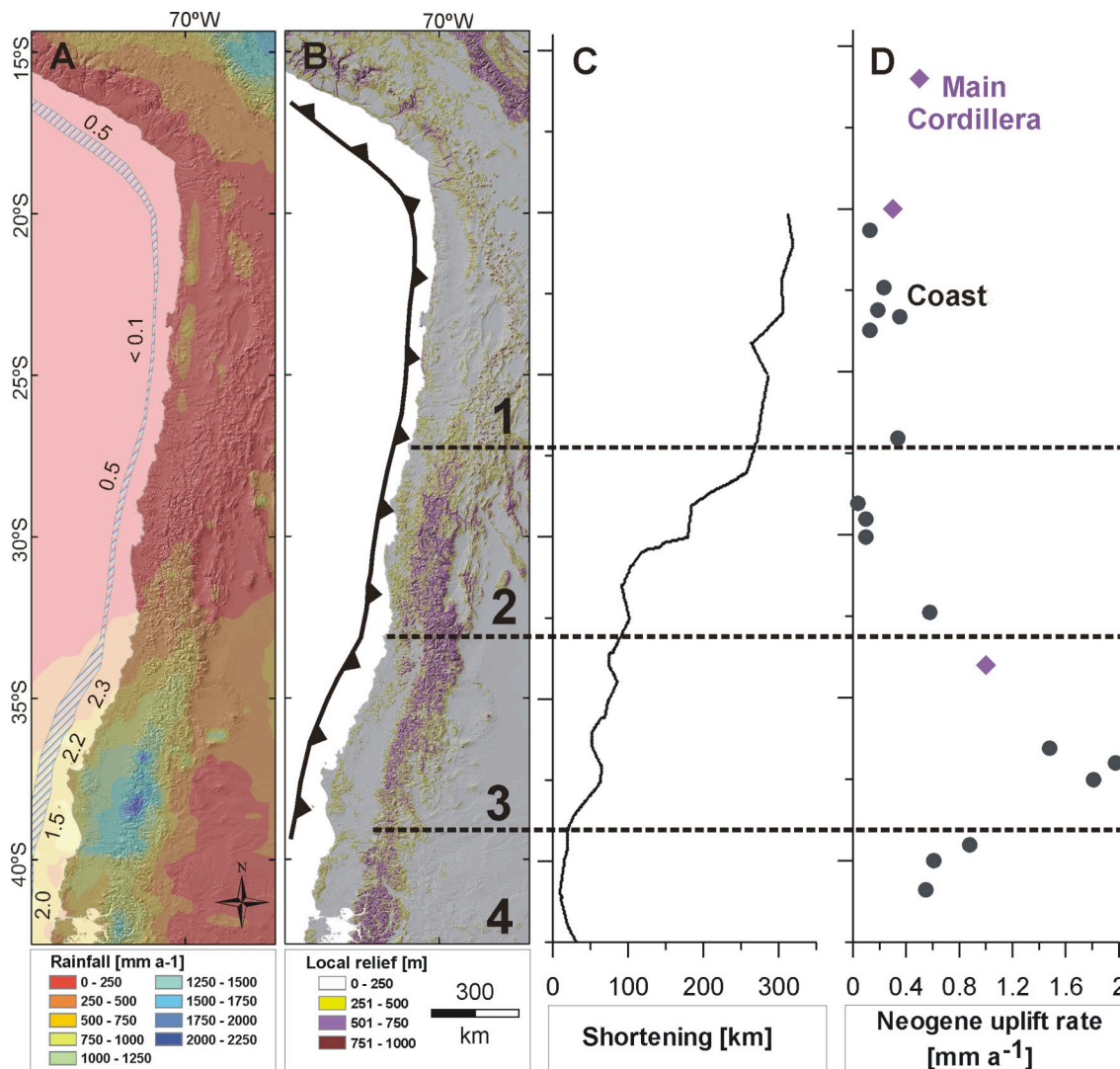


Fig. 6.1: (A): Analyzed drainage basins with TRMM-rainfall data (TRMM, 2007). Numbers indicate trench-fill thickness (Bangs and Cande, 1997). Note the rainfall increase south of ~32°S and the rainfall maximum between 35° to 40°S. (B): Local relief map calculated over a radius of 4.5 km with tectonic segments (Mpodozis and Ramos, 1989). Segment 1 exhibits high crustal shortening comprising the plateau regions. Segment 2 is a flat-slab segment with active deformation in the Main Cordillera, but no Quaternary volcanism. Segment 3 is characterized by low shortening and minimal foreland deformation, however, high uplift rates in the forearc. Segment 4 also shows low shortening and the deformation inheres a dominant strike-slip component. Note the high relief areas between 30° to 35°S and south of 40°S as well as the coincidence of the maximum rainfall and the lower local relief between 35° to 40°S. (C): Total shortening along the south-central Andean margin (Viator and Echtler, 2006). See the decrease in shortening at ~29°S. (D): Neogene uplift rates mostly derived from the forearc region (Kaizuka et al., 1973; Radtke, 1989; Atwater et al., 1992; Nelson and Manley, 1992; Ortlieb et al., 1996a; Ortlieb et al., 1996b; Marquardt et al., 2004; Le Roux et al., 2005; Melnick et al., 2005; Pino and Navarro, 2005; Bookhagen et al., 2006a; Le Roux et al., 2006) and from the Main Cordillera (Farias et al., 2005; Charrier et al., 2007; Schildgen et al., 2007).

Less extensive shifts of the Westerlies have occurred on shorter timescales, i.e. in Holocene (Lamy et al., 1999). Contrasting, precipitation pattern of the plateau regions north of 27°S appear to be relatively stable over glacial-interglacial cycles (Garreaud et al., 2003). Taken together, these present-day and past conditions define a broad climatic and geomorphic transition zone between 28° to 35°S characterized by annual and glacial-interglacial rainfall variations.

The climatic zonation of the study area is controlled by long-lived, hemisphere-scale circulation patterns. The hyperarid conditions in the Atacama Desert were established at least 10 to 15 Ma ago leading to extremely low geomorphic process rates (Hartley, 2003; Dunai et al., 2005; Nishiizumi et al., 2005; Rech et al., 2006). The general circulation in the southern Central Andes has persisted during Pleistocene, but may have been established in the middle Miocene implying that the humid conditions in the south have been stable and controlled by the Southern Westerlies over a very long time span (Schwerdtfeger, 1976; Bice et al., 2000; Haselton et al., 2002; Blisniuk et al., 2005). This is supported by the fact that the distribution of precipitation is mimicked by the thickness of sediment fill in the trench off South America, documenting a significant increase of sediment thickness south of the Juan-Fernández Ridge and supporting the long-term stability of the general precipitation pattern along the western Andean margin (Bangs and Cande, 1997; Melnick and Echtler, 2006a) (Fig. 6.1). Due to the longevity of this zonation, we infer that topography, relief, and drainage are adapted to climate.

South of 41°S drainage basins are not integrated and frequently change size due to glacial erosion of ice caps (Mardones, 2006). Consequently, these basins were not included in our analysis. Between about 18°S and 28°S no recent glaciers exist, the elevation of the modern perennial snowline as well as the lowest Pleistocene glacier extent lie well above 5000 m and exceed the maximum elevation of drainage basins (Rabassa and Clapperton, 1990; Ammann et al., 2001). Hence, these catchments are not influenced by Quaternary glaciations.

### 6.3 Methodology

Along the western Andean flank from 15.5°S near Arequipa (Peru) to 41.5°S to Chiloé Island (Chile) we extracted a total of 120 drainage basins, comprising 64 main catchments draining into the Pacific, and 56 equally-sized subcatchments along the divide, running common ArcInfo and RiverTools routines. The initiation of a channel was determined by a rainfall-related threshold value. Extracted channels were compared with the blue lines of 1 : 250,000 topographic maps. According to their location the main catchments were grouped in forearc, mountain front, and arc sectors (Fig. 6.2). Forearc catchments drain only the Coastal Cordillera, whereas mountain-front catchments also include the Central Depression and the Andean foothills, nevertheless they do not reach the high Andes. Arc catchments extend from the Pacific up to the principal Andean watershed. Subcatchments are parts of the arc catchments and constituting the uppermost headwater basins along the Andean main drainage divide. All subcatchments were extracted based on a similar contributing area of ~ 500 to 2000 km<sup>2</sup> in order to identify and exclude orographic and scale effects. For each basin and its trunk stream we calculated 19 variables describing geometry, relief, and climate. Our analysis is based on the medium-resolution rainfall dataset TRMM and topographic SRTM3-90-m data.

A selection of calculated parameters is described in Table 6.1. A complete list is attached in Appendix A. All variables were correlated in order to identify relationships between basin geometry, range relief, climate, river-profile concavity and hypsometric integral. Total basin relief is calculated as the difference between the absolute maximum and minimum elevation of a catchment (Fig. 6.2). In contrast, local relief describes the range of relief in circles with a radius of 5 cells, 4.5 km, averaged for each basin (Fig. 6.2). Modern annual snowline and lowest Pleistocene glacier extent are compiled from Schwerdtfeger (1976) and Rabassa & Clapperton (1990).

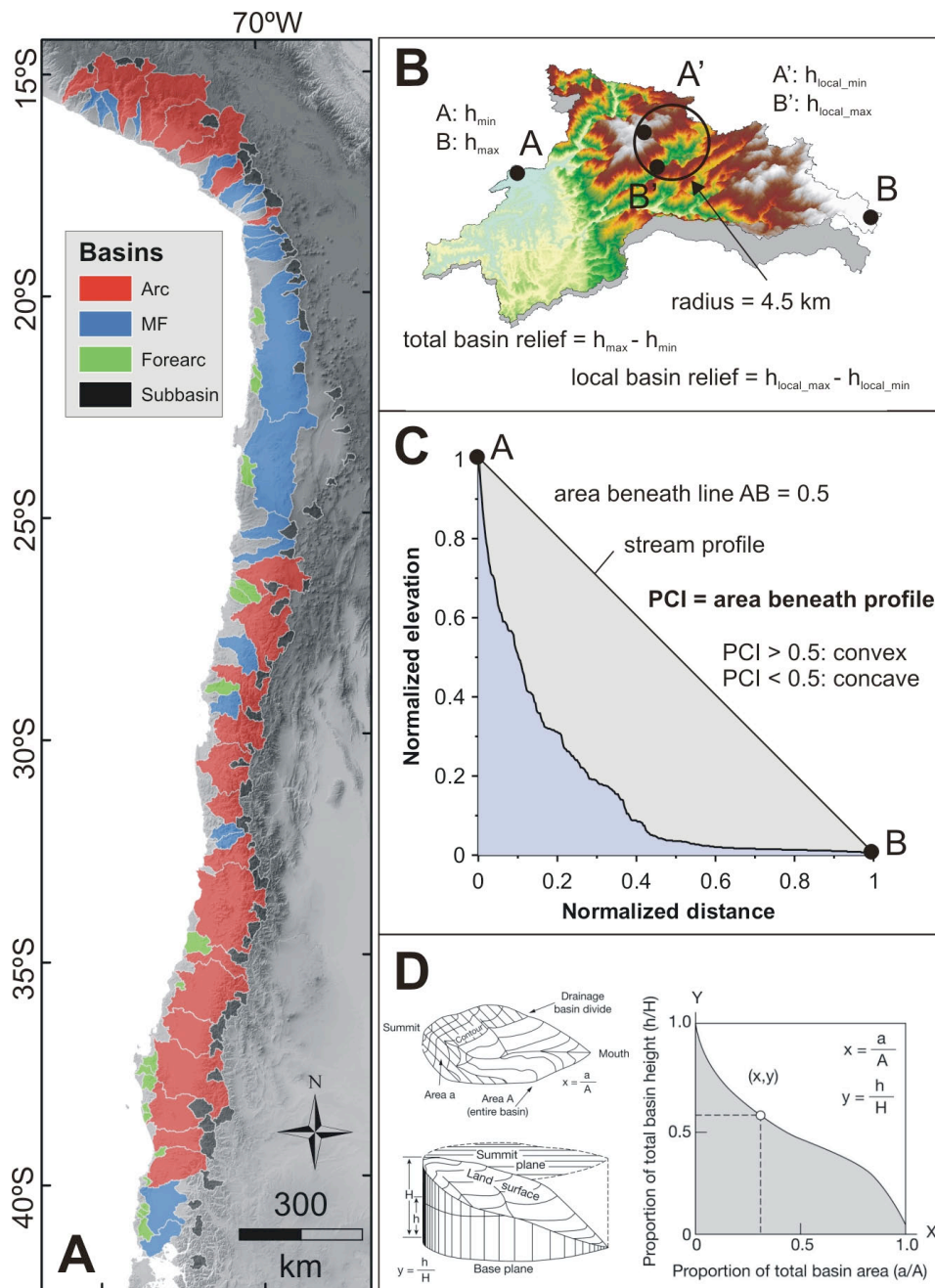


Fig. 6.2: (A): Analyzed basins along the Andean margin. Arc catchments reach from the Pacific Ocean up to the main drainage divide, mountain-front catchments reach the Andean foothills. Forearc catchments drain only the Coastal Ranges. Subcatchments are mostly part of the arc catchments and constitute headwater basins along the watershed. (B): Sample catchment demonstrating the calculation of total and local basin relief. (C): The PCI is an integral describing the area beneath a river-longitudinal profile. (D): Generation of the hypsometric curve and the related hypsometric integral defined as the area beneath the curve.

River profiles are often interpreted with respect to climatic conditions, fluvial processes, rock-uplift rates, and evolutionary stage (e.g. Strahler, 1952; Summerfield, 1991; Ohmori, 1993; Whipple and Tucker, 1999; Snyder et al., 2000; Kirby and Whipple, 2001). The concavity of a river-profile can be expressed as a profile concavity index (PCI) (e.g. Demoulin, 1998). This reduces the river profile to a single number and enables correlation with other variables. The PCI is calculated as the normalized area under the normalized distance-elevation curve of the river (Fig. 6.2). A diagonal drawn from the source to the mouth would result in a value of 0.5; thus, profiles with a

PCI > 0.5 reflect convex shapes. The PCI is similar to stream-profile concavity used by Zaprowski et al. (2005), who found that this index covaries with the stream-profile concavity  $\theta$ , i.e. the regression slope in log slope-log area plots. These authors hence conclude that both values are effective measures of profile concavity.

<u>Variable</u>	<u>Unit</u>	<u>Definition</u>	<u>Source</u>
<b>Vertical shape</b>			
profile concavity		normalized area under the normalized distance-elevation profile (diagonal from source to mouth would be 0.5) PCI > 0.5 reflect a strongly convex profile	after Demoulin, 1998
hypsothetic integral		normalized area under a normalized area-elevation curve after Strahler	after Strahler, 1952
<b>Relief</b>			
basin mean elevation	m		
total basin relief	m	basin maximum elevation - basin minimum elevation	
basin local relief	m	local relief averaged over a circle with a diameter of 10 cells	after Summerfield, 1991
<b>Climate</b>			
mean annual rainfall	mm a <sup>-1</sup>		TRMM 30km dataset
modern perennial snowline	m		after Schwerdtfeger, 1976; Rabassa and Clapperton, 1990
lowest Pleistocene glacier extent	m		after Schwerdtfeger, 1976; Rabassa and Clapperton, 1990

*Table 6.1: Selection of investigated variables extracted for each catchment. See Appendix A for more detail. In our study, we will mainly concentrate on basin mean elevation, basin total and local relief, mean annual rainfall, and snowline as well as glacier extent.*

The hypsothetic integral (HI) describes the distribution of elevations in a drainage basin. The HI is calculated as the normalized area under a normalized area-elevation curve, following Strahler (1952) (Fig. 6.2). It is interpreted as a reflection of the geomorphic evolutionary stage and the degree of tectonic activity of a landscape (Strahler, 1952; Strahler, 1957; Summerfield, 1991; Ohmori, 1993).

The variables were correlated separately for all basin groups. We excluded strongly covarying variables, which might express similar characteristics. In our interpretation, we will focus on a few key parameters that we identified to best elucidate the interactions between relief, topography, rainfall, and snowline. The significance level for all correlations was set to the 95 % confidence interval of a two tailed t-test. As a goodness-of-fit measure for the correlations and regressions we used  $R^2$ .

## 6.4 Results

Our comprehensive dataset reveals a strong influence of rainfall on topography along the western flank of the Andean margin. See Appendix A for a detailed list of all correlations and raw data. A negative correlation exists between rainfall versus basin mean elevation, total relief, PCI, and HI (Fig. 6.3). A similar relationship exists between snowline and Pleistocene glacier extent versus these relief parameters. Both, modern snowline and Pleistocene glacier extent are closely linked to rainfall (Fig. 6.3) supporting the notion that glaciation in large parts of the central Andes is moisture-controlled. This is in good agreement with results from Haselton et al. (2002) who concluded that the Pleistocene snowline in the Altiplano-Puna region is more sensitive to moisture increases than temperature. However, the decrease of mean elevations is also apparent in basins that do not reach the snowline and have not been affected by glaciation, i.e. most mountain-front and all forearc catchments (Fig. 6.3). The correlation between HI and PCI versus rainfall is probably partly determined by relief parameters. HI, for example, is coupled to basin mean elevation, which itself is correlated with rainfall (Fig. 6.3).

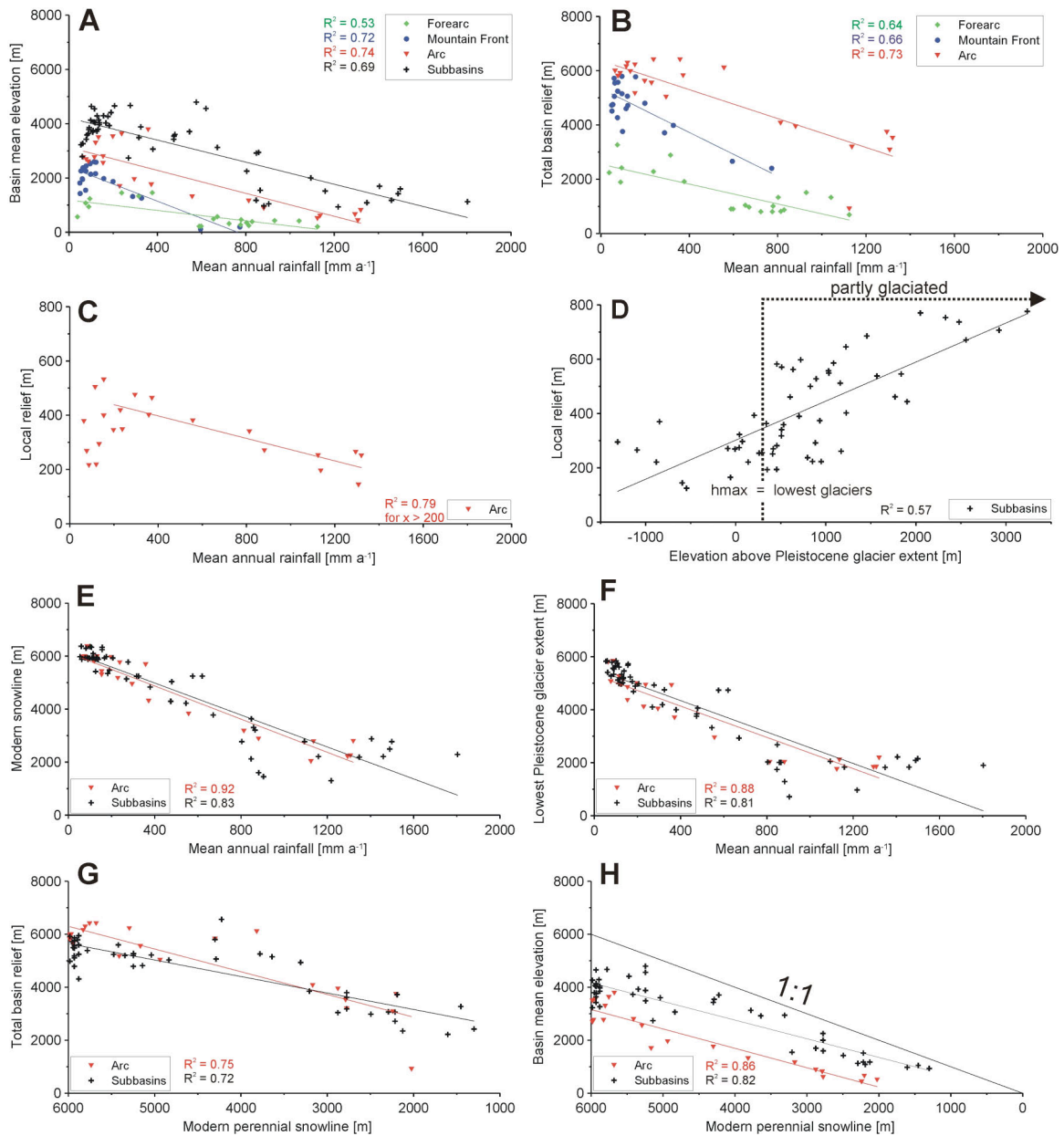


Fig. 6.3: Correlations between relief and climate variables. Plots A and B show a negative relationship between total basin relief as well as basin mean elevation versus rainfall. Plots A to C and E to H are broadly north-south oriented from left to right. Note the inverse x-axes of the relief variables versus snowline (G, H). Plot D shows that the local relief increases the higher the basins reach above the Pleistocene glacier extent. Note the close relationship between snowline and glaciers versus rainfall (E, F).

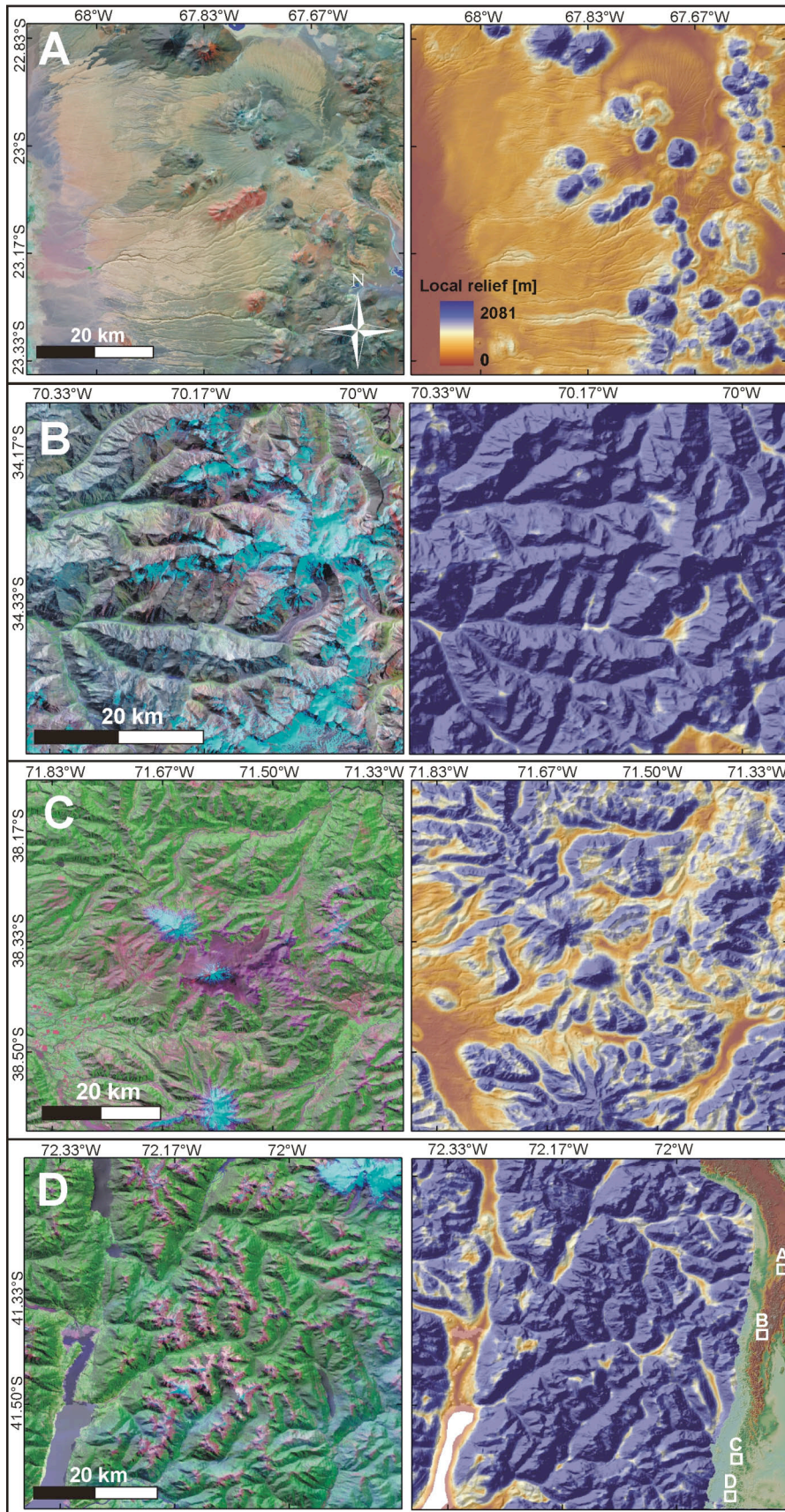
Satellite images of typical headwater basins reveal the distinct character of local catchment relief in the different climatic zones (Fig. 6.4). The northern basins in the hyperarid part display very low local relief. This landscape is virtually undissected and characterized by extremely low erosion rates  $< 0.1 \text{ m Ma}^{-1}$  (Nishiizumi et al., 2005) resulting in the preservation of mid-Miocene relict surfaces (Rech et al., 2006) (Fig. 6.4 A). Only those regions traversed by rivers originating in the high volcanic arc are characterized by deeply cut canyons (Zeilinger et al., 2005; Hoke et al., 2007; Schildgen et al., 2007). In contrast, headwaters in the semiarid-subhumid transition zone between  $28^\circ$  to  $35^\circ\text{S}$  are highly dissected. These subbasins have steep hillslopes, sharp ridges, and record glacial overprint (Fig. 6.4 B). The catchments in the humid south between  $35^\circ$  and  $40^\circ\text{S}$  display a smooth local relief with moderate hillslopes and subrounded ridges (Fig. 6.4 C). However, south of  $40^\circ\text{S}$  the landscape has again

steeper hillslopes and a higher degree of dissection (Fig. 6.4 D). These observations are clearly reflected in our data (Fig. 6.5).

Between  $\sim 18^\circ$  to  $28^\circ\text{S}$  modern snowline and the lowest extent of Pleistocene glaciation lie well above the maximum elevations of the ranges. Both modern and Pleistocene ELA start to descend southward when rainfall amounts rise. The modern snowline approaches the mean elevations until it undercuts the latter at a latitude of about  $42^\circ\text{S}$  (Fig. 6.3). The maximum elevation of the basins are reached by the snowline and the lowest Pleistocene glacier extent already farther north at  $\sim 32^\circ\text{S}$  (mountain-front catchments),  $\sim 27^\circ\text{S}$  (arc catchments), and  $\sim 28^\circ\text{S}$  (subcatchments), thus depending on latitude and elevation (Fig. 6.5). Basins south of these regions have been at least partially glaciated during Pleistocene. Most interestingly, between  $28^\circ$  and  $35^\circ\text{S}$  local relief displays a prominent maximum, and mean annual rainfall amounts are still low (Fig. 6.5). In fact, once the maximum elevation is undercut by the snowline, basin sectors above this line display a progressive linear increase in local relief (Fig. 6.3). In contrast, local relief and maximum elevations significantly decrease southward where rainfall amounts exceed  $\sim 800 \text{ mm a}^{-1}$  (Fig. 6.5). Local relief reaches a minimum between  $35^\circ$  and  $40^\circ\text{S}$ , where rainfall amounts are highest. South of  $40^\circ\text{S}$  local relief appears to increase again.

Basin-geometry variables strongly covary with each other, however they show no correlation to relief or climate parameters (Appendix A). We thus conclude that basin geometry is generally independent of relief and climate.

*Fig. 6.4 (overleaf): Landsat TM images in the left column and corresponding local relief map in the right column showing one typical headwater basins of each climatic zone. The inset in the lower right corner delineates the location of the close-ups. (A): Hyperarid subtropical desert belt. Note the absence of incision and significant local relief in this transport-limited setting. (B): Arid-semiarid transition zone. Note the glacial imprint, the highly dissected landscape, steep hillslopes, and sharp ridges forming a high local relief. (C): Humid, temperate climate. Note the moderate hillslopes, smooth ridges, sediment-filled valleys, and generally decreased dissection and local relief. (D): Humid, cold region. Note the increased local relief expressed in steeper valleys, dissected landscape, and pronounced ridges.*



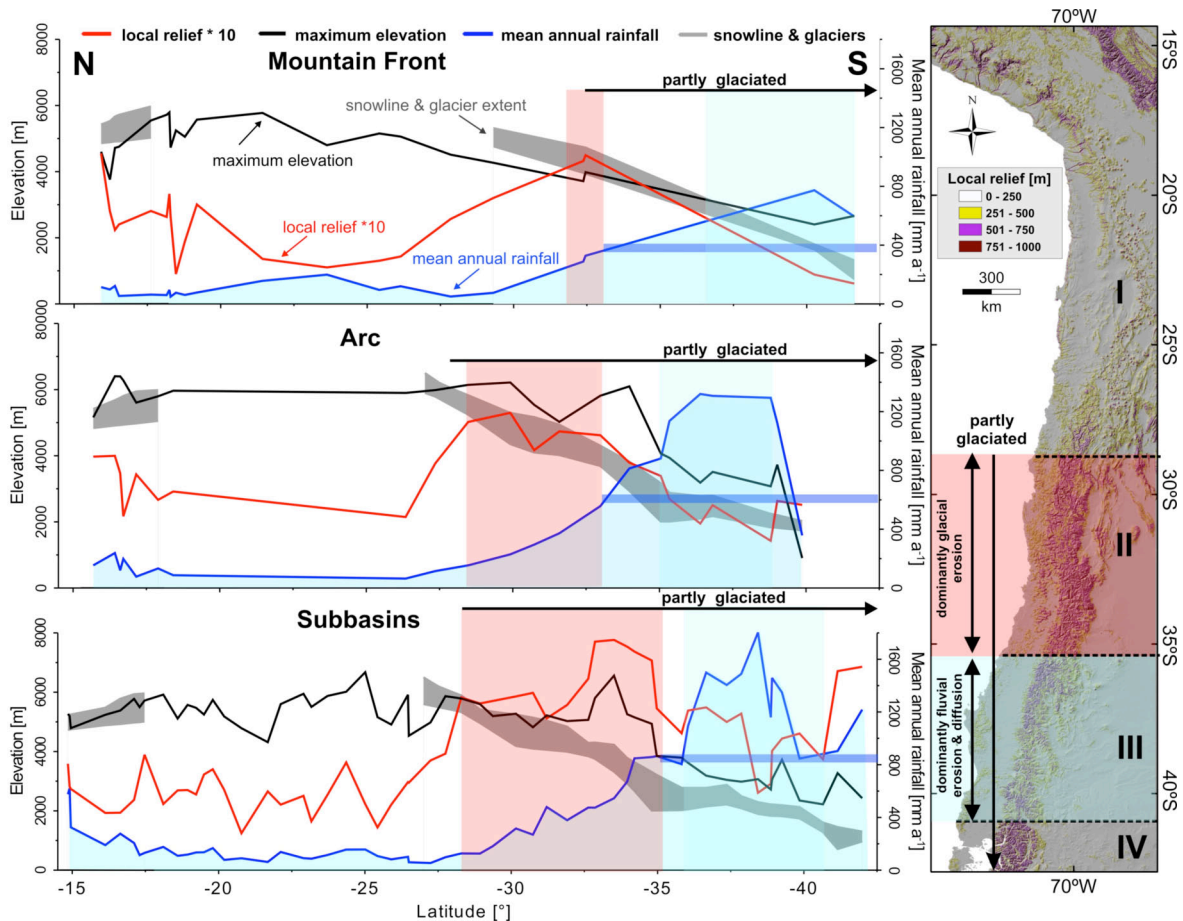


Fig. 6.5: North-south distribution of relief and climate parameters. Note the local-relief maximum around 28° to 35°S coinciding with increasing rainfall in the arid-semiarid transition zone and the undercutting of the basin maximum elevations by the snowline and the lowest Pleistocene glacier extent (red rectangle). When rainfall amounts increase and exceed  $\sim 800 \text{ mm a}^{-1}$  (blue bar) local relief is reduced and maximum elevations drop significantly. Local relief reaches a minimum around 35° to 40°S where rainfall rates are highest. This suggests that glacial and fluvial together with hillslope erosion are counteracting resulting in a glacially-dominated high-relief landscape where rainfall is low ( $\sim 28^\circ - 35^\circ\text{S}$ ) and a diffusion-dominated low-relief landscape where erosion is efficient due to high rainfall amounts ( $\sim 35^\circ - 40^\circ\text{S}$ ). South of 40°S local relief appears to rise again in the subcatchments. The right map shows the local relief sectors in roman numbers. Note the enhanced local relief in sector II (Figure 6.4 B) and the smoothed relief in sector III (Figure 6.4 C). The thin dotted lines indicate tectonic segments. South of  $\sim 27^\circ\text{S}$  catchments are partially influenced by glaciation. The region between 28° to 35°S is dominated by glacial erosion, the region between 35° and 40°S by fluvial erosion and diffusive denudation.

## 6.5 Discussion

The analysis of 120 drainage basins between the Central and Southern Andes reveals a prominent relation between climate and topography. Mean elevation and total basin relief decrease with increasing rainfall as well as decreasing snowline and Pleistocene glacier extent (Fig. 6.3). Although snowline and glacier extent influence mean elevations, the correlation between rainfall versus mean elevation and total basin relief can also be observed in basins that have not been influenced by glacial erosion. Hence, the decrease in topography appears to be partly related to increasing rainfall.

The distribution of local relief along the margin is very differentiated. Figure 6.5 indicates a local-relief maximum around 28° to 35°S. This zone coincides with the onset of partial basin glaciation due to decreasing modern and Pleistocene snowline elevations, particularly on the western Andean flank, since the region south of 28°S is dominated by westerly moisture (Clapperton, 1994; Haselton et al., 2002). Thus, northwards-migrating Westerlies may have reached these latitudes and intensified rainfall during glacials, delivering enough moisture for glaciation in these threshold environments (e.g. Heusser, 1989; Lamy et al., 1999). South of 40°S, where glacial processes dominate landscape evolution, local relief starts to increase again (Fig. 6.4 and 6.5). We therefore suggest that the high local relief between 28° and 35°S is the result of repeated glacial erosion during Pleistocene. The present-day low rainfall amounts promote the preservation of this dominantly glacial relief.

In contrast, farther south around 35°S local relief drops significantly despite the fact that the elevation of the snowline continues to descend (Fig. 6.5). Interestingly, this decrease starts in all catchments when rainfall amounts exceed  $\sim 800 \text{ mm a}^{-1}$  (Fig. 6.5). Additionally, local relief reaches its minimum where rainfall amounts are highest. Based on these observations we suggest that  $800 \text{ mm a}^{-1}$  might be a critical threshold-rainfall amount above which the fluvial system is coupled to the hillslopes and efficiently erodes in these environments. We therefore conclude that the zone between 35° to 40°S is dominated by fluvial erosion associated with diffusive hillslope processes that help smooth mountain-range relief.

Mean annual rainfall [mm/a]	$\Delta$ Mean elevation [%]	$\Delta$ Total relief [%]	Position
50 - 100	118	8	Forearc
	18	-20	Mountain Front
	0	3	Arc
	44	-37	Subbasins
	<b>45</b>	<b>-12</b>	<b>Average</b>
100 - 200	-24	-38	Forearc
	-13	28	Mountain Front
	28	-9	Arc
	0	7	Subbasins
	<b>-2</b>	<b>-3</b>	<b>Average</b>
200 - 400	55	29	Forearc
	-33	-17	Mountain Front
	-50	4	Arc
	-34	91	Subbasins
	<b>-16</b>	<b>27</b>	<b>Average</b>
400 - 800	-76	-31	Forearc
	-85	-40	Mountain Front
	-34	-30	Arc
	-26	-27	Subbasins
	<b>-55</b>	<b>-32</b>	<b>Average</b>
800 - 1600	<-41	<-48	Forearc
	---	---	Mountain Front
	<-30	<-14	Arc
	-29	-10	Subbasins
	<b>-33</b>	<b>-24</b>	<b>Average</b>
>400	<b>-44</b>	<b>-28</b>	<b>Average</b>

Table 6.2: Relief reduction due to a doubling of rainfall. See the amount of rainfall and the respective change in mean elevation and total relief for each basin group. Note that mean elevation and total relief are only significantly reduced by doubling rainfall amounts above rainfall rates of  $400 \text{ mm a}^{-1}$ .

Our results are in agreement with other empirical and modeling studies proposing that high precipitation rates lower topography (Montgomery et al., 2001; Roe et al., 2003; Gabet et al., 2004). Roe et al. (2003) suggest that in environments dominated by rainfall, a mountain range can be lowered by more than half due to enhanced precipitation. In the tectonically active Himalaya Gabet et al. (2004) document that a doubling of rainfall from 2000 to 4000 mm results in a 33 %-decrease in total relief between valley and ridge crests. Despite significantly lower rainfall amounts in our study area, our results document a decrease in mean elevation and total relief on the order of 44 % and 28 %, respectively, for a doubling of rainfall

amounts  $> 400 \text{ mm a}^{-1}$  (Table 6.2). Such a rainfall-induced decrease in topography would imply an increase in erosion rates toward the south. Indeed, an increase of erosion rates and terrigenous sediment accumulation in the trench is well documented along the Andean margin (Scholl et al., 1970; Montgomery et al., 2001; Lamb and Davis, 2003; Melnick and Echtler, 2006a; Hebbeln et al., 2007).

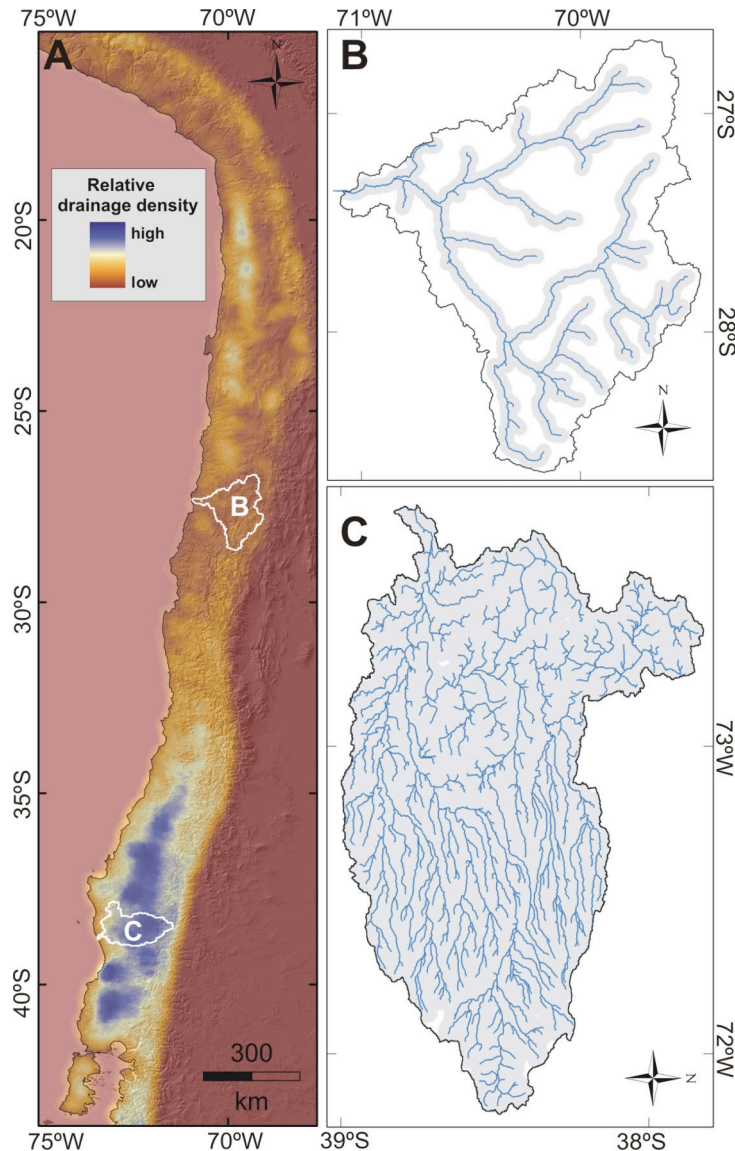


Fig. 6.6: (A): Relative drainage density along the margin calculated as the cumulative channel length per unit area. On the right see close-ups of two catchments representative for the arid (B) and humid (C) part of the study area. Note the significantly higher drainage density in the south where rainfall amounts are increased. The grey-shaded regions in basins (B) and (C) outline the parts of the catchments that are integrated in the fluvial network and thus denudated. In catchments with a higher drainage density in the south the entire basin with all hillslopes is integrated whereas dry catchments in the north display distinct ridges and interfluvies not reached by the drainage network.

Previous studies suggested that a rainfall-induced enhanced erosivity is controlled by an increase in drainage density, resulting in a lowering of hillslope, tributary, and trunk channel relief, as well as threshold hillslope angles (Tucker and Bras, 1998; Whipple et al., 1999; Reiners et al., 2003; Gabet et al., 2004). In fact, enhanced rainfall is associated with a progressive southward increase of drainage density (Fig. 6.6). High drainage density causes more effective denudation of higher

catchment parts that are not integrated in the fluvial network when drainage density is lower (Fig. 6.6). As a result, total and local relief decrease with increasing drainage density and increasing rainfall when fluvial processes coupled to diffusion dominate. In contrast, glacial erosion has been shown to be one of the main relief-generating processes focusing erosion near the peaks and thereby maintaining steep topography at and above the ELA (Hallet et al., 1996; Small and Anderson, 1998; Tomkin and Braun, 2002; Mitchell and Montgomery, 2006). The erosional effect of glaciers has been likened to the “buzz-saw effect”, effectively reducing the overall topography of mountain-ranges (Brozovic et al., 1997).

Consequently, we distinguish two geomorphic zones in the Central to Southern Andes. Between 28° to 35°S rainfall amounts are below a critical threshold rendering fluvial erosion ineffective. Hence, glacial erosion, generating local relief, is the dominant process. Between 35° and 40°S fluvial erosion, enhanced by higher rainfall amounts, dominates landscape evolution and diminishes local relief (Fig. 6.5).

PCI and HI as indicators for the general topography of basin and channels are reduced with enhanced rainfall. Our data expands the rainfall range of other studies significantly (e.g. Zaprowski et al., 2005) and supports the conclusions of those studies that less intense precipitation is correlated with convex profiles (high PCI), whereas concave profiles (low PCI) develop in regions with intense rainfall (Roe et al., 2002; Zaprowski et al., 2005). Although we do not identify rainfall variations along single longitudinal-river profiles in this study, the inverse relationship between rainfall and channel concavity probably reflects the more efficient erosion at higher rainfall rates, where rivers adjust faster to changes in boundary conditions and approach equilibrium profiles. The HI is typically used to infer the geomorphic and tectonic age of a landscape (Strahler, 1952; Ohmori, 1993). However, HI scales with mean elevation, which appears to be partly correlated with rainfall. Consequently, due to differences in rainfall and denudation rates, a basin in an arid environment is probably much older than a basin in a humid climate with the same HI. In contrast, two basins, which started to uplift at the same time, but are situated in different climatic zones should exhibit significantly distinct HI-values. Therefore, HI-values should only be used relative to each other as proxies for tectonic activity in similar climatic settings. It appears to be more suitable to interpret the HI with respect to the efficiency of erosion processes in drainage basins, which is supported by results of Montgomery et al. (2001).

Clearly, erosion and topography in mountain belts are also determined by tectonic processes. In the Andes, the shortening rate decreases towards the south, absolute shortening is reduced by more than 30 % from high shortening (> 300 km) to low shortening (< 100 km) at around 30°S (e.g. Allmendinger et al., 1990; Vietor and Echtler, 2006) (Fig. 6.1). However, we observe the local-relief maximum at 28° to 35°S, already in a sector where shortening is low, hence the opposite of what might be expected if shortening were a controlling factor for local relief. Furthermore, active deformation in the Central Andes is mainly observed as far south as 36°S (Mpodozis and Ramos, 1989; Vietor and Echtler, 2006). Consequently, the sectors defined by local relief and dominant geomorphic process are not consistent with tectonic segments. Last, the high-relief sector does not coincide with distinct rocks comprising a lower erodibility (Sernageomin, 2003). A lithologic control can thus be excluded as well. Conclusively, neither changes in shortening rate, lithology, nor the distribution of deformation alone can account for the local relief maximum. Apparently, local relief along the Andean margin is mainly determined by the long-term climatic zonation.

## 6.6 Conclusion

We analyzed the relation between basin geometry, climate, and topographic parameters in 120 drainage basins along the western Andean flank between 15.5° and 41.5°S based on SRTMV3-90m topographic data as well as the medium-resolution TRMM-dataset. Our analysis shows that basin geometry is not affected by climate along the Andean margin. Conversely, the relief parameters, PCI, and HI are strongly dependent on rainfall highlighting the importance of climate in attempting to derive information about tectonics from river profiles and hypsometry.

Furthermore, our results suggest that increased rainfall diminishes mean and maximum elevations of mountain ranges. This is similar to the impact of glaciation on total range topography, which focuses erosion on summits and ridges at, and above the ELA. This underscores the complex relationships between tectonics creating topography and rainfall as well as glaciers that decrease total range relief. With respect to the generation of local relief we propose that coupled fluvial and hillslope erosion and glacial erosion are opponents. Whereas glacial erosion appears to create local relief, moderate rainfall above a critical threshold promote diffusive processes and thus substantially smooth local relief. Accordingly, a climate shift to humid conditions or a transition from dominantly glacial to dominantly fluvial erosion is expected to reduce total and local relief. Hence, although the large-scale architecture of the Andean mountain chain is maintained by tectonic processes and inherited structures, our data suggest that the catchment-scale relief mainly reflects the dominant geomorphic process determined by the regional climatic conditions. In turn, this indicates that the geomorphic signature of landscapes inheres a significant transient component which may reflect erosion processes during the recent geologic past. Conversely, these geomorphic signatures can be used to identify past paleoclimatic extents if these processes occurred over a sufficiently long time interval. However, due care has to be exercised when interpreting landscapes as a mirror of modern climate.

## Acknowledgements

This work was funded by Deutsche Forschungsgemeinschaft through the Leibniz Award to Manfred Strecker (STR373-18-1), the A. Cox fund of Stanford University, and supported by the GeoForschungsZentrum Potsdam as well as the DAAD, the German Academic Exchange Program, to Katrin Rehak. We appreciate discussions with George Hilley.

## 7. Conclusions

In this study I discuss and answer questions concerning the role of morphotectonic segments with respect to forearc morphology, their persistence as morphotectonic entities as well as their relation to earthquake-rupture zones, the evolution of tectonic and geomorphic processes through time, and the climatic control on geomorphic processes and landscapes along the margin of central to southern Chile. I provide new results on the evolution of the highly dynamic forearc region of south-central Chile in particular, and insights into the complex interplay between climate and tectonics in composite landscapes in general.

(1) I investigated the forearc with regard to morphotectonic segments and identified three segments that record a distinct geomorphic and tectonic evolution. From north to south these segments are the Nahuelbuta, Toltén, and Bueno segments. The Coastal Cordillera in both, the Nahuelbuta and the Bueno segments, undergoes active tectonic uplift documented by flights of marine terraces, uplifted planation surfaces, ongoing river incision, and severe drainage perturbations. In contrast, the middle Toltén segment, characterized by flat topography and a lack of incision, appears to be quasi-stable. My observations suggest that this morphotectonic segmentation is persistent in the long-term and thus not related to the activity of short-lived earthquake-rupture zones. This was confirmed by reconstructing the uplift history of the northern Nahuelbuta segment on a timescale of  $10^6$  years applying cosmogenic-nuclide dating with  $^{10}\text{Be}$  and  $^{26}\text{Al}$ .

(2) The results suggest that the uplift of the Coastal Cordillera started in Pliocene time about 5 Ma ago which coincided with the establishment of the morphotectonic segmentation of this forearc. In line with other studies quantifying the sedimentation patterns in the trench this implies that the onshore and offshore forearc uplifted contemporaneously, related to a shift from subduction erosion to subduction accretion. This took place about 5 Ma ago and may have coincided with the onset of global cooling and higher glacial sediment production. In fact, the initiation of Patagonian glaciation ~ 6 Ma ago is followed by fundamental modifications of the subduction and surface process system along the south-central Chile margin. Various studies document changes from extensional to compressional deformation, from subsidence to uplift, from erosive to accretive subduction, from marine to continental deposition at the late Miocene to early Pliocene boundary. Importantly, my data clearly indicates that the forearc of south-central Chile obtained its present morphologic characteristics only during the Pliocene to Quaternary.

(3) Interestingly, late Pleistocene uplift rates derived by dating fluvial terraces with optically stimulated luminescence are higher than surface-uplift rates averaging over the last 5 Ma. This suggests that forearc uplift has accelerated during the late Quaternary, as corroborated by other data from the region. However, surface uplift is spatially variable due to preferred displacement along crustal-scale reverse faults. These faults – the locus of subduction-zone interplate earthquakes - control the degree and spatial distribution of deformation. This is supported by a late Pleistocene flow reversal in a growing crustal-scale anticline that appears to be related to uplift above a blind reverse fault. Surface uplift is transient and variable in time and space in this forearc setting, indicating a highly dynamic system, where subduction and related surface processes are closely linked.

(4) The Central Depression in south-central Chile is characterized by extensive depositional surfaces constituted by thick gravel sheets. According age determinations using  $^3\text{He}$  and  $^{21}\text{Ne}$  these surfaces were accumulated 150 to 300 ka ago. The recent geomorphic expression of this region has thus been established in late Pleistocene

time. The distribution of ages indicates that the deposition of these surfaces may have been climatically controlled and may have been related to outwash processes toward the end of late Pleistocene glacial stages. Hence, although the landscape of the south-central Chile forearc is significantly influenced by tectonics, it additionally preserves the imprint of pronounced climatic forcing.

(5) A climatic signal can also be seen in catchment-scale local relief along the Central to Southern Andes. Dependent on the dominant geomorphic process, which is determined by climate, relief varies significantly. Additionally, this reveals a pronounced transient component in landscape evolution reflecting surface processes active during past climatic conditions. Consequently, due care has to be exercised when interpreting landscapes as reflections of modern climates.

In conclusion, my study has shown that it is useful to analyze geomorphic markers reflecting different timescales and processes in order to elucidate the role of surface processes, and hence climate, in shaping landscapes in tectonically active regions. The data presented in this thesis shows a consistent picture of the tectonic and geomorphic evolution of the study area. However, the spatial density of the dataset could be further improved in future by investigating other geomorphic markers in order to increase the statistic reliability of the results.

My results allow the identification and differentiation of climatically and tectonically determined landscape components. Nevertheless, a future task would be to increase the temporal resolution and spatial density of the data in order to identify and correlate singular climatic events. In this context, cosmogenic nuclides would provide an excellent tool to quantify and compare present and past surface-process rates in different settings. My study shows that the accumulation of large sediment deposits in the south-central Chile forearc is primarily controlled by climate. Hence, fluvial and alluvial terraces may constitute excellent archives of past erosional regimes and could thus be used to reconstruct the climatic history of many settings in which sediment deposition is climatically driven.

## 8. Bibliography

- Adriasola, A.C., Thomson, S.N., Brix, M.R., Hervé, F., and Stockhert, B., 2006, Postmagmatic cooling and late Cenozoic denudation of the North Patagonian Batholith in the Los Lagos region of Chile, 41°-42°15'S: *International Journal of Earth Sciences*, v. 95, p. 504-528.
- Aguirre Le-Bert, L., Hervé, A.F., and Godoy, P.B.E., 1972, Distribution of metamorphic facies in Chile - an outline: *Krystalinikum*, v. 9, p. 7-19.
- Aitken, M.J., 1998, *An introduction to optical dating*: Oxford, Oxford University Press, 282 p.
- Aldrich, L.T., and Nier, A.O., 1948, The occurrence of <sup>3</sup>He in natural sources of helium: *Physical Reviews*, v. 74, p. 1590-1594.
- Allmendinger, R.W., Jordan, T.E., Kay, S.M., and Isacks, B.L., 1997, The evolution of the Altiplano-Puna plateau of the Central Andes: *Annual Review of Earth and Planetary Sciences*, v. 25, p. 139-174.
- Allmendinger, R.W., Figueroa, O., Snyder, D., Beer, J., Mpodozis, C., and Isacks, B.L., 1990, Foreland shortening and crustal balancing in the Andes at 30°S latitude: *Tectonics*, v. 9, p. 789-809.
- Ammann, C., Jenny, B., Kammer, K., and Messerli, B., 2001, Later Quaternary glacier response to humidity changes in the arid Andes of Chile (18-29°S): *Palaeogeography Palaeoclimatology Palaeoecology*, v. 172, p. 313-326.
- Angermann, D., Klotz, J., and Reigber, C., 1999, Space-geodetic estimation of the Nazca South America Euler vector: *Earth and Planetary Science Letters*, v. 171, p. 329-334.
- Atwater, B.F., Jiménez Núñez, H., and Vita-Finzi, C., 1992, Net late Holocene emergence despite earthquake-induced submergence, South-central Chile: *Quaternary International*, v. 15/16, p. 77-85.
- Bangs, N.L., and Cande, S.C., 1997, Episodic development of a convergent margin inferred from structures and processes along the southern Chile margin: *Tectonics*, v. 16 (3), p. 489-503.
- Barrientos, S., Plafker, G., and Lorca, E., 1992, Postseismic coastal uplift in southern Chile: *Geophysical Research Letters*, v. 19, p. 701-704.
- Barrientos, S.E., and Ward, S.N., 1990, The 1960 Chile earthquake: inversion for slip distribution from surface deformation: *Geophysical Journal International*, v. 103, p. 589-598.
- Beaumont, C., Fullsack, P., and Hamilton, J., 1992, Erosional control of active compressional orogens, in McClay, K.R., ed., *Thrust Tectonics*: London, Chapman & Hall, p. 1-18.

- Beck, S., Barrientos, S., Kausel, E., and Reyes, M., 1998, Source characteristics of historic earthquakes along the central Chile subduction zone: *Journal of South American Earth Sciences*, v. 11 (2), p. 115-129.
- Bice, K.L., Scotese, C.R., Seidov, D., and Barron, E.J., 2000, Quantifying the role of geographic change in Cenozoic ocean heat transport using uncoupled atmosphere and ocean models: *Palaeogeography Palaeoclimatology Palaeoecology*, v. 161, p. 295-310.
- Bierman, P.R., Caffee, M.W., Davis, P.T., Marsella, K., Pavich, M., Colgan, P., Mickelson, D., and Larsen, J., 2002, Rates and timing of earth surface processes from in situ-produced cosmogenic <sup>10</sup>Be, Beryllium: *Mineralogy, Petrology, and Geochemistry*, Volume 50: *Reviews in Mineralogy & Geochemistry*, p. 147-205.
- Bierman, P., and Steig, E.J., 1996, Estimating rates of denudation using cosmogenic isotope abundances in sediment: *Earth Surface Processes and Landforms*, v. 21, p. 125-139.
- Bierman, P.R., 1994, Using in-situ produced cosmogenic isotopes to estimate rates of landscape evolution - a review from the geomorphic perspective: *Journal of Geophysical Research-Solid Earth*, v. 99, p. 13885-13896.
- Bishop, P., and Goldrick, G., 2000, Geomorphological evolution of the East Australian continental margin, in Summerfield, M.A., ed., *Geomorphology and Global Tectonics*: New York, John Wiley and Sons, p. 225-255.
- Blisniuk, P.M., Stern, L.A., Chamberlain, C.P., Idleman, B., and Zeitler, P.K., 2005, Climatic and ecologic changes during Miocene surface uplift in the Southern Patagonian Andes: *Earth and Planetary Science Letters*, v. 230, p. 125-142.
- Bohm, M., 2004, 3-D Lokalbebentomographie der südlichen Anden zwischen 36° und 40°S [Scientific Technical Report STR04/15, PhD thesis]: Potsdam.
- Bohm, M., Lüth, S., Echtler, H., Asch, G., Bataille, K., Bruhn, C., Rietbrock, A., and Wigger, P., 2002, The southern Andes between 36° and 40°S latitude: seismicity and average seismic velocities: *Tectonophysics*, v. 356, p. 275-280.
- Bookhagen, B., and Strecker, M., 2008, Orographic barriers, high-resolution TRMM rainfall, and relief variations along the eastern Andes: *Geophysical Research Letters*, v. 35.
- Bookhagen, B., Echtler, H.P., Melnick, D., Strecker, M., and Spencer, J.Q.G., 2006a, Using uplifted Holocene beach berms for paleoseismic analysis on the Santa Maria Island, south-central Chile: *Geophysical Research Letters*, v. 33, p. doi:10.1029/2006GL026734.
- Bookhagen, B., Fleitmann, D., Nishiizumi, K., Strecker, M.R., and Thiede, R.C., 2006b, Holocene monsoonal dynamics and fluvial terrace formation in the northwest Himalaya, India: *Geology*, v. 34, p. 601-604.
- Brenan, J.M., Neroda, E., Lundstrom, C.C., Shaw, H.F., Ryerson, F.J., and Phinney, D.L., 1998, Behavior of boron, beryllium, and lithium during melting and crystallization: Constraints from mineral-melt partitioning experiments: *Geochimica et Cosmochimica Acta*, v. 62, p. 2129-2141.

- Brooks, B.A., Bevis, M., Smalley, R.J., Kendrick, E., Manceda, R., Lauria, E., Manturana, R., and Araujo, M., 2003, Crustal motion in the Southern Andes (26°-36°S): do the Andes behave like a microplate? *Geochemical Geophysical Geosystems*, v. 4, p. 10.1029.
- Brown, L., Pavich, M.J., Hickman, R.E., Klein, J., and Middleton, R., 1988, Erosion of the eastern United States observed with <sup>10</sup>Be: *Earth Surface Processes and Landforms*, v. 13, p. 441-457,
- Brozovic, N., Burbank, D.W., and Meigs, A.J., 1997, Climatic limits on landscape development in the northwestern Himalaya: *Science*, v. 276, p. 571-574.
- Brüggen, J., 1950, *Fundamentos de la Geología de Chile*, Instituto Geográfico Militar.
- Bruhn, C., 2003, *Momenttensoren hochfrequenter Ereignisse in Südchile* [PhD thesis], Potsdam.
- Carrapa, B., Adelmann, D., Hilley, G.E., Mortimer, E., Sobel, E.R., and Strecker, M.R., 2005, Oligocene range uplift and development of plateau morphology in the southern central Andes: *Tectonics*, v. 24.
- Cattin, R., LyonCaen, H., and Chery, J., 1997, Quantification of interplate coupling in subduction zones and forearc topography: *Geophysical Research Letters*, v. 24, p. 1563-1566.
- Cembrano, J., Schermer, E., Lavenu, A., and Sanhueza, A., 2000, Contrasting nature of deformation along an intra-arc shear zone, the Liqueine-Ofqui fault zone, southern Chilean Andes: *Tectonophysics*, v. 319, p. 129-149.
- Cerling, T.E., and Craig, H., 1994, Geomorphology and in-situ cosmogenic isotopes: *Annual Reviews of Earth and Planetary Sciences*, v. 22, p. 273-317.
- Charrier, R., Pinto, L., and Rodriguez, M.P., 2007, Tectonostratigraphic evolution of the Andean Orogen in Chile, in Moreno, T., and Gibbons, W., eds., *The geology of Chile*, The Geological Society, p. 440.
- Cifuentes, I.L., 1989, The 1960 Chilean earthquake: *Journal of Geophysical Research*, v. 94, p. 665-680.
- Cisternas, M., Atwater, B.F., Torrejon, F., Sawai, Y., Machuca, G., Lagos, M., Eipert, A., Youlton, C., Salgado, I., Kamataki, T., Shishikura, M., Rajendran, C.P., Malik, J.K., Rizal, Y., and Husni, M., 2005, Predecessors of the giant 1960 Chile earthquake: *Nature*, v. 437, p. 404-407.
- Clapperton, C.M., 1994, The Quaternary glaciation of Chile - a review: *Revista Chilena de historia natural*, v. 67, p. 369-383.
- Clapperton, C.M., 1993, Nature of environmental-changes in South-America at the Last Glacial Maximum: *Palaeogeography Palaeoclimatology Palaeoecology*, v. 101, p. 189-208.
- Clift, P., and Vannucchi, P., 2004, Controls on tectonic accretion versus erosion in subduction zones: Implications for the origin and recycling of the continental crust: *Reviews of Geophysics*, v. 42.

- Clift, P.D., Pecher, I., Kukowski, N., and Hampel, A., 2003, Tectonic erosion of the Peruvian forearc, Lima Basin, by subduction and Nazca Ridge collision: *Tectonics*, v. 22, p. TC001386.
- Darwin, C., 1846, *Geological observations on South America*: London, 279 p.
- Davis, D., Suppe, J., and Dahlen, F.A., 1983, Mechanics of fold-and-thrust belts and accretionary wedges: *Journal of Geophysical Research*, v. 88, p. 1153-1172.
- Demets, C., Gordon, R.G., Argus, D.F., and Stein, S., 1994, Effect of recent revisions to the geomagnetic reversal timescale on estimates of current plate motions: *Geophysical Research Letters*, v. 21, p. 2191-2194.
- Demoulin, A., 1998, Testing the tectonic significance of some parameters of longitudinal river profiles: the case of the Ardenne (Belgium, NW Europe): *Geomorphology*, v. 24, p. 189-208.
- Dewey, J.F., and Lamb, S.H., 1992, Active tectonics of the Andes: *Tectonophysics*, v. 205, p. 79-95.
- Dewey, J.F., and Horsfield, B., 1970, Plate tectonics, orogeny, and continental growth: *Nature*, v. 225, p. 521.
- Diraison, M., Cobbold, P.R., Rossello, E.A., and Amos, A.J., 1998, Neogene dextral transpression due to oblique convergence across the Andes of northwestern Patagonia, Argentina: *Journal of American Earth Sciences*, v. 11, p. 519-532.
- Dunai, T.J., Lopez, G.A.G., and Juez-Larre, J., 2005, Oligocene-Miocene age of aridity in the Atacama Desert revealed by exposure dating of erosion-sensitive landforms: *Geology*, v. 33, p. 321-324.
- Dunai, T.J., 2000, Scaling factors for production rates of in situ produced cosmogenic nuclides: a critical reevaluation: *Earth and Planetary Science Letters*, v. 176, p. 157-169.
- Dunai, T.J., and Wijbrans, J.R., 2000, Long-term cosmogenic  $^3\text{He}$  production rates (152 ka -1.35 Ma) from  $^{40}\text{Ar}/^{39}\text{Ar}$  dated basalt flows at 29°N latitude: *Earth and Planetary Science Letters*, v. 176, p. 147-156.
- Dunne, J., Elmore, D., and Muzikar, P., 1999, Scaling factors for the rates of production of cosmogenic nuclides for geometric shielding and attenuation at depth on sloped surfaces: *Geomorphology*, v. 27, p. 3-11.
- Echtler, H., 2008, Pers. comm.
- Echtler, H., Glodny, J., Gräfe, K., Rosenau, M., Melnick, D., Seifert, W., and Vietor, T., 2003, Active tectonics controlled by inherited structures in the long-term stationary and non-plateau south-central Andes, EGU/AGU Joint Assembly: Nice, p. EAE03-A-10902.
- Elger, K., Oncken, O., and Glodny, J., 2005, Plateau-style accumulation of deformation: Southern Altiplano: *Tectonics*, v. 24.

- Encinas, A., Finger, K.L., Nielsen, S.N., Lavenu, A., Buatois, L.A., Peterson, D.E., and Jacobus, P.L.R., 2008, Rapid and major coastal subsidence during the late Miocene in south-central Chile: *Journal of South American Earth Sciences*, v. 25, p. 157-175.
- Engdahl, E.R., and Villasenor, A., 2002, Global Seismicity: 1900-1999, in Lee, W.H.K., Kanamori, H., Jennings, P.C., and Kisslinger, C., eds., *International Handbook of Earthquake and Engineering Seismology, Volume International Geophysics Series (81A)*: Amsterdam, Academic Press, p. 665-690.
- Engdahl, E.R., Hilst van der, R., and Buland, R., 1998, Global teleseismic earthquake relocation with improved travel times and procedures for depth determination: *Bulletin of the Seismological Society of America*, v. 88, p. 722-743.
- Fabel, D., Fink, D., Fredin, A., Harbor, J., Land, M., and Stroeven, A.P., 2006, Exposure ages from relict lateral moraines overridden by the Fennoscandian ice sheet: *Quaternary Research*, v. 65, p. 136-146.
- Fabel, D., and Harbor, J., 1999, The use of in-situ produced cosmogenic radionuclides in glaciology and glacial geomorphology, Volume 28: *Annals of Glaciology*, p. 103-110.
- Farias, M., Charrier, R., Comte, D., Martinod, J., and Herail, G., 2005, Late Cenozoic deformation and uplift of the western flank of the Altiplano: Evidence from the depositional, tectonic, and geomorphologic evolution and shallow seismic activity (northern Chile at 19°30' S): *Tectonics*, v. 24.
- Finger, K.L., Nielsen, S.N., Devries, T.J., Encinas, A., and Peterson, D.E., 2007, Paleontologic evidence for sedimentary displacement in Neogene forearc basins of central Chile: *PALAIOS*, v. 22, p. 3-16.
- Finlayson, D.P., Montgomery, D.R., and Hallet, B., 2002, Spatial coincidence of rapid inferred erosion with young metamorphic massifs in the Himalayas: *Geology*, v. 30, p. 219-222.
- Fuller, C.W., Willett, S.D., and Brandon, M.T., 2006, Formation of forearc basins and their influence on subduction zone earthquakes: *Geology*, v. 34, p. 65-68.
- Gabet, E.J., Pratt-Sitaula, B.A., and Burbank, D.W., 2004, Climatic controls on hillslope angle and relief in the Himalayas: *Geology*, v. 32, p. 629-632.
- Gansser, A., 1973, Facts and theories on the Andes: *Journal of the Geological Society of London*, v. 129, p. 93-131.
- Gardner, T., Marshall, J., Merritts, D., Bee, B., Burgette, R., Burton, E., Cooke, J., Kehrwald, N., Protti, M., Fisher, D., and Sak, P., 2001, Holocene forearc block rotation in response to seamount subduction, southeastern Peninsula de Nicoya, Costa Rica: *Geology*, v. 29, p. 151-154.
- Gardner, T.W., Verdonck, D., Pinter, N.M., Slingerland, R., Furlong, K.P., Bullard, T.F., and Wells, S.G., 1992, Quaternary uplift astride the aseismic Cocos Ridge, Pacific Coast, Costa Rica: *Geological Society of America Bulletin*, v. 104, p. 219-232.

- Garreaud, R., Vuille, M., and Clement, A.C., 2003, The climate of the Altiplano: observed current conditions and mechanisms of past changes: *Palaeogeography Palaeoclimatology Palaeoecology*, v. 194, p. 5-22.
- Garzzone, C.N., Molnar, P., Libarkin, J.C., and MacFadden, B.J., 2006, Rapid late Miocene rise of the Bolivian Altiplano: evidence for removal of mantle lithosphere: *Earth and Planetary Science Letters*, v. 241, p. 543-556.
- Giambiagi, L.B., Ramos, V.A., Godoy, E., Alvarez, P.P., and Orts, S., 2003, Cenozoic deformation and tectonic style of the Andes, between 33° and 34° south latitude: *Tectonics*, v. 22.
- Glodny, J., Echtler, H., Collao, S., Ardiles, M., Buron, P., and Figueroa, O., in press, Differential late Paleozoic active margin evolution in south-central Chile (37°S-40°S) – The Lanalhue fault zone: *Journal of South American Earth Sciences*.
- Glodny, J., Gräfe, K., Echtler, H.P., and Rosenau, M., 2007, Mesozoic to Quaternary continental margin dynamics in south-central Chile (36°-42°S): the apatite and zircon fission track perspective: *International Journal of Earth Sciences*, DOI 10.1007/s00531-007-0203-1.
- Glodny, J., Lohrmann, J., Echtler, H., Gräfe, K., Seifert, W., Collao, S., and Figueroa, O., 2005, Internal dynamics of an accretionary wedge: insights from combined isotope tectonochronology and sandbox modeling of the south-central Chilean forearc: *Earth and Planetary Science Letters*, v. 231, p. 23-39.
- Gosse, J.C., and Phillips, F.M., 2001, Terrestrial in situ cosmogenic nuclides: theory and application: *Quaternary Science Reviews*, v. 20, p. 1475-1560.
- Granger, D.E., and Muzikar, P.F., 2001, Dating sediment burial with in situ-produced cosmogenic nuclides: theory, techniques, and limitations: *Earth and Planetary Science Letters*, v. 188, p. 269-281.
- Gregory-Wodzicki, K.M., 2000, Uplift history of the Central and Northern Andes: a review: *GSA Bulletin*, v. 112, p. 1091-1105.
- Gupta, S., 1997, Himalayan drainage patterns and the origin of fluvial megafans in the Ganges foreland basin: *Geology*, v. 25, p. 11-14.
- Gutscher, M.A., Malavieille, J., Lallemand, S., and Collot, J.Y., 1999, Tectonic segmentation of the north Andean margin: impact of the Carnegie Ridge collision: *Earth and Planetary Science Letters*, v. 168, p. 255-270.
- Haberland, C., Rietbrock, A., Lange, D., Bataille, K., and Hofmann, S., 2006, Interaction between forearc and oceanic plate at the south-central Chilean margin as seen in local seismic data: *Geophysical Research Letters*, v. 33.
- Hackney, R., Echtler, H., Franz, G., Götze, H.-J., Lucassen, F., Marchenko, D., Melnick, D., Meyer, U., Schmidt, S., Tašárová, Z., Tassara, A., and Wienecke, S., 2006, The segmented overriding plate and coupling at the south-central Chilean margin (36-42°S), in Oncken, O., Chong, G., Franz, G., Giese, P., Götze, H.-J., Ramos, V.A., Strecker, M., and Wigger, P., eds., *The Andes - Active Subduction Orogeny: Frontiers in Earth Sciences*: Berlin, Heidelberg, New York, Springer-Verlag, p. 355-374.

- Hallet, B., Hunter, L., and Bogen, J., 1996, Rates of erosion and sediment evacuation by glaciers: A review of field data and their implications: *Global and Planetary Change*, v. 12, p. 213-235.
- Hampel, A., Adam, J., and Kukowski, N., 2004, Response of the tectonically erosive south Peruvian forearc to subduction of the Nazca Ridge: analysis of three-dimensional analogue experiments: *Tectonics*, v. 23, p. TC5003.
- Hartley, A.J., 2003, Andean uplift and climate change: *Journal of the Geological Society*, v. 160, p. 7-10.
- Haselton, K., Hilley, G., and Strecker, M.R., 2002, Average Pleistocene climatic patterns in the southern central Andes: Controls on mountain glaciation and paleoclimate implications: *Journal of Geology*, v. 110, p. 211-226.
- Hauser, A., 1983, Rodados multicolores: su distribución y características en el sur de Chile: *Revista Geológica de Chile*, v. 27, p. 69-83.
- Hauser, A., 1970, Geología, Estudio integrado de los recursos naturales de la provincia de Cautín, Volume 2, Inst. Rec. Nat. (IREN), p. 72.
- Hebbeln, D., Lamy, F., Mohtadi, M., and Echtler, H., 2007, Tracing the impact of glacial-interglacial climate variability on erosion of the southern Andes: *Geology*, v. 35, p. 131-134.
- Heimsath, A.M., Dietrich, W.E., Nishiizumi, K., and Finkel, R.C., 1997, The soil production function and landscape equilibrium: *Nature*, v. 388, p. 358-361.
- Heintz, M., Debayle, E., and Vauchez, A., 2005, Upper mantle structure of the South American continent and neighboring oceans from surface wave tomography: *Tectonophysics*, v. 406, p. 115-139.
- Heisinger, B.P., 1998, Myonen-induzierte Produktion von Radionukliden: München, TU München.
- Hervé, F., Faundex, V., Calderón, M., Massonne, H.-J., and Willner, A.P., 2007, Metamorphic and plutonic basement complexes, in Moreno, T., and Gibbons, W., eds., *The Geology of Chile*, Geological Society, p. 440.
- Hervé, A.F., 1994, The Southern Andes between 39° and 44°S latitude: The geological signature of a transpressive tectonic regime related to a magmatic arc, in Reutter, K.J., Scheuber, E., and Wigger, P.J., eds., *Tectonics of the Southern Central Andes*: Berlin, Springer, p. 243-248.
- Hervé, A.F., 1988, Late Paleozoic subduction and accretion in southern Chile: *Episodes*, v. 11.
- Hervé, F., 1977, Petrology of the crystalline basement of the Nahuelbuta Mountains, south-central Chile, in Ishikawa, K., and Aguirre Le-Bert, L., eds., *Comparative studies on the geology of the circumpacific orogenic belt in Japan and Chile*: Tokyo, Japan Society for the Promotion of Science, p. 1-51.
- Heusser, C.J., 1989, Southern Westerlies during the last glacial maximum: *Quaternary Research*, v. 31, p. 423-425.

- Hofmann, H.J., Beer, J., Bonani, G., Vongunten, H.R., Raman, S., Suter, M., Walker, R.L., Wolfli, W., and Zimmermann, D., 1987,  $^{10}\text{Be}$  half-life and AMS-standards: Nuclear Instruments and Methods in Physics Research Section B-Beam Interactions with Materials and Atoms, v. 29, p. 32-36.
- Hoke, G.D., Isacks, B.L., Jordan, T.E., Blanco, N., Tomlinson, A.J., and Ramezani, J., 2007, Geomorphic evidence for post-10 Ma uplift of the western flank of the central Andes 18°30'-22°S: Tectonics, v. 26.
- Hsu, J.T., 1992, Quaternary uplift of the Peruvian coast related to the subduction of the Nazca Ridge: 13.5 to 15.6°S latitude: Quaternary International, v. 15, p. 87-97.
- Huntley, D.J., and Baril, M.R., 1998, The K content of the K-feldspars being measured in optical dating or in thermoluminescence dating: Ancient TL, v. 15, p. 11-13.
- Illies, H., 1967, Randpazifische Tektonik und Vulkanismus im südlichen Chile: Geologische Rundschau, v. 57, p. 81-101.
- Isacks, B., 1988, Uplift of the Central Andean Plateau and bending of the Bolivian Orocline: Journal of Geophysical Research, v. 93, p. 3211-3231.
- Ishibashi, K., 1992, Recurrence history of great subduction zone earthquakes along the Sagami and Suruga-Nankai troughs, Japan, and its tectonic implication, preprint, p. 11.
- Jenny, B., Valero-Garces, B.L., Villa-Martinez, R., Urrutia, R., Geyh, M., and Veit, H., 2002, Early to mid-Holocene aridity in central Chile and the southern Westerlies: The Laguna Aculeo record (34°S): Quaternary Research, v. 58, p. 160-170.
- Jenson, S.K., and Domingue, J.O., 1988, Extracting topographic structure from digital elevation data for geographic-information-system analysis: Photogrammetric Engineering and Remote Sensing, v. 54, p. 1593-1600.
- Jordan, T.E., Burns, W.M., Veiga, R., Pangaro, F., Copeland, P., Kelley, S., and Mpodozis, C., 2001, Extension and basin formation in the southern Andes caused by increased convergence rate: a mid-Cenozoic trigger for the Andes: Tectonics, v. 20, p. 308-324.
- Jordan, T.E., 1993, Chronology of motion in a complete thrust belt: the Precordillera, 30-31°S, Andes Mountains: Journal of Geology, v. 101, p. 135-156.
- Jordan, T.E., and Allmendinger, R.W., 1986, The Sierras Pampeanas of Argentina - a modern analog of Rocky-Mountain foreland deformation: American Journal of Science, v. 286, p. 737-764.
- Jordan, T.E., Bryan, L.I., Allmendinger, R.W., Brewer, J.A., Ramos, V.A., and Ando, C.J., 1983, Andean tectonics related to geometry of subducted Nazca plate: Geological Society of America Bulletin, v. 94, p. 341-361.
- Kaizuka, S., Matsuda, T., Nogami, M., and Yonekura, N., 1973, Quaternary tectonic and recent seismic crustal movements in the Arauco Peninsula and its environs, central Chile, Geographical Report (8): Tokyo, Tokyo Metropolitan University, p. 1-49.
- Katz, H.R., 1963, Erdölgeologische Untersuchungen im chilenischen Längstal: Erdöl und Kohle, v. 16, p. 1089-1094.

- Kay, S.M., and Mpodozis, C., 2002, Magmatism as a probe to the Neogene shallowing of the Nazca plate beneath the modern Chilean flat-slab: *Journal of South American Earth Sciences*, v. 15, p. 39-57.
- Kelleher, J.A., 1972, Rupture zones of large South American earthquakes and some predictions: *Journal of Geophysical Research*, v. 77, p. 2087-2107.
- Kelm, U., Cisternas, M.E., Helle, S., and Mendez, D., 1994, Diagenetic character of the Tertiary basin between Los Angeles and Osorno, southern Chile: *Revista Geologica de Chile*, v. 21, p. 241-252.
- Kendrick, E., Bevis, M., Smalley, R., Brooks, B., Vargas, R.B., Lauria, E., and Fortes, L.P.S., 2003, The Nazca South America Euler vector and its rate of change: *Journal of South American Earth Sciences*, v. 16, p. 125-131.
- Khazaradze, G., and Klotz, J., 2003, Short- and long-term effects of GPS measured crustal deformation rates along the south central Andes: *Journal of Geophysical Research-Solid Earth*, v. 108.
- Kirby, E., and Whipple, K., 2001, Quantifying differential rock-uplift rates via stream profile analysis: *Geology*, v. 29, p. 415-418.
- Kley, J., Monaldi, C.R., and Salfity, J.A., 1999, Along-strike segmentation of the Andean foreland: causes and consequences: *Tectonophysics*, v. 301, p. 75-94.
- Kley, J., and Monaldi, C.R., 1998, Tectonic shortening and crustal thickness in the Central Andes: How good is the correlation? *Geology*, v. 26, p. 723-726.
- Klotz, J., Khazaradze, G., Angermann, D., Reigber, C., Perdomo, R., and Cifuentes, O., 2001, Earthquake cycle dominates contemporary crustal deformation in central and southern Andes: *Earth and Planetary Science Letters*, v. 193, p. 437-446.
- Kober, F., Ivy-Ochs, S., Leya, I., Baur, H., Magna, T., Wieler, R., and Kubik, P.W., 2005, In situ cosmogenic  $^{10}\text{Be}$  and  $^{21}\text{Ne}$  in sanidine and in situ cosmogenic  $^3\text{He}$  in Fe-Ti-oxide minerals: *Earth and Planetary Science Letters*, v. 236, p. 404-418.
- Kohl, C.P., and Nishiizumi, K., 1992, Chemical isolation of quartz for measurement of in situ-produced cosmogenic nuclides: *Geochimica et Cosmochimica Acta*, v. 56, p. 3583-3587.
- Krawczyk, C.M., and SPOC-Team, 2003, Amphibious seismic survey images plate interface at 1960 Chile earthquake, AGU Fall Meeting, EOS. Trans. AGU 84 (32/301), p. 304-305.
- Krbetschek, M.R., Götze, J., Dietrich, A., and Trautmann, T., 1997, Spectral information from minerals relevant for luminescence dating: *Radiation Measurements*, v. 27, p. 695-748.
- Kummerow, C., Simpson, J., Thiele, O., Barnes, W., Chang, A.T.C., Stocker, E., Adler, R.F., Hou, A., Kakar, R., Wentz, F., Ashcroft, P., Kozu, T., Hong, Y., Okamoto, K., Iguchi, T., Kuroiwa, H., Im, E., Haddad, Z., Huffman, G., Ferrier, B., Olson, W.S., Zipser, E., Smith, E.A., Wilheit, T.T., North, G., Krishnamurti, T., and Nakamura, K., 2000, The status of the Tropical Rainfall Measuring Mission (TRMM) after two years in orbit: *Journal of Applied Meteorology*, v. 39, p. 1965-1982.

- Lagabrielle, Y., Guivel, C., Maury, R.C., Bourgois, J., Fourcade, S., and Martin, H., 2000, Magmatic-tectonic effects of high thermal regime at the site of active ridge subduction: the Chile triple junction model: *Tectonophysics*, v. 326, p. 255-268.
- Lal, D., 1991, Cosmic ray labeling of erosion surfaces: in situ nuclide production rates and erosion models: *Earth And Planetary Science Letters*, v. 104, p. 424-439.
- Lal, D., 1987, Production of  $^3\text{He}$  in terrestrial rocks: *Chemical Geology*, v. 66, p. 89-98.
- Lal, D., and Peters, B., 1967, Cosmic-ray-produced radioactivity on the Earth, *Handbuch der Physik: Berlin, Springer Verlag*, p. 551-612.
- Lallemand, S.E., Schnurle, P., and Malavieille, J., 1994, Coulomb theory applied to accretionary and non-accretionary wedges - possible causes for tectonic erosion and or frontal accretion: *Journal of Geophysical Research-Solid Earth*, v. 99, p. 12033-12055.
- Lamb, S.H., and Davis, P., 2003, Cenozoic climate change as a possible cause for the rise of the Andes: *Nature*, v. 425, p. 792-797.
- Lamothe, M., Auclair, M., Hamzaoui, C., and Huot, S., 2003, Towards a prediction of long-term anomalous fading of feldspar IRSL: *Radiation Measurements*, v. 37, p. 493-498.
- Lamy, F., Klump, J., Hebbeln, D., and Wefer, G., 2000, Late Quaternary rapid climate change in northern Chile: *Terra Nova*, v. 12, p. 8-13.
- Lamy, F., 1999, High-resolution marine record of climatic change in mid-latitude Chile during the last 28,000 years based on terrigenous sediment parameters: *Quaternary Research*, v. 51, p. 83-93.
- Lamy, F., Hebbeln, D., and Wefer, G., 1998, Late quaternary precessional cycles of terrigenous sediment input off the Norte Chico, Chile (27.5°S) and palaeoclimatic implications: *Palaeogeography Palaeoclimatology Palaeoecology*, v. 141, p. 233-251.
- Laursen, J., Scholl, D.W., and von Huene, R., 2002, Neotectonic deformation of the central Chile margin: Deepwater forearc basin formation in response to hot spot ridge and seamount subduction: *Tectonics*, v. 21.
- Lavenu, A., and Cembrano, J., 1999, Compressional- and transpressional stress pattern for Pliocene and Quaternary brittle deformation in fore-arc and intra-arc zones (Andes of Central and Southern Chile): *Journal of Structural Geology*, v. 21, p. 1669-1691.
- Lay, T., Kanamori, H., and Ruff, L., 1982, The asperity model and the nature of large subduction zone earthquakes: *Earthquake Prediction Research*, v. 1, p. 3-71.
- Le Roux, J.P., Olivares, D.M., Nielsen, S.N., Smith, N.D., Middleton, H., Fenner, J., and Ishman, S.E., 2006, Bay sedimentation as controlled by regional crustal behavior, local tectonics, and eustatic sea-level changes: Coquimbo Formation (Miocene-Pliocene), Bay of Tongoy, central Chile: *Sedimentary Geology*, v. 184, p. 133-153.

- Le Roux, J.P., Gómez, C., Venegas, C., Fenner, J., Middleton, H., Marchant, M., Buchbinder, B., Frassinetti, D., Marquardt, C., Gregory-Wodzicki, K.M., and Lavenu, A., 2005, Neogene-Quaternary coastal and offshore sedimentation in north central Chile: Record of sea-level changes and implications for Andean tectonism: *Journal of South American Earth Sciences*, v. 19, p. 83-89.
- Lee, K., and Yang, W.S., 2006, Historical seismicity of Korea: *Bulletin of the Seismological Society of America*, v. 96, p. 846-855.
- Licciardi, J.M., Kurz, M.D., Clark, P.U., and Brook, E.J., 1999, Calibration of cosmogenic  $^3\text{He}$  production rates from Holocene lava flows in Oregon, USA, and effects of the Earth's magnetic field: *Earth and Planetary Science Letters*, v. 172, p. 261-271.
- Lohrmann, J., 2002, Identification of parameters controlling the accretive and tectonically erosive mass-transfer mode at the south-central and north Chilean forearc using scaled 2D sandbox experiments [Scientific Technical Report 02/10, PhD thesis], GeoForschungsZentrum Potsdam.
- Lomnitz, C., 2004, Major earthquakes of Chile: A historical survey, 1535-1960: *Seismological Research Letters*, v. 75, p. 368-378.
- Lomnitz, C., 1970, Some observations of gravity waves in 1960 Chile earthquake: *Bulletin of the Seismological Society of America*, v. 60, p. 669-670.
- Machare, J., and Ortlieb, L., 1992, Plio-Quaternary vertical motions and the subduction of the Nazca Ridge, central coast of Peru: *Tectonophysics*, v. 205, p. 97-108.
- Machette, M.N., Personius, S.F., Nelson, A.R., Schwartz, D.P., and Lund, W.R., 1991, The Wasatch fault zone, Utah: segmentation and history of Holocene earthquakes: *Journal of Structural Geology*, v. 13, p. 137-149.
- Mann, P., Taylor, F.W., Lagoe, M.B., Quarles, A., and Burr, G., 1998, Accelerating late Quaternary uplift of the New Georgia Island Group (Solomon island arc) in response to subduction of the recently active Woodlark spreading center and Coleman seamount: *Tectonophysics*, v. 295, p. 259-306.
- Mardones, M., 2006, Pers. comm.
- Mardones, M., and Reuther, C.D., 1999, Geomorphological aspects of the drainage pattern around Lake Lanalhue and Lake Lleulleu in the active convergent margin setting of south-central Chile, *Mitteilungen des Geologischen Instituts* (83), Universität Hamburg, p. 75-88.
- Marquardt, C., Lavenu, A., Ortlieb, L., Godoy, E., and Comte, D., 2004, Coastal neotectonics in southern central Andes: uplift and deformation of marine terraces in northern Chile (27°S): *Tectonophysics*, v. 394, p. 193-219.
- Masarik, J., and Wieler, R., 2003, Production rates of cosmogenic nuclides in boulders: *Earth and Planetary Science Letters*, v. 216, p. 201-208.
- Masarik, J., 2002, Numerical simulation of in-situ production of cosmogenic nuclides: *Geochimica et Cosmochimica Acta*, v. 66, p. A491-A491.

- McCaffrey, R., 1994, Global variability in subduction thrust zone forearc systems: Pure and Applied Geophysics, v. 142, p. 173-224.
- McCaffrey, R., 1993, On the role of the upper plate in great subduction zone earthquakes: *Journal of Geophysical Research - Solid Earth*, v. 98, p. 11953-11966.
- McCann, W.R., and Habermann, R.E., 1989, Morphologic and geologic effects of the subduction of bathymetric highs: *Pure and Applied Geophysics*, v. 129, p. 41-69.
- McKean, J., Dietrich, W.E., Finkel, R.C., Southon, J.R., and Caffee, M.C., 1993, Quantification of soil production and downslope creep rates from cosmogenic <sup>10</sup>Be accumulations on a hillslope profile: *Geology*, v. 21, p. 343-346.
- Melnick, D., Bookhagen, B., Echtler, H.P., and Strecker, M.R., 2006, Coastal deformation and great subduction earthquakes, Isla Santa María, Chile (37°S): *Geological Society of America Bulletin*, v. 118, p. 1463-1480.
- Melnick, D., and Echtler, H., 2006a, Inversion of forearc basins in south-central Chile caused by rapid glacial age trench fill: *Geology*, v. 34, p. 709-712.
- Melnick, D., and Echtler, H.P., 2006b, Morphotectonic and geologic digital map compilations of the south-central Andes (36°-42°S), in Oncken, O., Chong, G., Franz, G., Giese, P., Götze, H.-J., Ramos, V.A., Strecker, M., and Wigger, P., eds., *The Andes - Active Subduction Orogeny: Frontiers in Earth Sciences*: Berlin Heidelberg New York, Springer-Verlag, p. 565-568.
- Melnick, D., Bookhagen, B., Echtler, H., and Strecker, M., 2005, Active shortening, surface deformation and late Neogene coastal geomorphology of the Arauco Region, Chile, 6th International Symposium on Andean Geodynamic: Barcelona, p. 502-503.
- Mercer, J.H., and Sutter, J.F., 1982, Late Miocene - earliest Pliocene glaciation in southern Argentina: Implications for global ice-sheet history: *Palaeogeography Palaeoclimatology Palaeoecology*, v. 38, p. 185-206.
- Mercer, J.H., 1976, Glacial history of southernmost South America: *Quaternary Research*, v. 6, p. 125-166.
- Mitchell, A.H., and Reading, H.G., 1969, Continental margins, geosynclines, and ocean-floor spreading: *Journal of Geology*, v. 77, p. 629.
- Mitchell, S.G., and Montgomery, D.R., 2006, Influence of a glacial buzzsaw on the height and morphology of the Cascade Range in central Washington State, USA: *Quaternary Research*, v. 65, p. 96-107.
- Mogi, K., 1969, Relationship between the occurrence of great earthquakes and tectonic structures: *Bulletin Earthquake Research Institute*, v. 47, p. 429-441.
- Molin, P., Pazzaglia, F.J., and Dramis, F., 2004, Geomorphic expression of active tectonics in a rapidly deforming forearc, Sila Massif, Calabria, southern Italy: *American Journal of Science*, v. 304, p. 559-589.
- Molnar, P., and England, P., 1990, Late Cenozoic uplift of mountain-ranges and global climate change - chicken or egg: *Nature*, v. 346, p. 29-34.

- Monaghan, M.C., McKean, J., Dietrich, W., and Klein, J., 1992,  $^{10}\text{Be}$  chronometry of bedrock-to-soil conversion rates: *Earth and Planetary Science Letters*, v. 111, p. 483-492.
- Montgomery, D.R., and Brandon, M.T., 2002, Topographic controls on erosion rates in tectonically active mountain ranges: *Earth And Planetary Science Letters*, v. 201, p. 481-489.
- Montgomery, D.R., Balco, G., and Willett, S.D., 2001, Climate, tectonics, and the morphology of the Andes: *Geology*, v. 29, p. 579-582.
- Mordojovich, C., 1981, Sedimentary basins of Chilean Pacific offshore, in Halbouty, M.T., ed., *American Association of Petroleum Geologists Studies in Geology, Volume Energy resources of the Pacific region (12)*, p. 63-82.
- Moreno, M., Klotz, J., Melnick, D., Grund, V., Echtler, H., and Bataille, K., submitted, Active faulting and forearc block rotation in south-central Chile from GPS-derived deformation ( $36^{\circ}$ - $39^{\circ}\text{S}$ ).
- Moreno, T., and Gibbons, W., 2007, *The geology of Chile*, The Geological Society, 440 p.
- Morrison, P., and Pine, J., 1955, Radiogenic origin of the helium isotopes in rock: *Annals of the New York Academy of Sciences*, v. 62, p. 69-92.
- Mpodozis, C., and Ramos, V.A., 1989, The Andes of Chile and Argentina., in Ericksen, G., Canas Pinochet, M., and Reinemund, J., eds., *Geology of the Andes and its relation to hydrocarbon and mineral resources, Volume 11: Earth Science Series - Circum-Pacific Council of Energy and Mineral Resources: Houston TX*, p. 59-89.
- Muhs, D.R., Kelsey, H.M., Miller, G.H., Kennedy, G.L., Whelan, J.F., and McInelly, G.W., 1990, Age estimates and uplift rates for late Pleistocene marine terraces - southern Oregon portion of the Cascadia forearc: *Journal of Geophysical Research-Solid Earth And Planets*, v. 95, p. 6685-6698.
- Muñoz-Cristi, J., 1960, Contribución al conocimiento geológico de la Cordillera de la Costa de la Zona Central: *Minerales*, v. 15, p. 28-46.
- Muñoz, J., Troncoso, R., Duhart, P., Crignola, P., Farmer, L., and Stern, C.R., 2000, The relation of the mid-Tertiary coastal magmatic belt in south-central Chile to the late Oligocene increase in plate convergence: *Revista Geologica de Chile*, v. 27, p. 177-203.
- Murray, A.S., and Wintle, A.G., 2000, Application of the single-aliquot regenerative-dose protocol to the  $375^{\circ}\text{C}$  quartz TL signal: *Radiation Measurements*, v. 32, p. 579-583.
- NEIC, 2006, <http://neic.usgs.gov/>, National Earthquake Information Center.
- Nelson, A.R., and Manley, W.F., 1992, Holocene coseismic and aseismic uplift of Isla Mocha, south-central Chile. Impacts of tectonics on Quaternary coastal evolution: *Quaternary International*, v. 15-16, p. 61-76.
- New, M., Lister, D., Hulme, M., and Makin, I., 2002, A high-resolution data set of surface climate over global land areas: *Climate Research*, v. 21, p. 1-25.

- Niedermann, S., 2002, Cosmic-ray-produced noble gases in terrestrial rocks: Dating tools for surface processes, *Noble Gases in Geochemistry and Cosmochemistry*, Volume 47: Reviews In Mineralogy & Geochemistry, p. 731-784.
- Niedermann, S., Bach, W., and Erzinger, J., 1997, Noble gas evidence for a lower mantle component in MORBs from the southern East Pacific Rise: decoupling of helium and neon isotope systematics: *Geochimica et Cosmochimica Acta*, v. 61, p. 2697-2715.
- Niedermann, S., Graf, T., Kim, J.S., Kohl, C.P., Marti, K., and Nishiizumi, K., 1994, Cosmic-ray produced  $^{21}\text{Ne}$  in terrestrial quartz - the neon inventory of Sierra-Nevada quartz separates: *Earth and Planetary Science Letters*, v. 125, p. 341-355.
- Niedermann, S., Graf, T., and Marti, K., 1993, Mass-spectrometric identification of cosmic-ray-produced neon in terrestrial rocks with multiple neon components: *Earth and Planetary Science Letters*, v. 118, p. 65-73.
- Nishiizumi, K., Caffee, M.W., Finkel, R.C., Brimhall, G., and Mote, T., 2005, Remnants of a fossil alluvial fan landscape of Miocene age in the Atacama Desert of northern Chile using cosmogenic nuclide exposure age dating: *Earth and Planetary Science Letters*, v. 237, p. 499-507.
- Nishiizumi, K., Kohl, C.P., Arnold, J.R., Klein, J., Fink, D., and Middleton, R., 1991, Cosmic-ray produced  $^{10}\text{Be}$  and  $^{26}\text{Al}$  in Antarctic rocks - exposure and erosion history: *Earth and Planetary Science Letters*, v. 104, p. 440-454.
- Nishiizumi, K., Winterer, E.L., Kohl, C.P., Klein, J., Middleton, R., Lal, D., and Arnold, J.R., 1989, Cosmic-ray production rates of  $^{10}\text{Be}$  and  $^{26}\text{Al}$  in quartz from glacially polished rocks: *Journal of Geophysical Research-Solid Earth and Planets*, v. 94, p. 17907-17915.
- Norris, T.L., Gancarz, A.J., Rokop, D.J., and Thomas, K.W., 1983, Half-life of  $^{26}\text{Al}$ : *Journal of Geophysical Research*, v. 88, p. B331-B333.
- O'Callaghan, J., and Mark, D.M., 1984, The extraction of drainage networks from digital elevation data: *Computer Vision Graphics and Image Processing*, v. 28, p. 323-344.
- Ohmori, H., 1993, Changes in the hypsometric curve through mountain building resulting from concurrent tectonics and denudation: *Geomorphology*, v. 8, p. 263-277.
- Oleskevich, D.A., Hyndman, R.D., and Wang, K., 1999, The updip and downdip limits to great subduction earthquakes: Thermal and structural models of Cascadia, south Alaska, SW Japan, and Chile: *Journal of Geophysical Research*, v. 104, p. 14965-14991.
- Oncken, O., Hindle, D., Kley, J., Elger, K., Victor, V., and Schemmann, K., 2006, Deformation of the Central Andean upper plate system - facts, fiction, and constraints for plateau models, in Oncken, O., Chong, G., Frank, G., Giese, P., Götze, H.-J., Ramos, V.A., Strecker, M.R., and Wigger, P., eds., *The Andes - active subduction orogeny*, Volume 1: *Frontiers in Earth Science Series*: Berlin Heidelberg New York, Springer-Verlag.

- Ortlieb, L., Diaz, A., and Guzman, N., 1996a, A warm interglacial episode during oxygen isotope stage 11 in northern Chile: *Quaternary Science Reviews*, v. 15, p. 857-871.
- Ortlieb, L., Zazo, C., Goy, J.L., HillaireMarcel, C., Ghaleb, B., and Cournoyer, L., 1996b, Coastal deformation and sea-level changes in the northern Chile subduction area (23°S) during the last 330 ky: *Quaternary Science Reviews*, v. 15, p. 819-831.
- Pankhurst, R.J., and Hervé, F., 2007, Introduction and overview, in Moreno, T., and Gibbons, W., eds., *The geology of Chile*, The Geological Society, p. 440.
- Parada, M.A., López-Escobar, L., Oliveros, V., Fuentes, F., Morata, D., Calderón, M., Aguirre, L., Féraud, G., Espinoza, F., Moreno, H., Figueroa, O., Muñoz Bravo, J., Troncoso Vásquez, R., and Stern, C.R., 2007, Andean magmatism, in Moreno, T., and Gibbons, W., eds., *The geology of Chile*: London, Geological Society, p. 440.
- Parada, M.A., 1990, Granitoid plutonism in central Chile and its geodynamic implications: a review, *Plutonism from Antarctica to Alaska*, Volume 241: Boulder CO, Geological Society of America, p. 51-66.
- Pazzaglia, F.J., and Brandon, M.T., 2001, A fluvial record of long-term steady-state uplift and erosion across the Cascadia forearc high, western Washington State: *American Journal of Science*, v. 301, p. 385-431.
- Pineda, V., 1986, Evolución paleogeográfica de la cuenca sedimentaria Cretácico-Terciaria de Arauco, in Frutos, J., Oyarzún, R., and Pincheira, M., eds., *Geología y Recursos Minerales de Chile*, Volume Tomo 1: Concepción, Universidad de Concepción, p. 375-390.
- Pino, M., and Navarro, R.X., 2005, Geoarqueología del sitio arcaico Chan-Chan 18, costa de Valdivia: Discriminación de ambientes de ocupación humana y su relación con la transgresión marina del Holoceno Medio: *Revista Geológica de Chile*, v. 32, p. 59-75.
- Plafker, G., and Savage, J.C., 1970, Mechanism of the Chilean earthquakes of May 21 and 22, 1960: *Geological Society of America Bulletin*, v. 81, p. 1001-1030.
- Preusser, F., Degering, D., Fuchs, M., Hilgers, A., Kadereit, A., Klasen, N., Krbetschek, M., Richter, D., and Spencer, J., in press, Luminescence dating: Basics, methods, and applications: *Quaternary Science Journal*.
- Preusser, F., and Kasper, H.U., 2001, Comparison of dose rate determination using high-resolution gamma spectrometry and inductively coupled plasma-mass spectrometry: *Ancient TL*, v. 19, p. 19-23.
- Rabassa, J., Coronato, A.M., and Salemme, M., 2005, Chronology of the late Cenozoic Patagonian and their correlation with biostratigraphic glaciations units of the Pampean region (Argentina): *Journal of South American Earth Sciences*, v. 20, p. 81-103.
- Rabassa, J., and Clapperton, C.M., 1990, Quaternary glaciations of the southern Andes: *Quaternary Science Reviews*, v. 9, p. 153-174.

- Radtke, U., 1989, Marine Terrassen und Korallenriffe - Das Problem der quartären Meeresspiegelschwankungen erläutern an Fallstudien aus Chile, Argentinien und Barbados, *Düsseldorfer Geographische Schriften*, Heinrich-Heine-Universität, p. 245.
- Ramos, V.A., Cristallini, E.O., and Perez, D.J., 2002, The Pampean flat-slab of the Central Andes: *Journal of South American Earth Sciences*, v. 15, p. 59-78.
- Rech, J.A., Currie, B.S., Michalski, G., and Cowan, A.M., 2006, Neogene climate change and uplift in the Atacama Desert, Chile: *Geology*, v. 34, p. 761-764.
- Rehak, K., Strecker, M.R., and Echtler, H.P., 2008, Morphotectonic segmentation of an active forearc, 37°-41°S, Chile: *Geomorphology*, v. 94, p. 98-116.
- Rehak, K., Strecker, M.R., Echtler, H.P., Binnie, S., Summerfield, M.A., Dunai, T.J., and Freeman, S., in review, Reconstructing the uplift of the Coastal Cordillera in south-central Chile using cosmogenic nuclides dating: *Earth Surface Processes and Landforms*.
- Reiners, P.W., Ehlers, T.A., Mitchell, S.G., and Montgomery, D.R., 2003, Coupled spatial variations in precipitation and long-term erosion rates across the Washington Cascades: *Nature*, v. 426, p. 645-647.
- Repka, J.L., Anderson, R.S., and Finkel, R.C., 1997, Cosmogenic dating of fluvial terraces, Fremont River, Utah: *Earth And Planetary Science Letters*, v. 152, p. 59-73.
- Riebe, C.S., Kirchner, J.W., and Granger, D.E., 2001, Quantifying quartz enrichment and its consequences for cosmogenic measurements of erosion rates from alluvial sediment and regolith: *Geomorphology*, v. 40, p. 15-19.
- Roe, G.H., 2003, Orographic precipitation and the relief of mountain ranges: *Journal of Geophysical Research-Solid Earth*, v. 108.
- Roe, G.H., Montgomery, D.R., and Hallet, B., 2002, Effects of orographic precipitation variations on the concavity of steady-state river profiles: *Geology*, v. 30, p. 143-146.
- Romero, O.E., J.-H., K., and Hebbeln, D., 2006, Paleoproductivity evolution off central Chile from the last glacial maximum to the early Holocene: *Quaternary Research*, v. 65, p. 519-525.
- Rosenau, M., Melnick, D., and Echtler, H., 2006, Kinematic constraints on intra-arc shear and strain partitioning in the southern Andes between 38°S and 42°S latitude: *Tectonics*, v. 25, p. TC4013.
- Rosenau, M., 2004, Tectonic and geomorphic evolution of the southern Andean intra-arc zone between latitudes 38° and 42°S [PhD thesis]: Berlin, Freie Universität.
- Ruff, L., 1989, Introduction to subduction zones: *Pure and Applied Geophysics*, v. 129, p. 1-5.
- Ruff, L., and Kanamori, H., 1980, Seismicity and the subduction process: *Physics of the Earth and Planetary Interiors*, v. 23, p. 240-252.

- Ryan, H.F., and Scholl, D.W., 1993, Geologic implications of great interplate earthquakes along the Aleutian arc: *Journal of Geophysical Research-Solid Earth*, v. 98, p. 22135-22146.
- Ryan, J.G., and Kyle, P.R., 2004, Lithium abundance and lithium isotope variations in mantle sources: insights from intraplate volcanic rocks from Ross Island and Marie Byrd Land (Antarctica) and other oceanic islands: *Chemical Geology*, v. 212, p. 125-142.
- Schäfer, J.M., Ivy-Ochs, S., Wieler, R., Leya, J., Baur, H., Denton, G.H., and Schluchter, C., 1999, Cosmogenic noble gas studies in the oldest landscape on earth: surface exposure ages of the Dry Valleys, Antarctica: *Earth and Planetary Science Letters*, v. 167, p. 215-226.
- Schildgen, T.F., Hodges, K.V., Whipple, K.X., Reiners, P.W., and Pringle, M.S., 2007, Uplift of the western margin of the Andean plateau revealed from canyon incision history, southern Peru: *Geology*, v. 35, p. 523-526.
- Scholl, D.W., Christen, M., von Huene, R., and Marlow, M.S., 1970, Peru-Chile trench sediments and sea-floor spreading: *Geological Society of America Bulletin*, v. 81, p. 1339.
- Schwerdtfeger, W., 1976, *Climates of Central and South America*, Elsevier.
- Servicio Nacional de Geología y Minería, 2003, *Mapa geológico de Chile*: Talleres Gráficos Instituto Geográfico Militar.
- Seitz, H.M., Brey, G.P., Lahaye, Y., Durali, S., and Weyer, S., 2004, Lithium isotopic signatures of peridotite xenoliths and isotopic fractionation at high temperature between olivine and pyroxenes: *Chemical Geology*, v. 212, p. 163-177.
- Sernageomin, 2003, *Mapa geológico de Chile, 1 : 1000000*, Servicio Nacional de Geología y Minería, Chile.
- Small, E.E., and Anderson, R.S., 1998, Pleistocene relief production in Laramide mountain ranges, western United States: *Reply: Geology*, v. 26, p. 1151-1152.
- Snyder, N.P., Whipple, K.X., Tucker, G.E., and Merritts, D.J., 2000, Landscape response to tectonic forcing: Digital elevation model analysis of stream profiles in the Mendocino triple junction region, northern California: *Geological Society of America Bulletin*, v. 112, p. 1250-1263.
- Somoza, R., 1998, Updated Nazca (Farallon) - South America relative motions during the last 40 My: implications for mountain building in the central Andean region: *Journal of South American Earth Sciences*, v. 11, p. 211-215.
- Song, T.-R.A., and Simons, M., 2003, Large trench-parallel gravity variations predict seismogenic behavior in subduction zones: *Science*, v. 301, p. 630-633.
- Stone, J.O., 2000, Air pressure and cosmogenic isotope production: *Journal of Geophysical Research-Solid Earth*, v. 105, p. 23753-23759.
- Stone, J.O., 1999, A consistent  $^{10}\text{Be}$  production rate in quartz - muons and altitude scaling, AMS-8, Volume 8: *Proceedings Abstract Volume*: Vienna.

- Strahler, A.N., 1957, Quantitative analysis of watershed geomorphology, Volume 38: American Geophysical Union Transactions, p. 913-920.
- Strahler, A.N., 1952, Hypsometric (area-altitude) Analysis of erosional topography: Geological Society of America Bulletin, v. 63, p. 1117.
- Suárez, M.D., and Emparan, C., 1997, Hoja Curacautin - Regiones de la Araucania y del Bio-Bío: Santiago, Servicio Nacional de Geología y Minería, p. 105.
- Summerfield, M.A., 1991, Global Geomorphology: Essex, Addison Wesley Longman, 537 p.
- Sykes, L.R., and Nishenko, S.P., 1984, Probabilities of occurrence of large plate rupturing earthquakes for the San-Andreas, San-Jacinto, and Imperial Faults, California, 1983-2003: Journal of Geophysical Research, v. 89, p. 5905-5927.
- Tarboton, D.G., Bras, R.L., and Rodrigueziturbe, I., 1991, On the extraction of channel networks from digital elevation data: Hydrological Processes, v. 5, p. 81-100.
- Tašárová, Z., 2004, Gravity data analysis and interdisciplinary 3D modelling of a convergent plate margin (Chile, 36-42°S) [PhD thesis], Freie Universität Berlin.
- Tassara, A., Gotze, H.J., Schmidt, S., and Hackney, R., 2006, Three-dimensional density model of the Nazca plate and the Andean continental margin: Journal of Geophysical Research-Solid Earth, v. 111.
- Taylor, F.W., Mann, P., Bevis, M.G., Edwards, R.L., Cheng, H., Cutler, K.B., Gray, S.C., Burr, G.S., Beck, J.W., Phillips, D.A., Cabioch, G., and Recy, J., 2005, Rapid forearc uplift and subsidence caused by impinging bathymetric features: Examples from the New Hebrides and Solomon arcs: Tectonics, v. 24.
- Taylor, F.W., Frohlich, C., Lecolle, J., and Strecker, M., 1987, Analysis of partially emerged corals and reef terraces in the central Vanuatu arc - comparison of contemporary coseismic and nonseismic with Quaternary vertical movements: Journal of Geophysical Research - Solid Earth, v. 92, p. 4905-4933.
- Tebbens, S.F., and Cande, S.C., 1997, Southeast Pacific tectonic evolution from early Oligocene to present: Journal of Geophysical Research - Solid Earth, v. 102, p. 12061-12084.
- Thomson, S.N., 2002, Late Cenozoic geomorphic and tectonic evolution of the Patagonian Andes between latitudes 42°S and 46°S: An appraisal based on fission-track results from the transpressional intra-arc Liquine-Ofqui fault zone: Geological Society of America Bulletin, v. 114, p. 1159-1173.
- Tomkin, J.H., and Braun, J., 2002, The influence of alpine glaciation on the relief of tectonically active mountain belts: American Journal Of Science, v. 302, p. 169-190.
- TRMM, 2007, Tropical Rainfall Measurement Mission: NASA.
- Tucker, G.E., and Bras, R.L., 1998, Hillslope processes, drainage density, and landscape morphology: Water Resources Research, v. 34, p. 2751-2764.

- Tucker, G.E., and Slingerland, R., 1997, Drainage basin responses to climate change: *Water Resources Research*, v. 33, p. 2031-2047.
- U.S. Soil Taxonomy, 2003
- Veit, H., 1996, Southern Westerlies during the Holocene deduced from geomorphological and pedological studies in the Norte Chico, northern Chile (27-33°S): *Palaeogeography Palaeoclimatology Palaeoecology*, v. 123, p. 107-119.
- Vergara, M., and Munizaga, F., 1974, Age and evolution of the Upper Cenozoic andesitic volcanism in central-south Chile: *Geological Society of America Bulletin*, v. 85, p. 603-606.
- Vietor, T., and Echtler, H., 2006, Episodic Neogene southward growth of the Andean subduction orogen between 30°S and 40°S - plate motions, mantle flow, climate, and upper-plate structure, in Oncken, O., Strecker, M.R., Franz, G., and Götze, H.-J., eds., *The Andes - active subduction orogeny*, Volume *Frontiers in Earth Sciences*: Berlin, Heidelberg, New York, Springer, p. 371-396.
- Vietor, T., Babeyko, A.Y., Echtler, H., Elger, K., Hindle, D., Klotz, J., Kley, J., Riller, U., Sobolev, S.V., Victor, V., Oncken, O., and Group, S.R., 2005, Plate motions, inter- and intraplate strengths control the phases of Andean subduction orogeny, *International Final Symposium of the Collaborative Research Center 'Deformation Processes in the Andes'*: GeoForschungsZentrum Potsdam, SFB 267, p. 6887.
- von Huene, R., and Scholl, D.W., 1991, Concerning sediment subduction, subduction erosion, and the growth of continental crust.: *Reviews of Geophysics*, v. 29, p. 279-316.
- Weischet, W., 1970, *Chile - Seine länderkundliche Individualität und Struktur*: Darmstadt.
- Wells, R.E., Blakely, R.J., Sugiyama, Y., Scholl, D.W., and Dinterman, P.A., 2003, Basin-centered asperities in great subduction zone earthquakes: a link between slip, subsidence, and subduction erosion? *Journal Of Geophysical Research-Solid Earth*, v. 108, p. 2507, doi:10.1029/2002JB002072.
- Wells, S.G., Bullard, T.F., Menges, C.M., Drake, P.G., Karas, P.A., Kelson, K.I., Ritter, J.B., and Wesling, J.R., 1988, Regional variations in tectonic geomorphology along a segmented convergent plate boundary, Pacific coast of Costa Rica: *Geomorphology*, v. 1, p. 239-265.
- Whipple, K., and Tucker, G.E., 1999, Dynamics of stream-power river incision model: Implications for height limits of mountain ranges, landscape response timescales, and research needs: *Journal of Geophysical Research*, v. 104, p. 17661-17674.
- Whipple, K.X., Kirby, E., and Brocklehurst, S.H., 1999, Geomorphic limits to climate-induced increases in topographic relief: *Nature*, v. 401, p. 39-43.
- Willett, S.D., 1999, Orogeny and orography: The effects of erosion on the structure of mountain belts: *Journal of Geophysical Research-Solid Earth*, v. 104, p. 28957-28981.
- Windley, B.F., and Smith, J.V., 1976, Archaean high-grade complexes and modern continental margins: *Nature*, v. 260, p. 671-675.

- Wintle, A.G., and Murray, A.S., 2006, A review of quartz optically stimulated luminescence characteristics and their relevance in single-aliquot regeneration dating protocols: *Radiation Measurements*, v. 41, p. 369-391.
- Wintle, A.G., 1973, Anomalous fading of thermoluminescence in mineral samples: *Nature*, v. 245, p. 143-144.
- Zachos, J., Pagani, H., Sloan, L., Thomas, E., and Billups, K., 2001, Trends, rhythms, and aberrations in global climate 65 Ma to present: *Science*, v. 292, p. 686-693.
- Zaprowski, B.J., Lal, D., Pazzaglia, F.J., and Evenson, E.B., 2005, Climatic influence on profile concavity and river incision: *Journal of Geophysical Research - Earth Surface*, v. 110, p. F03004.
- Zeilinger, G., Schlunegger, F., and Simpson, G., 2005, The Oxaya anticline (northern Chile): a buckle enhanced by river incision? *Terra Nova*, v. 17, p. 368-375.

## Appendix

## Climatic controls on drainage-basin morphology

Variable	Unit	Definition	Source
<b>Vertical shape</b>			
profile concavity		normalized area under the normalized distance-elevation profile (diagonal from source to mouth would be 0.5) PCI > 0.5 reflect a strongly convex profile	after Demoulin, 1998
hypsometric integral		normalized area under a normalized area-elevation curve after Strahler	after Strahler, 1952
<b>Geometry</b>			
basin area	km <sup>2</sup>		
basin length	km	longest distance from outlet	
basin width	km	longest distance perpendicular to basin length	
basin form		basin length/basin width	
basin elongation ratio		diameter of a circle with basin area/basin length	after Schumm, 1956
<b>Relief</b>			
basin mean elevation	m		
total basin relief	m	basin maximum elevation - basin minimum elevation	
basin relief ratio		relief/length * 100	
basin local relief	m	local relief averaged over a circle with a diameter of 10 cells	after Summerfield, 1991
channel slope	m m <sup>-1</sup>	(channel maximum elevation - channel minimum elevation)/channel length	
<b>Climate</b>			
mean annual rainfall	mm a <sup>-1</sup>		TRMM 30km dataset
mean annual temperature	°C		cru-dataset, 10' grid ( <a href="http://www.cru.uea.ac.uk/cru/data/hrg.htm">http://www.cru.uea.ac.uk/cru/data/hrg.htm</a> )
mean annual ground frost	d a <sup>-1</sup>		cru-dataset, 10' grid ( <a href="http://www.cru.uea.ac.uk/cru/data/hrg.htm">http://www.cru.uea.ac.uk/cru/data/hrg.htm</a> )
modern perennial snowline	m		after Schwerdtfeger, 1976; Rabassa and Clapperton, 1990
lowest Pleistocene glacier extent	m		after Schwerdtfeger, 1976; Rabassa and Clapperton, 1990
<b>Erosion</b>			
erosion index		$e = Q^{0.5} * S$ , with Q = mean annual rainfall, S = channel drop	after Finlayson et al., 2002
erosion intensity	km <sup>3</sup> a <sup>-1</sup>	$IE = P * A * S$ , with P = mean annual rainfall, A = drainage area	after Montgomery et al., 2001

Table A 1: Definition and sources of the calculated variables.

basin ID	group	latitude [°]	area [km <sup>2</sup> ]	basin_length [km]	basin_width [km]	basin_form	basin_elongation_ratio	basin_elevation	total_basin_relieft [m]	basin_relieft_ratio	basin_relieft [m]	channel_slope [m m <sup>-1</sup> ]	mean_rainfall [mm a <sup>-1</sup> ]	mean_temperature [°C]	ground_snowline [d a <sup>-1</sup> ]	modern_perennial_snowline [m]	lowest_Pleistocene_glaciers [m]	erosion_index [m a <sup>-1</sup> ]	PCI	HI	
1	Forearc	-20.66	1098	41.09	48.69	0.88	0.91	944	1484	3.64	149	0.0153	224	15.00	46.20	5931	5321	0.0229	0.0377	0.64	0.63
2	Forearc	-21.71	524	42.86	22.27	1.92	0.60	1459	1920	4.48	102	0.0362	377	13.87	62.05	5980	5422	0.0702	0.0714	0.76	0.76
3	Forearc	-22.76	1091	45.19	24.78	1.81	0.58	1340	2680	3.27	185	0.0242	314	14.82	54.39	6005	5614	0.0350	0.0366	0.48	0.48
4	Forearc	-23.70	2091	89.33	43.75	2.02	0.58	1340	2680	3.27	185	0.0242	314	14.82	54.39	6005	5614	0.0350	0.0366	0.48	0.48
5	Forearc	-26.57	2080	89.89	34.84	2.55	0.58	1242	2423	2.73	216	0.0164	94	14.16	65.35	6375	5941	0.0159	0.0321	0.50	0.51
6	Forearc	-28.77	1074	64.66	20.89	3.10	0.57	940	1896	2.93	222	0.0183	89	14.34	50.35	6397	5953	0.0182	0.0184	0.48	0.48
7	Forearc	-28.11	1771	79.59	35.64	2.23	0.60	589	2248	2.62	190	0.0155	38	14.62	35.40	5917	5446	0.0085	0.0104	0.27	0.25
8	Forearc	-29.06	2278	95.26	45.70	2.08	0.57	1075	3288	3.43	236	0.0198	75	13.07	62.46	5395	4874	0.0171	0.0338	0.30	0.33
9	Forearc	-30.65	2894	105.35	52.43	1.93	0.58	1171	3594	3.13	243	0.0244	104	13.68	45.40	5297	4713	0.0106	0.0202	0.42	0.38
10	Forearc	-35.66	391	49.21	24.48	1.72	0.83	318	810	1.30	149	0.0384	724	13.69	55.30	2013	1929	0.0202	0.0202	0.42	0.38
11	Forearc	-37.23	1268	59.29	43.08	1.24	0.75	416	1333	2.50	196	0.0148	104	11.69	66.22	2364	2228	0.0479	0.1960	0.22	0.31
12	Forearc	-37.60	625	50.09	25.90	1.94	0.65	351	1334	2.66	166	0.0104	803	11.93	60.90	2699	2177	0.0296	0.0692	0.14	0.28
13	Forearc	-38.00	1219	45.48	48.17	0.94	0.87	428	1512	3.32	235	0.0124	930	11.43	68.32	2419	2050	0.0377	0.1403	0.20	0.28
14	Forearc	-38.35	398	26.98	24.78	1.15	0.78	390	872	3.05	231	0.0187	629	11.32	62.30	2317	1936	0.0538	0.0999	0.16	0.45
15	Forearc	-38.53	523	35.33	24.74	1.47	0.71	416	1334	2.66	166	0.0104	803	11.93	60.90	2699	2177	0.0296	0.0692	0.14	0.28
16	Forearc	-39.46	523	35.33	24.74	1.47	0.71	416	1334	2.66	166	0.0104	803	11.93	60.90	2699	2177	0.0296	0.0692	0.14	0.28
17	Forearc	-39.96	289	29.00	14.63	1.91	0.68	492	1044	3.73	220	0.0159	654	9.86	67.70	1866	1707	0.0407	0.0300	0.34	0.30
18	Forearc	-40.58	384	34.96	18.59	1.88	0.62	280	803	2.30	174	0.0141	776	9.81	57.70	1864	1363	0.0391	0.0397	0.17	0.35
19	Forearc	-40.72	357	32.97	16.71	1.57	0.65	463	1009	3.06	285	0.0165	779	9.75	56.10	1579	1236	0.0462	0.0460	0.18	0.46
20	Forearc	-40.78	188	23.32	11.41	2.04	0.69	575	974	4.18	300	0.0265	671	10.00	52.20	1541	1185	0.0686	0.0334	0.27	0.59
21	Forearc	-41.85	1185	38.39	36.75	1.03	0.55	2539	4626	6.33	458	0.0263	114	12.36	14.52	5427	4311	0.0238	0.0253	0.11	0.58
22	Mountain Front	-15.20	1389	79.17	35.75	2.24	0.53	2140	3760	4.70	280	0.0366	98	12.97	91.33	5525	4890	0.0362	0.0502	0.44	0.57
23	Mountain Front	-16.22	1389	79.17	35.75	2.24	0.53	2140	3760	4.70	280	0.0366	98	12.97	91.33	5525	4890	0.0362	0.0502	0.44	0.57
24	Mountain Front	-16.39	1983	117.31	37.40	3.14	0.43	2581	4719	4.02	224	0.0274	122	13.79	83.12	5665	4915	0.0303	0.0663	0.41	0.55
25	Mountain Front	-16.53	990	100.86	24.58	4.10	0.35	2258	4754	4.71	240	0.0379	54	12.49	110.4	5716	4915	0.0278	0.0203	0.48	0.48
26	Mountain Front	-17.62	3532	124.16	37.38	3.32	0.54	2374	5547	4.47	281	0.0322	63	12.89	111.13	5970	5029	0.0256	0.0717	0.38	0.43
27	Mountain Front	-18.15	4076	125.15	47.95	2.63	0.48	2496	5719	5.33	303	0.0285	95	13.19	102.98	5862	5060	0.0231	0.0872	0.31	0.34
28	Mountain Front	-18.35	195	105.71	21.26	4.94	0.36	2566	4727	5.38	295	0.0443	48	15.27	15.27	5862	5069	0.0310	0.0305	0.29	0.38
29	Mountain Front	-18.29	1404	84.78	24.28	3.49	0.50	1915	4727	5.38	295	0.0443	48	15.27	15.27	5862	5069	0.0310	0.0305	0.29	0.38
30	Mountain Front	-18.47	3238	109.37	44.86	2.44	0.59	2254	5246	4.80	90	0.0322	76	12.40	106.27	5862	5105	0.0291	0.0793	0.41	0.43
31	Mountain Front	-18.78	2110	117.68	33.96	3.47	0.44	1947	5054	4.29	189	0.0327	61	10.67	131.44	5931	5131	0.0295	0.0420	0.43	0.39
32	Mountain Front	-19.19	4647	120.68	54.52	2.21	0.64	2439	5572	4.62	301	0.0279	77	11.41	119.53	5931	5169	0.0245	0.0999	0.39	0.44
33	Mountain Front	-21.43	3642	133.12	315.02	0.44	0.54	1977	5775	4.04	196	0.0097	197	12.63	90.37	5905	5384	0.0172	0.3855	0.46	0.34
34	Mountain Front	-22.43	2990	151.77	104.47	0.64	0.54	1977	5775	4.04	196	0.0097	197	12.63	90.37	5905	5384	0.0172	0.3855	0.46	0.34
35	Mountain Front	-25.41	6000	151.58	77.13	1.97	0.54	2526	5153	3.40	131	0.0252	95	11.38	127.06	6337	5752	0.0246	0.1437	0.43	0.49
36	Mountain Front	-26.14	4794	188.86	59.95	2.82	0.46	2157	5060	3.00	143	0.0216	120	12.31	108.11	6337	5815	0.0237	0.1240	0.35	0.43
37	Mountain Front	-27.85	5510	134.88	72.83	1.85	0.62	1428	4514	3.34	297	0.0189	50	12.11	87.41	5929	5812	0.0134	0.0522	0.24	0.32
38	Mountain Front	-29.31	3953	86.90	73.31	1.18	0.78	1549	4598	4.92	300	0.0298	75	11.34	94.95	5344	4734	0.0258	0.0904	0.29	0.36
39	Mountain Front	-32.38	1952	96.34	38.95	2.97	0.53	1319	3672	3.86	452	0.0285	288	12.19	103.31	4772	3933	0.0461	0.1484	0.23	0.35
40	Mountain Front	-34.26	1327	69.34	38.95	2.97	0.53	1319	3672	3.86	452	0.0285	288	12.19	103.31	4772	3933	0.0461	0.1484	0.23	0.35
41	Mountain Front	-40.26	9137	142.71	131.27	1.09	0.76	184	2403	1.88	89	0.0069	773	10.01	65.94	1834	1618	0.0025	0.0839	0.27	0.08
42	Mountain Front	-41.62	4457	117.75	50.83	2.32	0.64	115	2681	2.26	61	0.0011	595	10.07	54.57	1350	715	0.0028	0.0303	0.35	0.04

Table A 2: Raw data with geometry, relief, and climatic variables calculated for each basin: forearc and mountain-front catchments.

basin ID	group	latitude [°]	area [km <sup>2</sup> ]	basin_length [km]	basin_width [km]	basin_form	basin_elongation_ratio	basin_elevation	total_basin_relief [m]	basin_relief_ratio	basin_local_relief [m]	channel_slope [m m <sup>-1</sup> ]	mean_annual_rainfall [mm a <sup>-1</sup> ]	mean_annual_temperature [°C]	ground_frost [d a <sup>-1</sup> ]	modern_perennial_snowline [m]	lowest_Pleistocene_glaciers [m]	erosion_index	erosion_intensity [km <sup>3</sup> a <sup>-1</sup> ]	PCI	HI
43	Arc	-15.69	4367	138.55	55.10	2.51	0.54	2785	5158	3.72	387	0.0235	154	12.75	109.25	5411	4839	0.0282	0.1582	0.36	0.54
44	Arc	-16.61	17036	230.93	100.28	2.30	0.64	3616	6369	2.77	347	0.0143	238	7.35	209.34	5754	4828	0.0221	0.5610	0.44	0.57
45	Arc	-16.71	13590	186.59	115.59	1.63	0.70	3284	6278	3.33	217	0.0187	120	9.02	177.4	5805	4940	0.0205	0.3054	0.49	0.52
46	Arc	-17.15	12854	202.82	120.82	1.69	0.63	3519	5607	2.76	344	0.0158	196	8.43	186.59	5944	4979	0.0223	0.4026	0.42	0.63
47	Arc	-17.90	5719	144.88	49.69	2.92	0.59	2678	5797	4.00	268	0.0259	77	11.59	129.14	5982	5054	0.0227	0.1139	0.49	0.46
48	Arc	-18.42	3340	107.86	69.71	1.55	0.80	3463	5965	5.53	292	0.0304	133	9.02	177.66	5982	5105	0.0351	0.1351	0.44	0.58
49	Arc	-25.34	12015	197.64	99.27	1.99	0.63	2601	5866	2.88	215	0.0168	87	10.51	134.86	6362	5828	0.0156	0.1753	0.38	0.44
50	Arc	-25.34	15310	223.67	107.16	2.08	0.61	2830	5954	3.10	271	0.0157	115	9.46	129.33	6362	5790	0.0170	0.1607	0.30	0.46
51	Arc	-26.46	9226	197.25	107.25	1.84	0.62	2715	5954	3.10	271	0.0157	115	9.46	129.33	6362	5790	0.0170	0.1607	0.30	0.46
52	Arc	-29.91	9355	95.26	107.89	0.88	1.15	2542	6214	6.52	530	0.0268	154	7.75	152.18	5393	4383	0.0258	0.2992	0.34	0.41
53	Arc	-30.73	11645	148.19	134.40	1.10	0.82	1684	5539	3.74	417	0.0166	229	10.75	105.69	5186	4088	0.0252	0.4440	0.25	0.30
54	Arc	-31.59	6235	136.42	93.89	1.45	0.65	1945	5022	3.68	474	0.0231	295	9.16	140.57	4837	4022	0.0386	0.4243	0.27	0.39
55	Arc	-32.99	7510	144.39	93.82	1.54	0.68	1747	5815	4.03	462	0.0162	372	10.46	126.00	4801	3981	0.0312	0.4521	0.26	0.30
56	Arc	-33.97	31900	183.16	221.25	0.83	1.10	1304	6097	3.33	379	0.0163	557	10.60	112.03	3818	2941	0.0396	2.9024	0.21	0.21
57	Arc	-35.05	6231	166.55	70.19	2.37	0.53	1150	4066	2.44	339	0.0116	813	10.53	112.72	3169	2013	0.0330	0.5669	0.23	0.28
58	Arc	-35.34	20662	196.17	158.81	1.25	0.82	875	3937	1.98	289	0.0108	881	11.82	90.14	2877	2013	0.0322	2.0027	0.22	0.22
59	Arc	-36.39	11535	171.54	103.10	1.66	0.71	586	3185	1.86	195	0.0069	1136	12.33	78.50	2775	2101	0.0233	0.9077	0.23	0.19
60	Arc	-36.82	24024	286.48	153.24	1.88	0.61	803	3511	1.22	250	0.0039	1320	11.12	95.01	2788	2178	0.0141	1.2382	0.27	0.23
61	Arc	-38.79	12347	166.37	128.64	1.29	0.75	426	3075	1.65	143	0.0062	1307	11.04	78.29	2241	1834	0.0225	1.0043	0.20	0.14
62	Arc	-38.02	9285	157.69	103.10	1.53	0.69	646	3729	2.36	263	0.0032	1394	9.69	99.58	2203	1821	0.0116	0.3871	0.18	0.17
63	Arc	-39.87	11580	186.23	97.85	1.92	0.65	501	906	0.48	251	0.0032	1124	9.81	91.63	2024	1746	0.0108	0.4180	0.33	0.21
64	Arc	-16.42	15978	206.65	160.48	1.29	0.69	3778	6403	3.10	400	0.0147	358	7.15	185.69	5678	4915	0.0278	0.8409	0.36	0.59

Table A 3: Raw data with geometry, relief, and climatic variables calculated for each basin: arc catchments.

basin ID	group	latitude [°]	area [km <sup>2</sup> ]	basin_length [km]	basin_width [km]	basin_form	basin_elongation_ratio	basin_elevation	total_basin_relief [m]	basin_relief_ratio	basin_local_relief [m]	channel_slope [m m <sup>-1</sup> ]	mean_annual_rainfall [mm a <sup>-1</sup> ]	mean_annual_temperature [°C]	ground_frost [d a <sup>-1</sup> ]	modern_perennial_snowline [m]	lowest_Pleistocene_glaciers [m]	erosion_index	erosion_intensity [km <sup>3</sup> a <sup>-1</sup> ]	PCI	HI
65	Subbasin	-18.13	1205	36.15	49.91	0.84	1.08	4412	1485	4.11	183	0.0132	190	...	...	5474	4890	0.0183	0.0393	0.38	0.44
66	Subbasin	-16.64	1048	27.52	44.71	0.82	1.33	4672	1072	3.90	184	0.0086	277	...	...	5779	4928	0.0144	0.0251	0.36	0.34
67	Subbasin	-17.11	998	35.76	46.96	0.76	1.00	4654	2109	5.90	237	0.0148	206	...	...	5932	4978	0.0212	0.0304	0.67	0.48
68	Subbasin	-17.20	561	40.21	16.99	2.37	0.66	4055	2748	6.83	318	0.0410	114	...	...	5944	4991	0.0458	0.0262	0.46	0.47
69	Subbasin	-18.11	1434	42.42	62.14	0.68	1.01	4266	2549	6.01	269	0.0137	176	...	...	5932	5067	0.0182	0.0346	0.55	0.35
70	Subbasin	-18.60	552	38.13	22.80	1.67	0.70	3753	2246	5.89	269	0.0334	109	...	...	5931	5118	0.0411	0.0237	0.35	0.40
71	Subbasin	-19.23	479	41.05	13.02	3.15	0.60	4140	2374	5.78	255	0.0284	134	...	...	5931	5181	0.0340	0.0189	0.44	0.44
72	Subbasin	-19.80	645	46.04	21.51	2.14	0.62	4028	3484	7.57	340	0.0461	167	...	...	5931	5232	0.0654	0.0629	0.41	0.51
73	Subbasin	-20.19	427	42.80	19.70	2.17	0.54	3425	3550	8.29	271	0.0545	78	...	...	5931	5270	0.0481	0.0181	0.41	0.50
74	Subbasin	-20.78	1182	48.52	62.12	0.79	0.79	3764	3357	6.88	125	0.0332	90	...	...	5931	5334	0.0315	0.0354	0.53	0.70
75	Subbasin	-22.12	797	43.47	39.50	1.10	0.73	4036	2858	6.11	221	0.0369	136	...	...	5980	5460	0.0469	0.0439	0.30	0.41
76	Subbasin	-22.90	515	47.66	18.95	2.52	0.54	3852	3539	7.43	251	0.0490	91	...	...	5980	5536	0.0468	0.0230	0.36	0.41
77	Subbasin	-23.17	528	43.57	21.84	1.99	0.60	3658	3187	7.31	165	0.0478	87	...	...	5930	5562	0.0446	0.0220	0.31	0.41
78	Subbasin	-23.72	481	34.54	34.20	1.01	0.89	4547	2487	7.23	254	0.0326	115	...	...	6096	5913	0.0349	0.0169	0.42	0.47
79	Subbasin	-24.36	983	32.07	24.96	1.28	0.67	4289	2887	9.00	363	0.0472	115	...	...	6246	5976	0.0602	0.0273	0.41	0.40
80	Subbasin	-25.01	1239	54.02	49.46	1.09	0.74	4285	3074	5.69	223	0.0173	197	...	...	6337	5727	0.0217	0.0271	0.31	0.23
81	Subbasin	-25.05	1177	57.13	47.84	1.19	0.78	4285	3121	5.71	174	0.0173	197	...	...	6337	5727	0.0217	0.0271	0.31	0.23
82	Subbasin	-25.59	938	57.25	39.34	1.77	0.67	3789	3383	5.91	295	0.0418	60	...	...	6375	5941	0.0334	0.0236	0.36	0.49
83	Subbasin	-27.24	1193	58.34	26.39	2.21	0.67	3227	3142	5.39	370	0.0452	54	...	...	5980	5928	0.0332	0.0291	0.33	0.44
84	Subbasin	-27.75	1263	28.21	59.98	0.50	1.42	4131	2899	10.24	393	0.0289	98	...	...	5930	5963	0.0266	0.0359	0.35	0.40
85	Subbasin	-28.29	358	40.37	15.84	2.55	0.53	4288	3564	8.63	582	0.0602	127	...	...	5332	5332	0.0679	0.0274	0.44	0.58
86	Subbasin	-28.93	991	48.60	38.46	1.26	0.73	3727	4033	8.30	562	0.0508	126	...	...	5891	5332	0.0571	0.0635	0.40	0.54
87	Subbasin	-29.37	990	53.75	27.76	1.94	0.66	3931	2786	5.18	571	0.0301	182	...	...	5344	4863	0.0406	0.0543	0.38	0.55
88	Subbasin	-30.16	352	49.81	17.35	2.87	0.43	3485	3999	8.03	588	0.0500	316	...	...	5243	4187	0.0889	0.0556	0.44	0.55
89	Subbasin	-30.74	733	53.88	19.88	2.71	0.57	2737	4085	7.88	586	0.0496	269	...	...	5141	4068	0.0813	0.0978	0.36	0.49
90	Subbasin	-31.21	1125	53.27	33.87	1.57	0.71	3604	2414	4.53	512	0.0090	479	...	...	5039	4060	0.0186	0.0482	0.51	0.33
91	Subbasin	-31.91	1171	51.49	45.10	1.14	0.75	3064	4037	7.64	587	0.0437	379	...	...	4835	3886	0.0851	0.1940	0.40	0.45
92	Subbasin	-32.63	272	25.53	15.57	1.64	0.73	3543	2761	10.81	645	0.0640	475	...	...	4289	3844	0.1386	0.0627	0.27	0.45
93	Subbasin	-33.96	1137	57.40	33.74	1.70	0.66	3126	3843	6.70	753	0.0335	671	...	...	3780	2928	0.0668	0.2855	0.30	0.45
94	Subbasin	-34.97	766	51.12	23.21	2.20	0.61	1547	3999	6.65	548	0.0366	865	...	...	3298	2013	0.1136	0.2559	0.21	0.32
95	Subbasin	-35.82	763	52.05	28.95	1.74	0.60	2254	2958	5.68	461	0.0409	804	...	...	2775	2025	0.1191	0.2511	0.29	0.48
96	Subbasin	-36.04	1555	50.66	65.28	0.78	0.88	2001	2744	5.42	538	0.0145	1084	...	...	2775	2025	0.0481	0.2473	0.30	0.41
97	Subbasin	-36.95	1598	33.24	69.93	0.55	1.39	1988	2572	8.04	538	0.0156	1084	...	...	2775	2025	0.0481	0.2473	0.30	0.41
98	Subbasin	-37.05	1598	33.24	69.93	0.55	1.39	1988	2572	8.04	538	0.0156	1084	...	...	2775	2025	0.0481	0.2473	0.30	0.41
99	Subbasin	-38.43	2084	50.60	25.88	1.95	1.02	1127	2659	5.27	261	0.0134	1893	...	...	2295	1888	0.0586	0.5030	0.35	0.27
100	Subbasin	-14.95	417	33.94	18.36	1.86	0.68	3880	2082	6.13	274	0.0624	320	...	...	5246	4737	0.1125	0.0946	0.45	0.56
101	Subbasin	-14.91	891	46.05	23.41	1.97	0.64	4580	1454	3.16	292	0.0279	620	...	...	5246	4737	0.0640	0.1985	0.46	0.57
102	Subbasin	-14.85	531	29.89	25.29	1.18	0.87	4793	1418	4.74	359	0.0279	576	...	...	5246	4737	0.0640	0.1985	0.46	0.57
103	Subbasin	-17.47	1424	45.71	44.08	1.04	0.95	3788	4031	8.82	389	0.0432	131	...	...	5957	5016	0.0484	0.0863	0.32	0.52
104	Subbasin	-18.94	908	39.16	38.40	1.02	0.87	4036	2939	7.51	270	0.0367	118	...	...	5931	5156	0.0486	0.0490	0.33	0.48
105	Subbasin	-19.50	1077	41.42	36.04	1.15	0.89	3971	3069	7.41	322	0.0236	136	...	...	5980	5207	0.0427	0.0536	0.34	0.58
106	Subbasin	-21.68	675	35.22	32.32	1.09	0.83	3287	2290	6.50	266	0.0236	136	...	...	6299	5790	0.0166	0.0099	0.30	0.54
107	Subbasin	-25.90	886	37.86	28.63	1.32	0.78	3586	2763	7.30	221	0.0265	82	...	...	6299	5790	0.0240	0.0149	0.34	0.52
108	Subbasin	-26.47	322	17.05	38.37	0.43	1.19	4640	1978	11.60	297	0.0165	101	...	...	6362	5841	0.0166	0.0054	0.52	0.36
109	Subbasin	-32.86	909	30.80	48.45	0.64	1.10	3426	4457	14.47	770	0.0276	474	...	...	4301	3755	0.0691	0.1189	0.22	0.47
110	Subbasin	-33.51	1326	38.84	54.40	0.71	1.06	3707	5134	13.22	776	0.0218	545	...	...	4225	3322	0.0509	0.1575	0.20	0.44
111	Subbasin	-34.21	963	29.42	45.00	0.65	1.10	2920	4093	13.91	737	0.0184	848	...	...	3640	2674	0.0585	0.1584	0.22	0.45
112	Subbasin	-34.80	542	20.04	30.31	0.86	1.31	2943	3891	19.37	707	0.0264	858	...	...	3309	2013	0.0832	0.1321	0.22	0.45
113	Subbasin	-37.86	943	39.76	38.90	1.03	0.87	1423	2330	6.38	528	0.0089	1489	...	...	2495	2088	0.0343	0.1250	0.13	0.38
114	Subbasin	-37.95	1267	48.38	48.88	1.02	0.83	1495	2372	5.66	528	0.0089	1489	...	...	2495	2088	0.0343	0.1250	0.13	0.38
115	Subbasin	-38.25	1959	48.12	48.88	1.02	0.83	1495	2372	5.66	528	0.0089	1489	...	...	2495	2088	0.0343	0.1250	0.13	0.38
116	Subbasin	-39.25	2332	43.12	63.04	0.70	1.24	1087	1348	8.05	464	0.0086	847	...	...	2190	1821	0.0242	0.1188	0.23	0.34
117	Subbasin	-39.65	1482	67.48	33.60	2.01	0.64	1176	1723	2.55	464	0.0086	847	...	...	2126	1745	0.0279	0.1069	0.17	0.32
118	Subbasin	-40.65	889	37.41	28.93	1.39	0.90	1050	2025	5.41	671	0.0120	902	...	...	1605	1287	0.0366	0.0941	0.16	0.40
119	Subbasin	-41.15	1100	47.99	29.89	1.61	0.78	1050	3070	6.40	671	0.0120	902	...	...	1452	715	0.0794	0.2625	0.08	0.28
120	Subbasin	-41.99	1250	48.93	39.05	1.25	0.82	954	2390	4.88	686	0.0154	1218	...	...	1739	969	0.0537	0.2345	0.08	0.37

Table A 4: Raw data with geometry, relief, and climatic variables calculated for each basin: subcatchments.

Forearc	basin_area	basin_length	basin_width	basin_form	basin_elongation_ratio	basin_mean_elevation	total_basin_relie	basin_relie_ratio	basin_local_relie	channel_drop	mean_annual_rainfall	mean_annual_temperature	ground_frost	modern_perennial_snowline	lowest_Pleistocene_glaciers	erosion_index
Forearc	1.000															
basin_area	<b>0.988</b>	1.000														
basin_length	0.000	1.000														
basin_width	0.446	0.446	1.000													
basin_form	0.043	0.043	-0.650	1.000												
basin_elongation_ratio	0.029	0.043	0.010	<b>-0.869</b>	1.000											
basin_mean_elevation	0.081	<b>0.804</b>	0.000	0.000	<b>-0.199</b>	1.000										
total_basin_relie	0.090	0.090	0.000	0.000	0.000	<b>0.817</b>	1.000									
basin_relie_ratio	0.090	0.090	0.000	0.000	0.000	0.000	0.417	1.000								
basin_local_relie	0.090	0.090	0.000	0.000	0.000	0.000	0.000	0.000	1.000							
channel_drop	0.090	0.090	0.000	0.000	0.000	0.000	0.000	0.000	0.000	1.000						
mean_annual_rainfall	<b>-0.609</b>	<b>-0.635</b>	-0.242	-0.405	0.198	<b>-0.738</b>	<b>-0.776</b>	-0.363	0.219	-0.438	1.000					
mean_annual_temperature	0.533	<b>0.654</b>	0.342	0.232	-0.231	0.000	<b>0.659</b>	0.148	-0.455	0.227	-0.721	1.000				
ground_frost	-0.281	-0.242	-0.136	-0.175	0.094	0.121	0.005	0.301	0.168	0.214	0.399	-0.375	1.000			
modern_perennial_snowline	0.217	0.292	0.557	0.449	0.716	0.600	0.862	0.185	0.465	0.351	0.073	0.694	0.000	1.000		
lowest_Pleistocene_glacier	0.017	0.000	0.000	0.000	0.000	0.000	0.000	0.000	0.000	0.000	0.000	0.000	0.000	0.000	1.000	
erosion_index	<b>-0.521</b>	<b>-0.523</b>	-0.343	-0.183	0.100	0.246	-0.091	<b>0.635</b>	0.170	<b>0.727</b>	0.250	-0.329	0.421	-0.193	0.421	1.000
erosion_intensity	0.252	0.096	0.476	-0.423	0.320	0.089	0.141	0.085	-0.056	0.151	0.308	-0.020	0.358	-0.039	0.462	0.372
<i>bold r &gt; 0.5, shaded r' &gt; 0.5</i>																
Mountain Front	1.000															
basin_area	<b>0.516</b>	1.000														
basin_length	0.017	<b>0.622</b>	1.000													
basin_width	<b>0.984</b>	0.000	1.000													
basin_form	<b>-0.630</b>	-0.319	<b>-0.754</b>	1.000												
basin_elongation_ratio	<b>0.968</b>	0.388	<b>0.969</b>	<b>-0.812</b>	1.000											
basin_mean_elevation	-0.074	-0.075	-0.135	0.342	-0.179	1.000										
total_basin_relie	0.185	0.187	0.092	0.262	0.074	<b>0.824</b>	1.000									
basin_relie_ratio	0.187	0.187	0.092	0.262	0.074	<b>0.824</b>	1.000									
basin_local_relie	-0.300	<b>-0.706</b>	-0.364	0.431	-0.270	<b>0.572</b>	<b>0.536</b>	1.000								
channel_drop	0.053	0.000	0.104	0.051	0.236	0.001	0.012	0.000	0.000	0.000						
mean_annual_rainfall	-0.428	<b>-0.675</b>	-0.445	0.315	-0.371	0.243	0.091	<b>0.630</b>	1.000							
mean_annual_temperature	0.053	0.001	0.043	0.165	0.098	0.289	0.726	0.002	0.002	0.000						
ground_frost	<b>-0.551</b>	<b>-0.635</b>	<b>-0.695</b>	<b>0.640</b>	<b>-0.570</b>	<b>0.639</b>	0.478	<b>0.896</b>	<b>0.605</b>	1.000						
modern_perennial_snowline	0.117	0.188	0.189	-0.328	0.164	<b>-0.847</b>	<b>-0.811</b>	-0.710	-0.285	<b>-0.743</b>	1.000					
lowest_Pleistocene_glacier	0.016	0.000	0.000	0.000	0.000	0.000	0.000	0.000	0.000	0.000	0.000	1.000				
erosion_index	0.016	-0.222	-0.159	0.300	-0.052	0.340	0.371	0.048	0.159	0.402	-0.456	0.000	1.000			
erosion_intensity	0.016	-0.222	-0.159	0.300	-0.052	0.340	0.371	0.048	0.159	0.402	-0.456	0.000	1.000			
erosion_index	0.016	-0.222	-0.159	0.300	-0.052	0.340	0.371	0.048	0.159	0.402	-0.456	0.000	1.000			
erosion_intensity	0.016	-0.222	-0.159	0.300	-0.052	0.340	0.371	0.048	0.159	0.402	-0.456	0.000	1.000			
erosion_index	0.016	-0.222	-0.159	0.300	-0.052	0.340	0.371	0.048	0.159	0.402	-0.456	0.000	1.000			
erosion_intensity	0.016	-0.222	-0.159	0.300	-0.052	0.340	0.371	0.048	0.159	0.402	-0.456	0.000	1.000			
<i>bold r &gt; 0.5, shaded r' &gt; 0.5</i>																

Table A 5: Correlations between variables: forearc catchments and mountain-front catchments.

Arc	basin_area	basin_length	basin_width	basin_form	basin_elongation_ratio	basin_mean_elevation	total_basin_relie	basin_relie_ratio	basin_local_relie	channel_drop	mean_annual_rainfall	mean_annual_temperature	ground_frost_perennial_snowline	modern_perennial_snowline	lowest_Pleistocene_glaciers	erosion_index
1.000	1.000															
basin_area	0.624	1.000														
basin_length	0.001	0.432	1.000													
basin_width	0.884	0.045	-0.740	1.000												
basin_form	-0.437	0.128	0.577	-0.762	1.000											
basin_elongation_ratio	0.502	-0.237	0.691	0.177	0.153	1.000										
total_basin_elevation	-0.190	-0.101	0.351	0.457	0.168	0.816	1.000									
total_basin_relie	0.009	-0.166	0.111	-0.129	0.181	0.000	0.734	1.000								
basin_relie_ratio	-0.373	-0.709	-0.201	-0.195	0.342	0.689	0.000	0.526	1.000							
basin_local_relie	0.087	0.000	0.369	0.384	0.120	0.006	0.000	0.687	0.000	1.000						
channel_drop	-0.136	-0.335	0.061	-0.266	0.265	0.385	0.000	0.000	0.000	0.000	1.000					
mean_annual_rainfall	-0.472	-0.690	-0.328	0.125	-0.018	0.706	0.726	0.929	0.448	1.000						
mean_annual_temperature	0.252	0.071	0.137	-0.074	0.238	-0.850	-0.850	-0.746	-0.642	0.000	1.000					
ground_frost	-0.002	-0.052	-0.127	0.265	-0.114	0.589	-0.458	-0.309	-0.440	-0.171	0.386	1.000				
modern_perennial_snowline	-0.097	0.023	-0.062	0.038	-0.095	0.921	0.000	0.481	0.357	0.546	-0.715	-0.804	1.000			
lowest_Pleistocene_glacier_extent	0.333	-0.163	-0.094	0.093	-0.066	0.929	0.889	0.648	0.421	0.795	-0.961	-0.442	0.786	1.000		
erosion_index	0.080	0.468	0.676	0.681	0.704	0.000	0.000	0.001	0.051	0.000	0.039	0.000	0.000	0.685	1.000	
erosion_intensity	-0.090	-0.433	-0.100	-0.121	0.187	0.068	0.301	0.442	0.373	0.536	-0.224	0.079	0.105	0.103	-0.012	1.000
total_basin_elevation	0.804	0.336	0.611	-0.383	0.511	-0.440	-0.156	-0.307	-0.139	-0.323	0.429	0.262	-0.351	-0.471	-0.513	0.372
total_basin_relie	0.000	0.126	0.002	0.079	0.015	0.040	0.489	0.185	0.538	0.142	0.046	0.239	0.110	0.027	0.015	0.088
<i>bold: r &gt; 0.5, shaded: r &gt; 0.5</i>																
Subbasins	basin_area	basin_length	basin_width	basin_form	basin_elongation_ratio	basin_mean_elevation	total_basin_relie	basin_relie_ratio	basin_local_relie	channel_drop	mean_annual_rainfall	mean_annual_temperature	ground_frost_perennial_snowline	modern_perennial_snowline	lowest_Pleistocene_glaciers	erosion_index
1.000	1.000															
basin_area	0.397	1.000														
basin_length	0.006	-0.006	1.000													
basin_width	0.714	0.448	-0.818	1.000												
basin_form	-0.408	0.448	0.001	0.000	1.000											
basin_elongation_ratio	0.453	-0.592	0.642	-0.795	1.000											
basin_mean_elevation	-0.496	-0.393	-0.149	-0.011	-0.042	1.000										
total_basin_relie	0.016	0.112	0.040	0.099	-0.079	-0.044	1.000									
basin_relie_ratio	0.968	0.755	0.465	0.595	0.665	0.750	0.651	1.000								
basin_local_relie	0.080	0.000	0.688	0.038	0.002	0.281	0.000	0.651	1.000							
channel_drop	0.060	0.008	0.019	-0.014	0.103	-0.389	0.537	0.485	1.000							
mean_annual_rainfall	0.659	0.566	0.889	0.920	0.451	0.003	0.000	0.000	0.000	1.000						
mean_annual_temperature	-0.519	0.006	-0.583	0.532	-0.651	0.372	0.413	0.225	0.005	1.000						
ground_frost	0.000	0.986	0.000	0.000	0.000	0.005	0.002	0.973	0.000	-0.561	1.000					
modern_perennial_snowline	0.000	0.144	0.253	-0.181	0.273	-0.829	-0.111	-0.090	0.411	0.438	0.000	0.014	0.000	0.888	1.000	
lowest_Pleistocene_glacier_extent	0.001	-0.438	-0.202	-0.184	0.106	-0.189	0.000	0.751	0.631	0.457	-0.900	-0.277	0.438	0.000	0.000	
erosion_index	-0.284	0.028	-0.390	0.334	-0.290	0.162	0.303	0.238	0.480	0.876	0.196	-0.127	0.081	-0.289	-0.328	1.000
erosion_intensity	0.674	0.064	0.674	0.248	0.092	0.714	0.653	0.688	0.368	0.914	0.520	0.630	-0.630	-0.778	-0.784	0.633
erosion_intensity	0.000	0.041	0.068	0.482	0.122	0.020	0.665	0.618	0.002	0.030	0.000	0.018	0.001	0.000	0.000	0.001
<i>bold: r &gt; 0.5, shaded: r &gt; 0.5</i>																

Table A 6: Correlations between variables: arc catchments and subcatchments..

	Forearc		Mountain Front		Arc		Subbasins	
	HI	PCI	HI	PCI	HI	PCI	HI	PCI
basin_area	-0.301 0.185	0.042 0.857	-0.186 0.419	0.225 0.326	-0.267 0.230	-0.281 0.205	-0.469 0.000	-0.268 0.046
basin_length	-0.189 0.411	0.157 0.498	-0.272 0.233	0.088 0.706	-0.060 0.790	-0.014 0.952	-0.167 0.218	-0.141 0.299
basin_width	-0.300 0.187	0.005 0.983	-0.216 0.348	0.171 0.459	-0.200 0.372	-0.379 0.082	-0.255 0.058	-0.087 0.524
basin_form	0.155 0.502	0.168 0.467	0.282 0.215	0.031 0.895	0.228 0.307	0.454 0.034	0.151 0.267	0.100 0.463
basin_elongation_ratio	-0.113 0.624	-0.121 0.601	-0.258 0.260	0.126 0.585	-0.273 0.219	-0.318 0.149	-0.236 0.079	-0.124 0.362
basin_mean_elevation	<b>0.731</b> 0.000	<b>0.828</b> 0.000	<b>0.928</b> 0.000	<b>0.573</b> 0.007	<b>0.980</b> 0.000	<b>0.817</b> 0.000	0.496 0.000	<b>0.740</b> 0.000
total_basin_relief	0.245 0.285	0.475 0.030	<b>0.590</b> 0.005	0.399 0.073	<b>0.717</b> 0.000	0.492 0.020	0.175 0.197	-0.199 0.142
basin_relief_ratio	<b>0.719</b> 0.000	<b>0.583</b> 0.006	<b>0.683</b> 0.001	0.214 0.352	<b>0.503</b> 0.017	0.364 0.096	0.165 0.224	-0.142 0.297
basin_local_relief	-0.052 0.823	-0.383 0.086	0.379 0.090	-0.355 0.115	0.323 0.143	0.003 0.989	-0.029 0.835	<b>-0.508</b> 0.000
channel_drop	<b>0.762</b> 0.000	<b>0.587</b> 0.005	<b>0.756</b> 0.000	0.165 0.474	<b>0.694</b> 0.000	<b>0.603</b> 0.003	<b>0.522</b> 0.000	0.231 0.086
mean_annual_rainfall	-0.393 0.078	<b>-0.595</b> 0.004	<b>-0.798</b> 0.000	-0.366 0.103	<b>-0.822</b> 0.000	<b>-0.677</b> 0.001	<b>-0.473</b> 0.000	<b>-0.572</b> 0.000
mean_annual_temperature	0.302 0.184	<b>0.671</b> 0.001	0.426 0.054	-0.103 0.657	<b>-0.534</b> 0.010	-0.382 0.079	-0.284 0.034	-0.411 0.002
ground_frost	0.118 0.612	0.015 0.949	0.462 0.035	0.363 0.105	<b>0.883</b> 0.000	<b>0.740</b> 0.000	0.266 0.048	0.517 0.000
modern_perennial_snowline	0.445 0.043	<b>0.758</b> 0.000	<b>0.804</b> 0.000	0.323 0.153	<b>0.896</b> 0.000	<b>0.748</b> 0.000	0.465 0.000	<b>0.723</b> 0.000
lowest_Pleistocene_glacier_extent	0.481 0.027	<b>0.765</b> 0.000	<b>0.785</b> 0.000	0.324 0.151	<b>0.881</b> 0.000	<b>0.736</b> 0.000	0.446 0.001	<b>0.697</b> 0.000
erosion_index	-0.122 0.598	<b>-0.624</b> 0.003	0.216 0.348	-0.421 0.057	-0.181 0.421	-0.251 0.261	-0.090 0.509	-0.453 0.000
erosion_intensity	<b>-0.562</b> 0.008	<b>-0.680</b> 0.001	<b>-0.571</b> 0.007	<b>-0.759</b> 0.000	<b>-0.567</b> 0.006	<b>-0.537</b> 0.010	-0.494 0.000	<b>-0.565</b> 0.000

*bold:  $R > 0.5$ , shaded:  $R^2 > 0.5$*

Table A 7: Correlations between HI, PCI, and calculated variables.